

Design of a Single Capillary-Parenchymal Co-culture Bioreactor

by

Ernest S. Kim

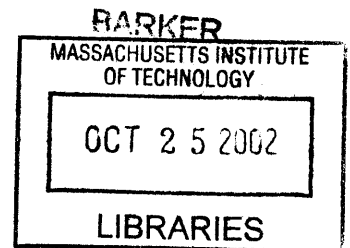
Sc.B. Mechanical Engineering
Brown University 1997

SUBMITTED TO THE DEPARTMENT OF MECHANICAL ENGINEERING IN PARTIAL
FULFILLMENT OF THE REQUIREMENTS FOR THE DEGREE OF

MASTER OF SCIENCE IN MECHANICAL ENGINEERING
AT THE
MASSACHUSETTS INSTITUTE OF TECHNOLOGY

JUNE 2002

©2002 Ernest Soonho Kim. All rights reserved.



The author hereby grants to MIT permission to reproduce and to distribute publicly paper and
electronic copies of this thesis document in whole or in part.

Signature of Author: _____

Department of Mechanical Engineering
May 24, 2002

Certified by: _____

Jeffrey T. Borenstein
The Charles Stark Draper Laboratory
Thesis Supervisor

Certified by: _____

Roger D. Kamm
Professor of Mechanical Engineering
Thesis Supervisor

Accepted by: _____

Professor Ain A. Sonin
Professor of Mechanical Engineering
Graduate Officer, Department of Mechanical Engineering

This page intentionally left blank.

Design of a Single Capillary-Parenchymal Co-culture Bioreactor

Ernest S. Kim

Submitted to the Department of Mechanical Engineering on May 24, 2002, in partial fulfillment of the requirements for the Degree of Master of Science in Mechanical Engineering.

Abstract

For the over 80,000 patients currently on the waiting list for complex internal organ transplant, tissue engineering is the only promising long-term solution to the problem of insufficient donor organs. Although some non-vascular tissues have been successfully engineered and implanted, thick, complex organs, such as the liver, require integration of vascular networks to deliver oxygen and nutrients to cells deep within the engineered constructs. Current efforts to engineer liver tissue include utilization of large-scale (~10 centimeters) micro-machined fluidic networks of blood vessels and capillaries cultured adjacent to confluent sheets of hepatocytes, and smaller constructs (~300 by 200 micrometers) of endothelial cells and hepatocytes which self-organize in co-culture. These approaches utilize microlithography technology to form structures on the length scales of blood vessels and capillaries. Another requirement for tissue-engineered organs is new materials. One such material is a class of self-assembling oligopeptides, which, in solution, form a gel when exposed to sufficient saline concentrations. Cell cultures in these peptide gels have shown excellent viability, and the gels have been shown to be very biocompatible, eliciting no immune response when implanted.

The objective of this thesis is to design and fabricate a novel bioreactor for co-culture of endothelial and hepatic parenchymal cells in a unique geometry. The bioreactor mimics the *in vivo* characteristics of the smallest functional unit of the liver, a single capillary and the adjacent hepatocytes, i.e. a 'capillary-parenchymal element' (CPE). The motivation for this work is the need to understand the cell-cell interactions that occur at this most basic unit of the liver; this knowledge can then be applied to the development of tissue-engineered replacement organs. The overall dimensions of the bioreactor are on the scale of a single capillary and the adjacent hepatocytes. The device utilizes microlithography fabrication technology to specify the location and geometry of the various cell-types. Additionally, this study is among the first applications of the self-assembling peptide gel.

The device enables the study of co-cultured cells to further the development of *in vitro* co-cultured tissue and tissue-engineered replacement organs. Analytic and numerical modeling techniques were used to investigate fluid flow and to model mass transfer in the little-understood gelation process of these self-assembling peptides, thus aiding in the design of the bioreactor. The experimental setup incorporated instrumentation to observe and control flow in the microscopic device. To fabricate the membrane, protocols and procedures were developed to initiate gelation of the peptide in previously untried conditions and geometries.

Thesis Supervisor: Jeffrey T. Borenstein

Title: Group Leader, MEMS Sensors Group, The Charles Stark Draper Laboratory, Inc.

Thesis Supervisor: Roger D. Kamm

Title: Professor of Mechanical Engineering

This page intentionally left blank.

Acknowledgments

I would like to thank my thesis advisors, Roger Kamm and Jeffrey Borenstein, for their guidance and encouragement throughout this work. I am fortunate and lucky to have worked with them. I would also like to acknowledge and thank Dr. Joseph P. Vacanti and his lab at Massachusetts General Hospital for supporting and helping to inspire this work, and for initiating the collaboration between my advisors. Dr. Mohammad Reza Kaazempur-Mofrad has been an enormous help with the modeling and the writing process. His efforts and willingness to help students are phenomenal. I am grateful to CIMIT (The Center for Integration of Medicine and Innovative Technology) for supporting this work and the work of my aforementioned mentors and advisors. Claire Sasahara has been exceptionally helpful, from my days as a teaching assistant, and throughout my research. Also, Shuguang Zhang and Alan Grodzinsky kindly allowed me to use their facilities for peptide synthesis and have both been truly inspirational teachers. I am grateful for the support, input, and friendship of my fellow graduate students and post-docs in the Kamm group. Michael Caplan was always willing to lend his time and patience to teach me about the peptide and peptide synthesis. Discussions with the peptide group, Davide Marini, Wonmuk Huang, and Gina Kim, on science and life in general, have been enlightening and fun. Thanks also to Ana Isasi, Belinda Yap, Janice Tan, Sephalie Patel, and Helene Karcher for making the Fluids Lab a fun place to work and write.

At Draper Laboratory, Chris Dubé and Angela Zapata devoted significant amounts of time and energy to helping me put together the written thesis, for which I am very grateful. I would like to thank everyone in the MEMS Sensors group for being helpful, warm and patient, and for fabricating my devices. Ed MacCormack, John Mahoney, and the rest of the folks in the Draper Central Machine shop were always very helpful and friendly, and would stop whatever they were doing when I came by with questions on mechanical design. Thanks also to Eli Weinberg, Kevin King, and ChiaoChun Joanne Wang, fellow students at Draper, for providing camaraderie and minds to bounce ideas off of.

My musical cohorts, local and worldwide, have been instrumental (!) in maintaining balance in my life: Brian Church and Stephen Budney (Tristan da Cunha), Kirthi Reddy (mopu mopu), and John McGreevy and Jason Zevin (RPBC). My housemates, Angus Davol, Brian, and Mark Schnittman, my friends, near and far, old and new, and my family, far and farther, old and new, have really made the past few years of my life the best so far, and I give them my deepest love and thanks.

This thesis was prepared at The Charles Stark Draper Laboratory, Inc., under Cooperative Agreement DAMD17-07-2-00, sponsored by the Department of the Army.

Publication of this thesis does not constitute approval by Draper or the sponsoring agency of the findings or conclusions contained herein. It is published for the exchange and stimulation of ideas.


Ernest S. Kim

May 24, 2002

This page intentionally left blank.

Contents

Abstract	3
Acknowledgments	5
Contents	7
List of Figures	11
List of Tables	16
1 Introduction	17
1.1 Background	17
1.1.1 Tissue Engineering	17
1.1.2 The Liver	18
1.1.3 Growing Cells and Co-Culture	19
1.1.4 Previous Work	21
1.2 Enabling Technologies	22
1.2.1 Self-Assembling Oligopeptide	22
1.2.2 MicroElectroMechanical Systems (MEMS)	23
1.3 Objectives and Scope of This Study	23
2 Device Design	27
2.1 Device Concept	28
2.2 Material Selection	32
2.3 Membrane Design: Stress Analysis	33
2.3.1 Flow-Induced Stress	33
2.3.2 Stresses Due to Pressure Differences Across the Membrane	35
2.3.2.1 Bending	36
2.3.2.2 Surface Tension	37
2.3.3 Micron-Scale Design: Stress Analysis Results	38
2.3.3.1 Flow-Induced Stress Results	39
2.3.3.2 Pressure Difference-Induced Stress Results	40
2.3.4 Transport Considerations	40
2.4 Macro-Scale Device Design	42
2.4.1 Flow delivery	42
2.4.2 Visibility, Cost Reduction, and Pressure Regulation	42
2.5 Fabricated Device Specifications	43
2.6 Summary	47
3 Fabrication and Experimental Setup	49
3.1 Silicon-Glass Device Fabrication	49

3.1.1	Mask Fabrication	49
3.1.2	Silicon Wafer Processing	50
3.1.3	Glass Wafer Processing	51
3.1.4	Glass-Silicon Bonding and Dicing	52
3.2	Fluidic Fittings	52
3.2.1	Design of the Fittings	52
3.2.2	Assembly Procedure	53
3.3	Device Validation	54
3.4	Experimental Setup	55
3.5	Summary	58
4	Computational Analysis	59
4.1	Flow Parameters and Constraints	59
4.2	Analytic Solution to the Three-Dimensional Flow	61
4.2.1	Derivation of the Analytic Solution	61
4.2.2	Application and Execution of the Analytic Model	65
4.2.3	Results from the Analytic Model	67
4.3	Numerical Model: Fluid Flow and Mass Transfer	70
4.3.1	Setting up the Numerical model	70
4.3.2	Numerical Results	72
4.4	Summary	75
5	Experimental Studies	77
5.1	Macro-Scale Experiment	77
5.1.1	Macro-Scale Experiment: Introduction	77
5.1.2	Macro-Scale Experiment: Materials and Methods	78
5.1.3	Macro-Scale Experiment: Results	81
5.1.4	Macro-Scale Experiment: Discussion (The Congo Red Stain Gradient)	89
5.1.5	Macro-Scale Experiment: Conclusions	90
5.2	Micron-Scale Viscosity Experiment	92
5.2.1	Micron-Scale Viscosity Experiment: Introduction	92
5.2.2	Micron-Scale Viscosity Experiment: Methods	93
5.2.3	Micron-Scale Viscosity Experiment: Results and Discussion	96
5.2.4	Micron-Scale Viscosity Experiment: Conclusions	97
5.3	Micron-Scale Membrane-Forming Experiment: Micro Experiment Design I- μ	97
5.3.1	Micro Experiment Design I- μ : Introduction	97
5.3.2	Micro Experiment Design I- μ : Methods and Results	97
5.3.2.1	Prepare Experiment, Confirm Equal Resistance	99
5.3.2.2	Infuse Peptide	101
5.3.2.3	Infuse Saline, Begin Gelation	102
5.3.2.4	Slow Flow, Continue Gelation	103
5.4	Micro Experiment Design II- μ	109

5.4.1	Prepare Experiment, Confirm Equal Resistance	110
5.4.2	Infuse Peptide	110
5.4.3	Infuse Saline, Begin Gelation	111
5.4.4	Stop Flow, Continue Gelation	111
5.5	Summary	111
6	Recommendations for Further Development of the Capillary-Parenchymal Element (CPE) Bioreactor	113
6.1	Improvements for Successful Membrane Formation: Processes and Materials	113
6.1.1	Mask Selection	113
6.1.2	Material Selection	114
6.2	Improvements for Successful Membrane Formation: Geometry Design	115
6.2.1	Resistance Reduction	115
6.2.2	Center Channel Dimension	117
6.2.2.1	Numerical Results for a 24-12-24 Device	117
6.2.2.2	Numerical Results for a 24-6-24 Device	119
6.3	Investigating the Nature of Gel Formation	121
6.4	Testing the Gel	121
6.5	Cell Culture	123
6.5.1	Surface Chemistry Modification	123
6.5.2	Geometry Modification	123
6.6	Summary	125
7	Summary and Conclusions	127
7.1	Summary of the Work	127
7.2	Results	127
7.3	Recommendations for Further Work	128
	References	131
	Appendix	135
A2.1	Shear Stress on the Membrane	135
A2.2	Stresses Due to Pressure Differences Across the Membrane: Bending	138
A2.3	Stresses Due to Pressure Differences Across the Membrane: Surface Tension	140
A3.1	Mask Layouts	142
A3.2	Fluidic Fittings: Fabrication and Assembly	144
A3.2.1	Large-Bore Fittings	144
A3.2.2	Small-Bore Fittings	145
A3.3	Adhesive Gasket	146

A3.4	Modifications to the Harvard Apparatus PHD 2000 Push/Pull Syringe Pump	148
A4.1	Peptide Solution Density Measurements	155
A4.2	Peptide Solution Viscosity Measurements	156
A4.3	Derivation of the Analytic Solution	157
A4.4	Analytic Model Implemented in MATLAB	165
	A4.4.1 MATLAB Code	166
A4.5	Diffusivity Calculation for Peptide	169
A4.6	Non-Dimensionalizing the Numerical Model	171
A5.1	Preparation of the Peptide Solution	175
A5.2	Micron-Scale Viscosity Experiment: Measurement Procedure and Validation	175
A5.3	Calculation of μ_{center}	177
A5.4	Design of the Simultaneous Pressure Release Fixtures	179

List of Figures

1.1	Diagram of the liver	18
1.2	Cross-section view of a sinusoid and the adjacent hepatocytes	19
1.3	A diagram of the cellular and vascular organization of the liver, and a section diagram of the proposed bioreactor	23
2.1	Top view of the device; the channels are completely filled with water.	28
2.2	Self-assembling peptide solution is flowed through the center channel of the device, while water is flowed through the side channels.	28
2.3	Saline solution is added to the side channel flow.	29
2.4	The peptide solution begins to form a gel at the fluid interfaces.	29
2.5	The peptide solution forms a full gel between the two saline-filled channels.	30
2.6	Diagram showing cells in culture in the device. The section view shows the endothelial cells in the morphological configuration of a capillary.	30
2.7	Schematic of the device, showing key dimensions	31
2.8	Isometric view of the channels with laminar flow	34
2.9	Forces on the membrane	34
2.10	Flow in a rectangular channel; the gray wall represents the membrane.	35
2.11	A pressure gradient across the membrane ($P_a > P_b$) causes deformation.	36
2.12	A section view of the deformed membrane, attached to the top (glass) and bottom (silicon) surfaces of a channel; a diagram showing the stress distribution in the membrane and the bending moment	36
2.13	A pressure difference across the membrane causes the membrane to bow.	37
2.14	The stretched geometry of the membrane	37
2.15	A plot of the minimum membrane thickness (t_{min}) for the average velocity of flow in the channels ($V_{average}$) for a fluid with the viscosity and density of water	39
2.16	The pressure required to fracture the membrane for a range of membrane thicknesses	40
3.1	Diagram showing the silicon photolithography process	50
3.2	Diagram showing the metal-on-glass deposition process	51
3.3	A top view of the device, looking through the glass. The detail image shows a magnified view of the converged-channel area. An isometric drawing of a large-bore and small-bore fluidic fitting.	53
3.4	A smaller volume of solution becomes diluted in the small-bore tubing than in the large-bore tubing.	53
3.5	A cut-away view of an assembled large-bore fluidic fitting, showing placement of the adhesive ring and the application of the epoxy	54
3.6	Testing to verify that the channels are unoccluded	55
3.7	The modified Harvard PHD2000 syringe pump	56
3.8	The experimental setup	58
4.1	Flow rates are chosen that provide laminar flow conditions.	60
4.2	The membrane is to be of uniform thickness along the entire converged-channel area.	60
4.3	Modeled geometry, $\frac{1}{4}$ analytic solution of the velocity field, $\frac{1}{4}$ model of the numerical flow solution, $\frac{1}{4}$ model of the mass transfer solution for concentration	61

4.4	A top view of the converged-channel area; the red box shows the fully-developed region for low Reynolds number flow	62
4.5	An isometric view of the boxed-region in Figure 4.4	63
4.6	A cross-section view of the converged-channel region corresponding to the area denoted by the dotted line in Figure 4.5	64
4.7	A single quadrant of the cross-section shown in Figure 4.6	64
4.8	A plot of the flow ratio $Q_S:Q_P$ as a function of y_m	66
4.9	A plot of the flow ratio $Q_S:Q_P$ as a function of $\mu_{\text{peptide}}:\mu_{\text{saline}}$	66
4.10	A plot of the absolute flow rates (Q_S and Q_P) as linear functions of the axial pressure gradient over the converged-channel region (dp/dx)	67
4.11	The flow profile for $\mu_{\text{saline}} = 0.001 \text{ Pa}\cdot\text{s}$, $\mu_{\text{peptide}} = 0.0060 \text{ Pa}\cdot\text{s}$, $y_m = 24 \text{ }\mu\text{m}$	68
4.12	The flow profile for $\mu_{\text{saline}} = 0.00711 \text{ Pa}\cdot\text{s}$, $\mu_{\text{peptide}} = 0.0060 \text{ Pa}\cdot\text{s}$, $y_m = 24 \text{ }\mu\text{m}$	69
4.13	(a) The converged-channel device area geometry for Fc1; (b) $\frac{1}{4}$ model of the geometry, cut along two planes of symmetry	71
4.14	A vector plot of the numerical results for the normalized velocity field; flow is left to right	72
4.15	An isometric vector plot of the numerical results for the normalized velocity field; flow is upper right to lower left	73
4.16	A band plot of the numerical results for the normalized mass transfer solution for peptide concentration	74
4.17	A band plot of the numerical results for the normalized mass transfer solution for saline concentration	74
4.18	The overlapping region where concentrations of peptide and saline are sufficient for gelling	75
4.19	Normalized pressure in the device	75
5.1	Schematic of the macro-scale experimental setup; tubing and syringes are not to scale. Syringes were mounted on and removed from the pump as they were needed (See Section 5.1.2 for the protocol).	78
5.2	Device Fc8, shown with fluorescein dye flowing in through the center channel and out the outlet channels on the right	79
5.3	Device Fc8 fluidic ports, labeled as followed: C_L = large-bore center inlet, C_S = small-bore center inlet, C_O = large-bore center outlet; S_L = large-bore side inlets, S_S = small-bore side inlets, S_O = large-bore side outlets	79
5.4	Water was “pushed” into the device through the large bore inlets and “pulled” out through the large-bore outlets.	80
5.5	Peptide solution was infused through the center channel at $10 \text{ }\mu\text{l}/\text{min}$, while water was infused through the side channels at $20 \text{ }\mu\text{l}/\text{min}$.	80
5.6	A solution of saline, fluorescein, and Congo Red was infused through the side inlets at $20 \text{ }\mu\text{l}/\text{min}$; peptide flow was maintained at $10 \text{ }\mu\text{l}/\text{min}$.	81
5.7	$t \sim 0$. The observed black marks and nicks were imperfections on the glass surface. This and the following images have been reversed to show flow from left to right.	82
5.8	$t = 1:30$. The dye appeared to be at approximately equal concentrations on both sides of the center peptide stream.	82
5.9	$t = 24:00$. Fluorescein has diffused throughout the converged-channel area.	83

5.10	t = 36:00. High-magnification image showing Congo Red staining along the upper leading edge of the saline-peptide interface, indicating the presence of peptide gel	83
5.11	t = 40:00. The converged-channel area stitched from two images.	84
5.12	t = 83:00. Fluorescein was flushed from the device. Congo Red staining was very visible.	85
5.13	t = 86:00. The gel appeared torn at the divergence of the channels.	85
5.14	t = 164:00. Fluorescein has been removed from the device. Congo Red stain is visible along the edges of the peptide region.	86
5.15	A “panoramic” view of device, showing the inlet channels and the outlet channels. Note the gelled and stained peptide particles in the upper right outlet channel.	86
5.16	t = 19:49:00. High-magnification image of the fractured peptide gel membrane.	87
5.16a	Detail view <i>a</i> of Figure 5.16.	87
5.16b	Detail view <i>b</i> of Figure 5.16.	87
5.16c	Detail view <i>c</i> of Figure 5.16.	88
5.17	High-magnification image showing the Congo Red staining gradient.	88
5.17b	Detail view of Figure 5.17. Note the staining gradient and the dark edge of the stained region on the right.	89
5.18	(<i>a</i>) Water is flowed through a large-bore inlet, while the peptide solution is in the small-bore inlet path. (<i>b</i>) Peptide solution is infused into the device, causing pressure to build up and expand the large-bore inlet tubing. (<i>c</i>) The syringe pump infusing the peptide is stopped and pressure in the small-bore path falls. The tubing in the large-bore inlet path contracts and causes water to flow into the device.	90
5.19	Schematic of setup for the micron-scale viscosity experiment	93
5.20	A plot of the normalized center stream width as a function of the viscosity ratio $\mu_{\text{center}}:\mu_{\text{side}}$	95
5.21	Schematic of the setup for the micron-scale membrane forming experiment designated Micro Experiment Design I- μ	98
5.22	Saline-fluorescein-Congo Red solution was pumped into the two side channels through S_S 's while water was infused through the center channel	99
5.23	Laminar flow and an unclogged device were verified.	100
5.24	Water was flowed through the device until fluorescein dye was no longer visible.	100
5.25	When solution is pumped through a small-bore inlet and stopped, then solution is infused through the large-bore inlet, solution in the small-bore path should be present right up to the intersection of the two flows, not accounting for diffusion effects.	101
5.26	Peptide was infused through the center channel while water was flowed through the side channels.	101
5.27	t = 0:31. A thin ‘skin’ appeared to form on the outside surfaces of the center peptide stream.	103
5.28	t = 0:41. Infusing flow rates were reduced to allow further gelation of the peptide solution.	103
5.29	t = 1:28. The peptide gel ‘skin’ appeared quite thick with distinct edges.	104

5.30	t = 6:05. The dark gelled regions appeared to wash away, leaving transparent Congo Red-stained structures.	104
5.31	t = 4:54:15. No further gelling was observed. Peptide solution was no longer present in the device.	105
5.32	t = 0:15 from July 24, 2001, trial 4. The peptide solution formed a dark gel on the surfaces of the peptide stream that were exposed to saline.	105
5.33	t = 3:13 from July 24, 2001, trial 4. The dark gel appeared to wash away, leaving thin, transparent Congo Red-stained gel 'skins.' The 'skins' seemed to be a barrier to fluorescein.	106
5.34	t = 4:24 from July 24, 2001, trial 4. The gel structure was nearly invisible.	106
5.35	(a) Air bubbles may be hidden in the stainless steel large-bore tubing of a plugged inlet. (b) As fluid is pumped through the small-bore inlet, the pressure caused by resistance in the device causes the air bubble to contract. (c) When the pump is stopped, the air bubble expands, driving fluid through the device.	107
5.36	Schematic of the setup for the micron-scale membrane forming experiment designated Micro Experiment Design II-μ	109
6.1	Inlet and outlet channels become deeper and wider away from the converged-channel device area.	115
6.2	A plot of pressure versus width for various channel depths. The smallest pressure for inlet and outlet channels calculated here was 3.44 mm H ₂ O for 2000x100 μm channels	116
6.3	A wider channel results in a larger volume of diluted solution due to diffusion.	116
6.4	The edges of the peptide stream have gelled, but the center appears to be a fluid.	117
6.5	A vector plot of the velocity profile for channel widths 24-12-24 μm, $\mu_{\text{saline}}:\mu_{\text{peptide}} = 1:1$, and $Q_{\text{saline}}:Q_{\text{peptide}} = 1.38:1$	118
6.6	An isometric vector plot of the velocity profile for channel widths 24-12-24 μm, $\mu_{\text{saline}}:\mu_{\text{peptide}} = 1:1$, and $Q_{\text{saline}}:Q_{\text{peptide}} = 1.38:1$	118
6.7	A band plot of the concentration profile of saline for a device with channel widths 24-12-24 μm	119
6.8	A vector plot of the velocity profile for channel widths 24-6-24 μm, $\mu_{\text{saline}}:\mu_{\text{peptide}} = 1:1$, and $Q_{\text{saline}}:Q_{\text{peptide}} = 2.59:1$	119
6.9	An isometric vector plot of the velocity profile for channel widths 24-6-24 μm, $\mu_{\text{saline}}:\mu_{\text{peptide}} = 1:1$, and $Q_{\text{saline}}:Q_{\text{peptide}} = 2.59:1$	120
6.10	A band plot of the concentration profile of saline for a device with channel widths 24-6-24 μm	120
6.11	(a) Dye of known diffusivity and molecular size is flowed into one channel, water in the other. Flow is stopped in both channels, and the change in concentration density as (b) the dye diffuses through the peptide gel and (c) into the water-filled channel is observed by measuring the intensity of fluorescence over time.	122
6.12	A pressure gradient is set up across the membrane. The red box is a detail view of the converged-channel area.	122
6.13	Top view of the converged-channel area. The co-culture area (green) can be treated to be "sticky" to cells. The light gray areas can be treated to resist cell adhesion.	123

6.14	Revised Fc1 showing new fluidic paths. Detail of converged-channel area, fluid paths are labeled: the current-design center and side inlets, C_I and S_I 's; the current-design center and side outlets, C_O and S_O 's; the new auxiliary inlets and outlets, A_I 's and A_O 's.	124
6.15	Cells are flowed into the device in suspension; they are flowed in through the S_I 's and out through S_O 's.	124
6.16	Cells are flushed from the inlet and outlet channels; fluid is flowed in through the A_I 's and A_O 's, and out through the S_I 's and S_O 's.	125
A2.1	Cross-section of the channel, showing the side of the channel adjacent to the membrane	136
A2.2	The stretched geometry of the membrane	141
A3.1	Layout for silicon wafer pattern. Horizontal and vertical axes are not part of the pattern. Diameter of the wafer is 10.0 cm.	142
A3.2	Detail view of the layout for device Fc1	143
A3.3	Layout for glass wafer pattern. Horizontal and vertical axes are not part of the pattern. Diameter of the wafer is 10.0 cm.	143
A3.4	Machine drawing for large-bore fluidic fitting	144
A3.5	Cross-section of the large-bore fluidic fitting, showing locations of epoxy	144
A3.6	Machine drawing for small-bore fluidic fitting, base	145
A3.7	Machine drawing for small-bore fluidic fitting, tube	146
A3.8	Cross-section of the small-bore fluidic fitting, showing location of epoxy	146
A3.9	Drawing of the adhesive gasket	146
A3.10	Assembly of the adhesive gasket, part 1	147
A3.11	Assembly of the adhesive gasket, part 2	147
A3.12	Exploded view, showing the location of the adhesive gasket between the glass-silicon device and the fluidic fitting	148
A3.13	Standard PHD 2000 with 4 syringe rack	148
A3.14	PHD 2000 Push/Pull Syringe Pump	149
A3.15	Exploded-assembly drawing of the Harvard PHD2000 Push-Pull Pump Modifications	150
A3.16	Rail Slider, modification of an existing part	151
A3.17	Lower Clamp Plate, modification of an existing part	151
A3.18	Sliding Clamp Plate, modification of an existing part	152
A3.19	Position Plate, modification of an existing part	152
A3.20	Clamp Rack, modification of an existing part	153
A3.21	Piston Retaining Bracket, new part, sheet 1 of 2	153
A3.22	Piston Retaining Bracket, sheet 2 of 2	154
A3.23	Clamp Rack Standoff, new part	154
A4.1	Mass vs. volume for 1.0 weight percent KFE8 solution	155
A4.2	Viscosity vs. shear rate for 1.0 weight percent KFE8 solution	156
A5.1	Scanning-electron microscope image of the cross-section of an etched silicon channel. The dimensions are different from those used in this study, but the curvature at the bottom of the channel will exist in our fabricated geometries. (Image courtesy of Joe Ricker, The Charles Stark Draper Laboratory, Cambridge, MA)	176

A5.2	An image of the device showing the measurement of the channel (<i>left</i>) and the center stream (<i>right</i>). The fluid is flowing from right to left in this image.	177
A5.3	Drawings of (a) the assumed-geometry, used in the analytic solution, and (b) the actual geometry formed in the etch process	178
A5.4	The standard deviation for data sets $n=6$ and $n=5$, for a range of adjustment factors	179
A5.5	The single-syringe pressure release fixture	180
A5.6	The saline pressure release fixture. The black base represents the syringe mounting block of the syringe pump.	180
A5.7	The saline pressure release fixture, shown in the open position	181
A5.8	The saline pressure release fixture in the closed position	181
A5.9	2x Clamp Plate	182
A5.10	Clamp Lever	183
A5.11	Harvard Pump Modification	183

List of Tables

2.1	Design parameters for the micron-scale fluidic devices and ranges of values	32
2.2	Mechanical properties of 10 mg/ml KFE8 peptide gel	38
2.3	Dimensions and syringes combinations for devices Fc1-Fc8, critical pressures for the gel membrane in these devices, and estimated times for salt to diffuse into the peptide stream	44
2.4	Comparison of $100 \times (\text{critical pressures}) / (\text{pressure required for flow})$ for the devices at physiologic average fluid velocities	44
2.5	Design motivations for the devices	47
5.1	Flow rate data for the micron-scale viscosity experiment	95
5.2	Calculated viscosity values from center stream measurements	96
5.3	Quantitative outline of the micron-scale membrane forming experiment	99
A4.1	Density data for a 1.0 weight percent KFE8 solution	155
A4.2	Calculated error for the MATLAB model with varying mesh size	165
A4.3	Calculated error for the MATLAB model with varying n in the series expansion	165
A4.4	Tabulation of the total molecular volume of a KFE8 monomer	170
A4.5	Tabulation of the total molecular volume of a KFE8 intermediate	170
A4.6	Tabulation of the total molecular volume of a KFE8 filament	170
A4.7	Parameters for the normalized numerical models	174

Chapter 1

Introduction

1.1 Background

1.1.1 Tissue Engineering

There are currently over 80,000 patients on the waiting list for complex internal organs [26]. For these patients, options include extra-corporeal assist devices (such as kidney dialysis treatments) and artificial replacement devices (*e.g.*, artificial heart). For some conditions, such as severe liver failure, transplantation is the only viable option. Annually in the U.S., 3500 patients undergo liver transplantation, while 30,000 seeking transplants will die [21]. To deal with the gross inequality between supply and demand of available donor organs, tissue engineering is the most logical and promising potential solution.

In the field of tissue engineering, several types of non-vascular tissues have been grown *in vitro* and successfully implanted in human patients (skin and cartilage) and animal models (bone marrow) [12]. However, thick, complex organs have posed a greater challenge. For these tissues the radius of the organ exceeds diffusional length scales for oxygen and nutrients (approximately 150 micrometers). Vascular networks must be incorporated into these engineered organs to deliver these materials to cells deep within this tissue, via cell culture medium (*in vitro*) or blood (*in vivo*). This study will focus on tissue engineering efforts for a specific organ of this type, the liver.

1.1.2 The Liver

The main functions of the liver involve the handling of nutrients and pollutants, which are passed into the liver through the bloodstream; the liver is also important in acting as a reservoir that regulates the supply of blood to the body.

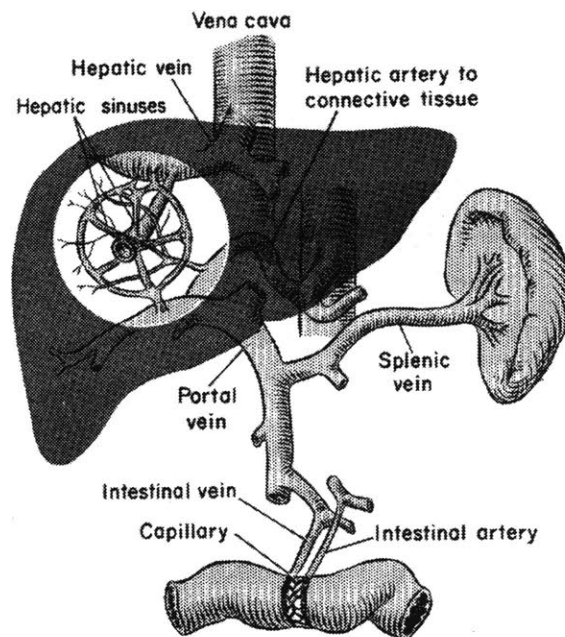


Figure 1.1. Diagram of the liver [14]

The liver has two blood supplies: the hepatic artery, which supplies nutrients and oxygen to the liver cells; and the portal vein, which collects the blood that leaves the spleen, stomach, small and large intestine, gall bladder, and pancreas, and carries it to the liver, where nutrients and toxins are processed (Figure 1.1) [6].

When blood enters the liver through the portal vein, the liver vasculature branches into smaller and smaller channels, down to the capillary level (Figure 1.2).

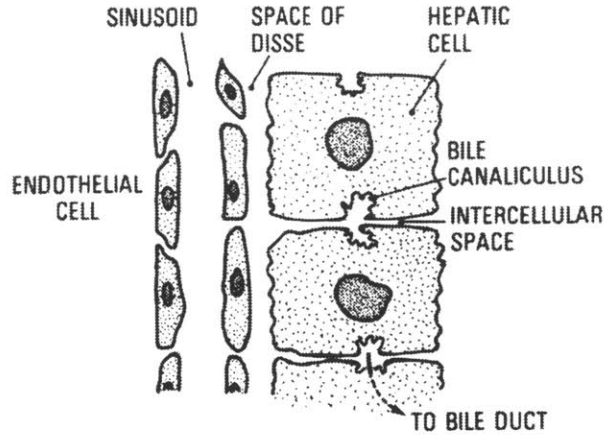


Figure 1.2. Cross-section view of a sinusoid and the adjacent hepatocytes [11]

Material and fluid exchange occurs between the sinusoids, which are specialized capillaries formed by loosely-connected fenestrated endothelial cells, and the hepatocytes. Material transport of nutrients and toxic substances occurs by osmosis and diffusion from the sinusoid, across the Space of Disse (width of 1 micron or less) and other intracellular spaces, through the hepatocyte cell membrane [11]. Blood flows out of the sinusoids and into larger and larger veins, leaving the liver through the vena cava. The hepatocytes secrete wastes as bile into the bile canaliculi. The bile canaliculi are connected to bile ducts, which empty into the gastrointestinal tract.

1.1.3 Growing Cells and Co-Culture

Culturing cells for the purpose of tissue engineering requires control over cell morphology and function. For an engineered liver, the important cell types to consider are the cells that form the vasculature (endothelial cells) and the parenchymal cells (hepatocytes). For these cell types, the environment can be controlled to achieve the desired cell expression, that of capillaries and functioning liver tissue.

Given the proper environment, endothelial cells in culture will form capillary-like structures. One approach to capillary formation is to fabricate a microfluidic network of channels, then grow endothelial cells on the inner walls of the channels. The channels are coated with cell-adhesion molecules, and then endothelial cells in suspension are dynamically seeded and cultured in the network. Endothelial cells have been shown to successfully adhere to and be cultured in micro-channels for more than 4 weeks [5].

Furthermore, endothelial cells can develop capillary-like morphology on a flat substrate through control of the cell-adhesion regions. Dike *et al.* patterned hydrophilic lines of various widths onto otherwise hydrophobic treated gold-plated glass slides [10]. Fibronectin was deposited onto the hydrophilic regions; endothelial cells were then seeded onto the fibronectin lines and cultured. On 30 micrometer and wider lines, the endothelial cells spread out and grew in a flat sheet. On 10 micrometer lines (typical capillary width), the cells lined up one or two cell widths along the length of the line and rolled up into three-dimensional capillary-like structures.

It is now common knowledge that mesenchymal cells should be co-cultured with hepatocytes to improve hepatocyte viability *in vitro* [31]. Hepatocytes in co-culture with mesenchymal cell types (endothelial cells, fibroblasts, and others) exhibit prolonged morphologic and functional differentiation characteristics that are quickly lost when hepatocytes are cultured alone [2]. Studies have demonstrated co-culture in various two- and three-dimensional configurations, with many variables, including randomly-mixed cells, segregated cells, static culture, continuous perfusion culture, and different chemical environments [4,13].

1.1.4 Previous Work

The main obstacle to building a tissue-engineered liver for implantation is the challenge of creating vasculature *in vitro*. One strategy is to take advantage of existing vascular beds in the patient, injecting or implanting cells directly into these areas [30]. While this approach has shown some short-term success in the liver, in the long run it does not result in a healthy organ, and the approach is useless for organs with less-extensive vascular beds. Very promising results have been achieved by the use of angiogenesis growth factors to promote blood vessel formation in *in vitro* cell cultures [27]. Still, this process is limited by the speed of blood vessel formation. Another means to achieve vascularized liver tissue is to use microfabrication technology to create geometries that promote blood vessel formation. Several strategies employ varying degrees of scale and imposed structure to achieve this goal.

One approach focuses on developing a vascularized “mini-liver” *in vitro* [13]. Mixtures of endothelial cells and hepatocytes are cultured in microfabricated wells (~300 micrometers in diameter by 200 micrometers deep) through which cell culture medium is perfused. The cells self-organize, driven by surface-adhesion effects, and form globules of liver cells surrounded by endothelial cells. As these globules adhere to each other and to the walls of the channel, the interstitial spaces are lined with endothelial cells and resemble the inner walls of capillaries. Perfusion of cell-culture medium through the crevices between the globules simulates blood flow through capillaries [12].

The other approach seeks to build organ-scale liver tissue by stacking large (10 centimeters in diameter) layers of two-dimensional vasculature and cultivated sheets of hepatocytes [12,19]. The vascular layers are fabricated by culturing endothelial cells in precision-machined branching fluidic channels modeled after physiologic capillary networks,

made from degradable polymers using MEMS technology. These vascular sheets are stacked in alternating layers with layers of hepatocytes, and the vascular sheets are connected to form a three-dimensional fluidic network. The endothelial cells form blood vessels and capillaries within the channels. As the blood vessels and hepatocytes develop, they produce extra-cellular matrix to provide structural integrity as the biodegradable networks break down [28].

1.2 Enabling Technologies

1.2.1 Self-Assembling Oligopeptide

A new biomaterial, a porous hydrogel (a three-dimensional network of hydrophilic polymers) made of self-assembling oligopeptides, shows potential as a scaffold for engineered tissue [34]. This recently identified class of oligopeptides consists of short amino acid sequences consisting of alternating hydrophilic and hydrophobic residues that join in β -sheet conformation to form long helical ribbon-like strands in solution. These strands bundle together into filaments. When either the ionic strength of the solution is above a certain threshold so that the charges are effectively screened, or the pH of the solution causes the net charge on the molecules to be nearly zero, the filaments cross-link to form a hydrogel [25]. The peptides self-assemble into a lattice of fibers with a matrix density that is dependent on the peptide concentration [24]. The peptide gel elicits no immune response when injected into laboratory animals, and has been shown to support viable cultures of several cell types [18,23,33]. The matrices are fragile, but the self-assembling property can be used to construct gel structures with minimal handling. Furthermore, after cell attachment, the natural matrices produced by the cells help increase membrane stability.

1.2.2 MicroElectroMechanical Systems (MEMS)

MEMS microfabrication technology is well suited to machining geometries on the scale of cells and capillaries. Microlithography and etching techniques allow one to manufacture three-dimensional features with in-plane resolution of ± 0.1 micrometers for features up to 40 micrometers deep, either by patterning directly onto flat substrates (generally silicon or Pyrex wafers), or by creating molds for polymer casting [5,22]. Different processes can alter the substrate surface chemistry from hydrophobic to hydrophilic, and can be used to control cell adhesion.

1.3 Objectives and Scope of This Study

The objective of this thesis was to design and fabricate a bioreactor for co-culture of endothelial and hepatic parenchymal cells mimicking the *in vivo* characteristics of the smallest functional unit of the liver, a single capillary and the adjacent hepatocytes, i.e. a 'capillary-parenchymal element' ('CPE', see Figure 1.3).

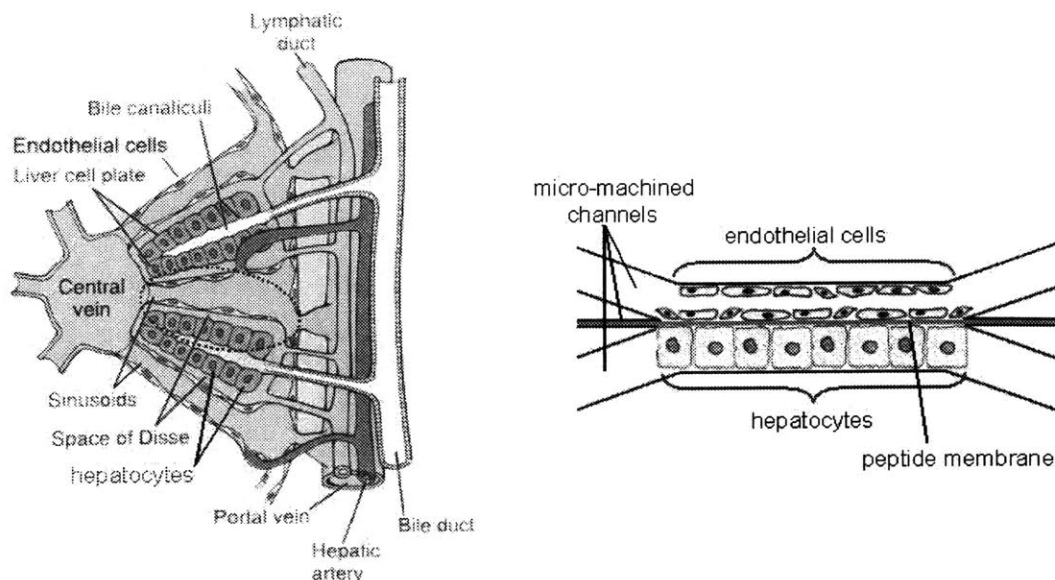


Figure 1.3. A diagram of the cellular and vascular organization of the liver [16] (*left*), and a section diagram of the proposed bioreactor (*right*)

The need to understand the cell-cell interactions that occur at this most basic unit of the liver is the motivation for this work. Knowledge gained from the study of these interactions in the bioreactor can be applied to the development of tissue-engineered replacement organs. The co-culture bioreactor consists of two cell-scale fluid channels separated by a thin porous membrane made of self-assembling oligopeptide hydrogel. This approach is distinguished from other small-scale co-culture studies by the highly specified geometry of the bioreactor; this is significant, as cell expression and morphology are affected and in some cases dictated by the geometry of the cell environment [10].

Additionally, this study is among the first applications of a new biomaterial, the self-assembling peptide. The bioreactor exploits the characteristics of the peptide to form the hydrogel in a unique fashion. This study aims to promote and expand the tissue-engineering applications of the peptide.

The design of the bioreactor was guided by physiologic data, as well as by the constraints of the materials and instrumentation. Fluid and solid mechanics analysis of the device was performed to aid in the design of the bioreactor geometry (Chapter 2). Standard MEMS microfabrication technologies were used to construct the micro-fluidic component of the devices, while precision-machined parts were used to interface the micro-fluidic components to high-precision fluid control instrumentation (Chapter 3). Analytic and finite element modeling (FEM) techniques were employed to model fluid flow and mass transfer in the device to estimate the optimal parameters, to be implemented in the gel membrane-forming experiments (Chapter 4). The experimental work focused on forming a gel membrane between two capillary-scale channels. To fabricate the membrane, protocols and procedures were developed to initiate gelation of the peptide in previously untried conditions and geometries. Promising precursors to

a gel membrane were achieved (Chapter 5). Continuing efforts to understand the gelling process, and well as to fabricate the gel, are required to successfully construct the bioreactor (Chapter 6).

Innovative achievements in this study include the unique design of the bioreactor, specifically: the use of highly specified geometry to promote capillary growth, and the scale of the bioreactor to study the interactions between a single capillary and the adjacent hepatocytes. The method by which the gel is formed is novel, as are the accompanying results from the numerical mass transfer models and experiments. These results provoke further investigation into the nature of the gelling process of the peptide.

This page intentionally left blank.

Device Design

The proposed device for co-culture of a capillary-parenchymal element (CPE) consists of two capillary-scale fluidic channels in parallel, separated by a membrane made of porous self-assembling oligopeptide matrix. Silicon and glass MEMS fabrication processes were used to fabricate the micron-scale geometry of the devices. This micron-scale substructure was connected to macro-scale devices, including syringe pumps to control fluid flow through the device, and an optical microscope to record images of the device and peptide matrix formation. The design of the micron-scale geometry was determined by the physics of the materials and the available micro-machining technology, as well as by constraints and requirements of the macro-scale devices. Solid and fluid mechanics analysis was used to consider the effects of pressure and flow-induced stresses on the peptide membrane, and to determine its optimal dimensions. Choosing the dimensions of the side channels required consideration of the physiology (dimensions of the liver capillaries (sinusoids) and hepatocytes) as well as the flow rate ratios available from the syringe pumps. The inlet and outlet channels were designed to allow sufficient visibility of the converged-channel device area with the microscope, while maximizing the number of devices on a single silicon wafer to minimize cost.

2.1 Device Concept

The device concept was to form a peptide gel membrane between two cell-sized channels by first flowing peptide solution between the two channels, then flowing saline in the two side channels to cause the peptide solution to gel. Design of the bioreactor was directed by the physiology of the liver, the properties of the peptide gel, and characteristics of the gel-forming process. The following procedure was proposed for forming the gel membrane:

- A device is constructed consisting of three channels that converge into a single wide, long channel, which diverges back into three channels (Figure 2.1). The channels are completely filled with water.

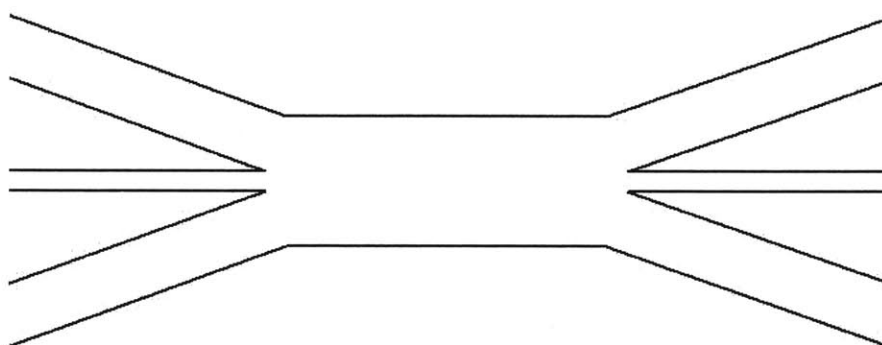


Figure 2.1. Top view of the device; the channels are completely filled with water.

- Under laminar flow conditions, self-assembling peptide solution is flowed through the center channel of the device, while water is flowed through the side channels (Figure 2.2).

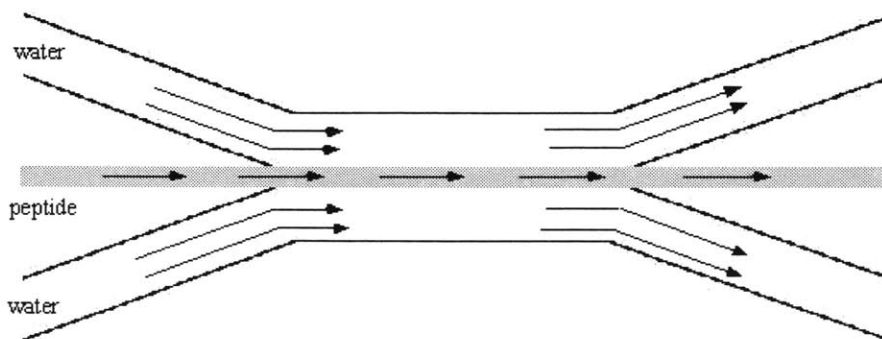


Figure 2.2. Self-assembling peptide solution is flowed through the center channel of the device, while water is flowed through the side channels.

- A saline solution consisting of sodium salt, fluorescein salt (a fluorescent dye for flow visualization) and Congo Red (a stain that binds to the β -sheet structures formed by the peptide for visualization of the gel) is introduced into the side channel flows (Figure 2.3).

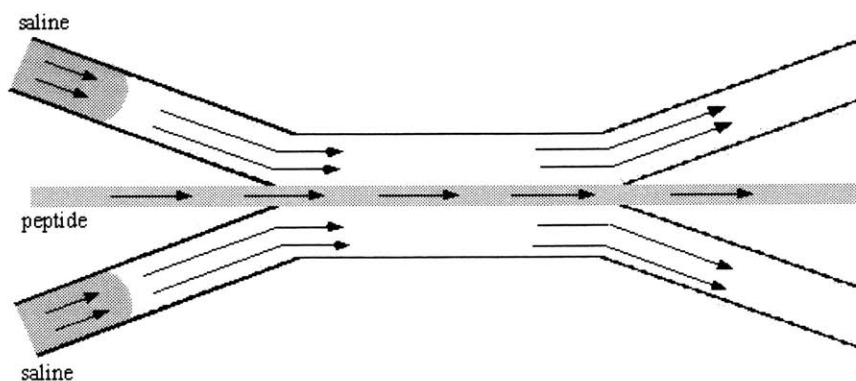


Figure 2.3. Saline solution is added to the side channel flow.

- As the saline comes into contact with the peptide solution, the ionic strength of the peptide solution rises above the threshold so that the charges are effectively screened, and the peptide solution begins to form a gel at the fluid interfaces. At this point, all the flow streams are stopped to allow complete gelation to occur undisturbed by the flow (Figure 2.4).

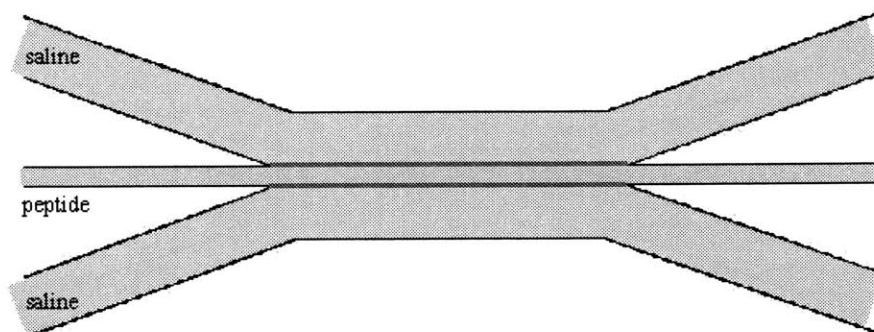


Figure 2.4. The peptide solution begins to form a gel at the fluid interfaces.

- Saline diffuses through the gel and into the peptide solution, and the rest of the peptide solution forms a gel between the two saline-filled channels (Figure 2.5).

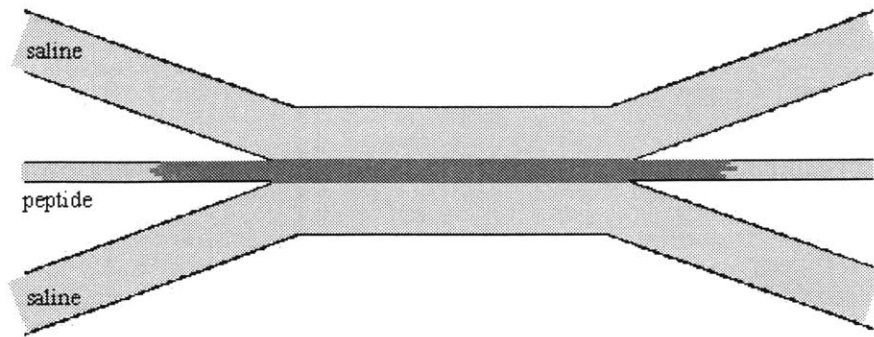


Figure 2.5. The peptide solution forms a full gel between the two saline-filled channels.

- The saline-fluorescein-Congo Red solution is flushed out of the device with water, leaving a peptide gel membrane separating the two parallel channels.

Once a stable gel is formed, characterization measurements can be made. For example, a chemical or pressure gradient can be imposed across the membrane to investigate its conductivity and mechanical properties. To use the device for cell seeding, cell adhesion molecules, such as fibronectin, can be flowed in solution through the channels to make the surfaces “sticky” to cells. One channel may then be seeded with endothelial cells and the other with hepatocytes (Figure 2.6).

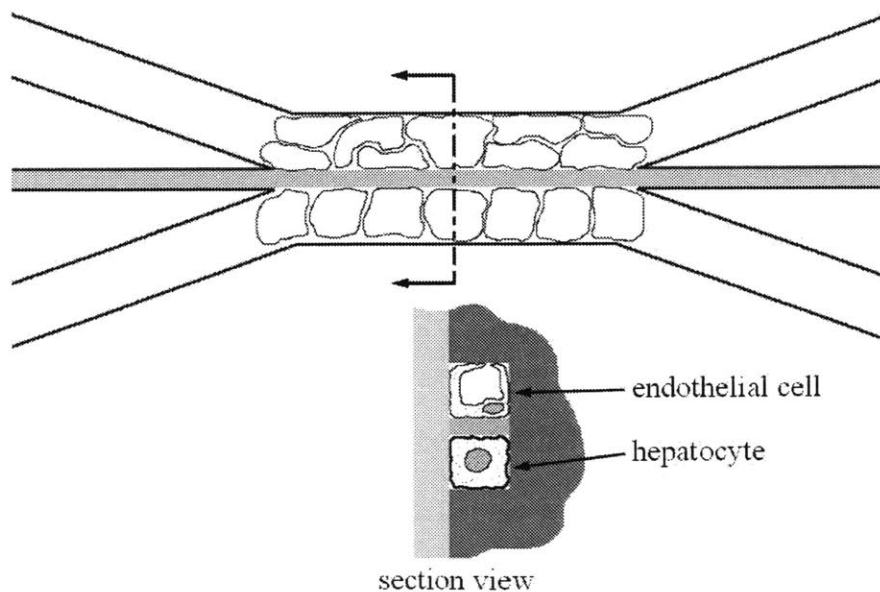


Figure 2.6. Diagram showing cells in culture in the device. The section view shows the endothelial cells in the morphological configuration of a capillary.

Oxygenated cell culture medium is flowed through each channel, and the system is incubated. The geometry of the capillary channel is designed to give the endothelial cells mechanical cues to promote capillary formation. Hepatocytes can adhere to the membrane and the walls of the other channel. Once the liver cells and endothelial cells have successfully grown and developed, the capillary is then supplied with oxygenated cell culture medium. The cell culture medium on the hepatocyte side is replaced with a non-nourishing fluid (“pseudo-bile”) to remove waste products from the cells. The hepatocytes are sustained by diffusion of oxygen and nutrients through the capillary wall and peptide membrane.

The design variables for the micron-scale geometry are the width and depth of each channel, and the length of the device area (see Figure 2.7). The dimensions of the side channels are based on the dimensions of endothelial cells (channel a , see Table 2.1) and hepatocytes (channel b). The center channel (channel c) is sized to the width of the desired membrane, which must possess adequate strength while allowing for material transport between the two side channels.

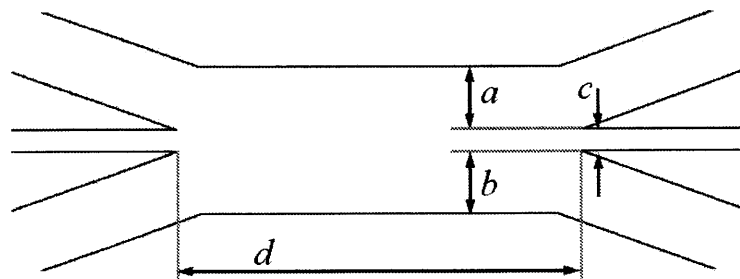


Figure 2.7. Schematic of the device, showing key dimensions

Table 2.1. Design parameters for the micron-scale fluidic devices and ranges of values

Design Area	Geometric parameters	Based on	Range of values
device area	length	length of capillary	0.3 – 1 mm [15]
channel <i>a</i>	width and depth	dimensions of sinusoids	7 – 15 μm in diameter; average 10 μm [1]
channel <i>b</i>	width and depth	dimensions of hepatocytes	13 – 30 μm in diameter; average 25 μm [1]
channel <i>c</i>	width and depth	width of the Space of Disse and material properties of the peptide gel: strength, conductivity, etc.	Dependent on fluid and pressure variables

2.2 Material Selection

Fabrication of the micron-scale fluidic device employed established MEMS technology, based on an etched silicon wafer bonded to a drilled glass wafer. The silicon paradigm has been used extensively in the area of microfluidics and tissue engineering, and surface chemistry modification techniques for cell seeding and culture are well-established [4,5,10]. These types of fluidic networks are also often made of elastic polymers, the most commonly used being poly(dimethylsiloxane) (PDMS). These polymers can be used to manufacture devices quickly and cheaply, but have the disadvantage of being highly compliant. Fluid flow at physiologic flow rates through long channels with cross-sectional dimensions that are on the size scale of capillaries generates high pressures. The inherent compliance of a non-rigid polymer device causes the device to deform and expand under high pressures. This compliance causes the device to act as a fluid capacitor, introducing transient effects on flow rates that need to be well-controlled. A glass-silicon device is considerably more rigid than a molded polymer device and reduces these effects. Furthermore, the silicon-glass paradigm is readily available and well-established in the Draper Laboratory MEMS fabrication facility, where most of the work in this study was performed.

In this study, the peptide sequence KFE8 used to form the hydrogel membrane (synthesized by the BioPolymers Lab at MIT, Cambridge, MA). This peptide was chosen due to its similarity to another peptide sequence for which mechanical property data was available (discussed in Section 2.3.3). ‘KFE’ refers to the side chains of the amino acids that make up the peptide: Lysine (K), positively charged and hydrophilic; phenylalanine (F), non-polar and hydrophobic; and glutamic acid (E), negatively charged and hydrophilic. ‘8’ refers to the number of amino acids in the peptide. Thus, KFE8 corresponds to the sequence ‘FKFEFKFE’.

2.3 Membrane Design: Stress Analysis

The purpose of the gel membrane is to provide a permeable fourth “wall” to channel *a* so that the endothelial cells have four continuous walls to adhere to and form a capillary. Prior to cell seeding, the inside walls of the capillary channel are treated with cell-adhesion molecules to promote cell attachment (see Section 6.5.1). Ideally, the gel would have a thickness close to the width of the Space of Disse (≤ 1 micron, see Figure 1.2). The minimum width of the gel is determined by the strength of material, and flow and pressure conditions in the channels. The gel membrane experiences both shear stress from flow in channels *a* and *b*, and normal and in-plane stresses resulting from pressure differences across opposite sides of the membrane. Quantitative analysis of these effects guides the design of the gel dimensions.

2.3.1 Flow-Induced Stress

The gel membrane experiences shear stress from the fluid flow in the side channels. The stress on the gel will be highest along its edges (Figure 2.8).

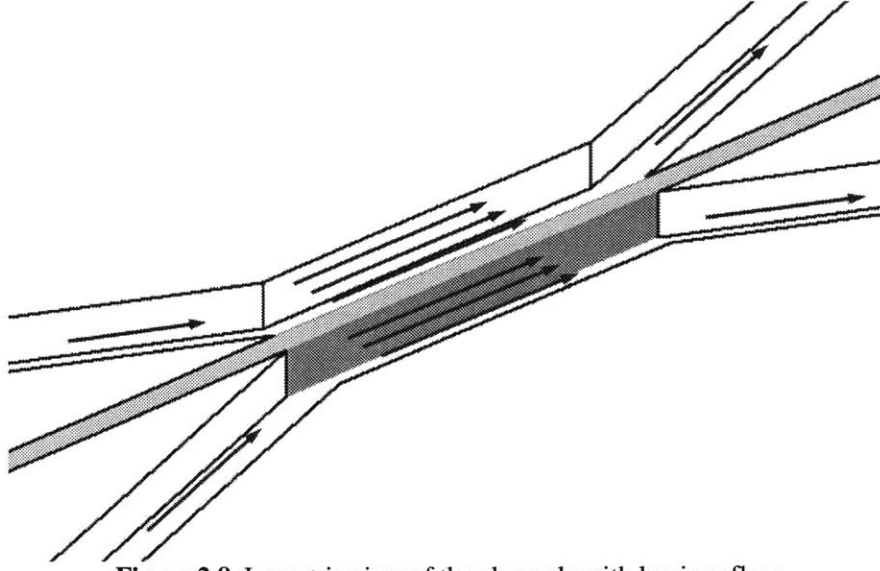


Figure 2.8. Isometric view of the channels with laminar flow

A simple force balance shows that

Total Force on the membrane = Σ reaction forces from edges 1,2,3,4 (see Figure 2.9).

In the worst-case scenario, the gel will be in tension, held only by edge 1.

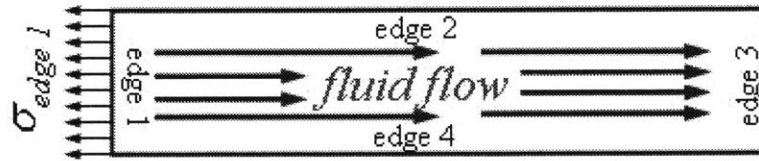


Figure 2.9. Forces on the membrane

The stress over the area where the gel is attached to edge 1 is

$$\sigma = \frac{F_{tot}}{t \cdot h}, \quad (2.1)$$

where F_{tot} is the total force on the membrane, t is the thickness of the membrane, and h is the height of the membrane. The Navier-Stokes equation for fully-developed fluid flow in one of the channels is solved and the shear stress calculated, then integrated over the membrane area to give the force on one side of the membrane (Figure 2.10).

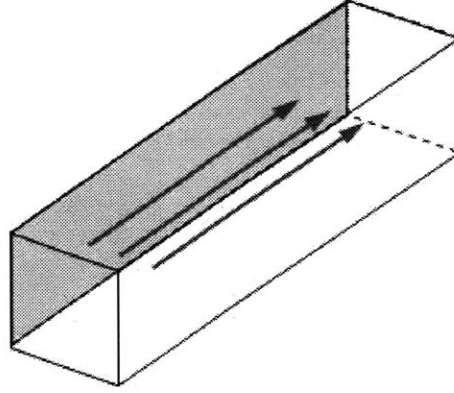


Figure 2.10. Flow in a rectangular channel; the gray wall represents the membrane.

Equal flow is assumed on both sides of the membrane, so by symmetry this result, multiplied by 2, gives an estimate of the total force on the membrane (F_{tot}) from the fluid shear stress on both sides of the membrane (see Appendix A2.1 for the full derivation). The total force on the membrane is

$$F_{tot} = 2F_{one\ side} = 4L \int_0^{z_c} \mu \frac{du}{dy} dz. \quad (2.2)$$

Choosing flow conditions, the height and length of the gel, and using the maximum strength of the gel (σ_{max} , from the known mechanical properties of the material, see Table 2.2), the minimum necessary thickness of the gel is given by

$$t_{min} = \frac{F_{tot}}{\sigma_{max} \cdot h}. \quad (2.3)$$

2.3.2 Stresses Due to Pressure Differences Across the Membrane

Stress on the membrane also occurs when there is a pressure gradient across the membrane (Figure 2.11). When the membrane deforms, it will bow towards the side with the lower pressure.

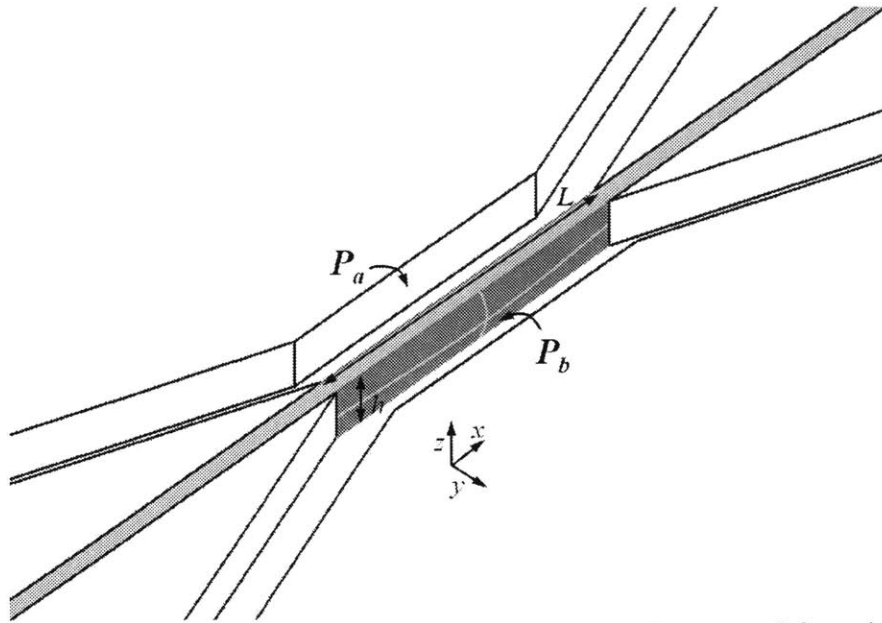


Figure 2.11. A pressure gradient across the membrane ($P_a > P_b$) causes deformation.

In-plane stresses will occur due to bending and membrane tension. If the stresses are separated into x and z components, the maximum stresses will occur along the shorter dimension h .

2.3.2.1 Bending

A vertical cross section of the membrane can be modeled as a beam-bending problem (Figure 2.12):

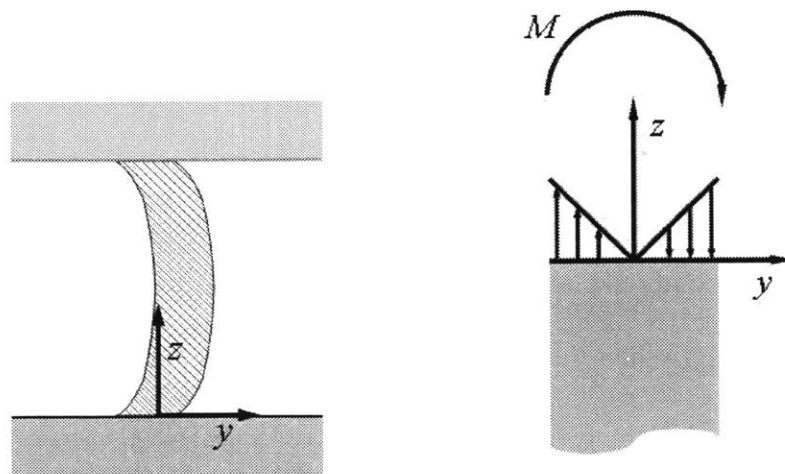


Figure 2.12. A section view of the deformed membrane, attached to the top (glass) and bottom (silicon) surfaces of a channel (*left*); a diagram showing the stress distribution in the membrane and the bending moment (*right*)

From the stress analysis, the maximum curvature of the beam occurs at $z = 0, h$ (see Appendix A2.2 for the full derivation). Across this section, the maximum σ_z values occur at $y = \pm \frac{1}{2}$. For $h=0, y = \frac{1}{2}$, and $\sigma_z = \sigma_{max}$ (the material fracture strength), one can calculate the critical pressure ΔP_{crit} at which the membrane will break.

2.3.2.2 Surface Tension

In addition to bending, pressure differences across the membrane will cause it to bow in the direction of lower pressure. This bowing will stretch and strain the membrane (see Figure 2.13).

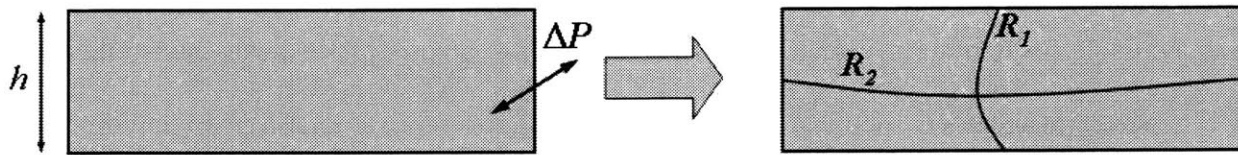


Figure 2.13. A pressure difference across the membrane causes the membrane to bow.

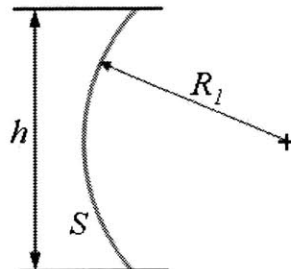


Figure 2.14. The stretched geometry of the membrane

Figure 2.14 shows the stretched geometry of a vertical cross-section of the membrane (represented by the gray line). From an original dimension of h , the membrane has stretched to length S . If the membrane is thin, the stresses due to in-plane strain can be approximated as uniform across the thickness of the membrane. The Laplace equation can be used to determine the critical pressure difference across the membrane that will cause failure due to this strain (see

Appendix A2.3 for the full derivation). From the maximum strain of the material, ϵ_{\max} , the minimum radius of curvature can be determined. The ΔP_{crit} calculated with this radius value, R , is the critical pressure that will generate critical strains and stresses, breaking the gel, and is given by

$$\Delta P_{\text{crit}} = \frac{\sigma_{\max} t}{R}. \quad (2.4)$$

2.3.3 Micron-Scale Design: Stress Analysis Results

The self-assembling peptide used in this study was KFE8. Due to the recent discovery of these materials, data for the mechanical properties of a KFE8 hydrogel were not available. Data was available for another peptide, EFK8, for which the synthesis process was less robust. The two peptides share nearly identical sequences; the only difference is that a phenylalanine (F) in EFK8 (KFEFKFEF) is pulled from the end of the sequence and placed at the beginning of the KFE8 (FKFEFKFE) sequence. The similarities of the peptides are such that similar mechanical properties can be assumed. The material properties for the EFK8 peptide at a concentration of 10 mg/ml (~1 weight percent) are listed in Table 2.2. These values were used in the stress analysis calculations.

Table 2.2. Mechanical properties of 10 mg/ml KFE8 peptide gel [24]

Young's modulus, E	14,700 Pa
Max. elongation, ϵ_{\max}	0.012 (1.2 %)
Fracture strength, σ_{\max}	196.5 Pa

For the initial calculations, a representative micron-scale device was used with the following dimensions and flow parameters: length $L = 150 \mu\text{m}$, channel widths $a = b = 25 \mu\text{m}$,

$h = 25 \text{ } \mu\text{m}$, average fluid velocity $v_{\text{average}} = 3 \text{ mm/s}$, and the fluid viscosity $\mu_{\text{fluid}} = \mu_{\text{water}} = 0.001 \text{ Pa}\cdot\text{s}$.

2.3.3.1 Flow-Induced Stress Results

Typical average fluid velocity values are on the order of $v_{\text{average}} \sim 3 \text{ mm/s}$. The minimum gel thickness that will not fracture under these conditions is $0.0815 \text{ } \mu\text{m}$ (Figure 2.15).

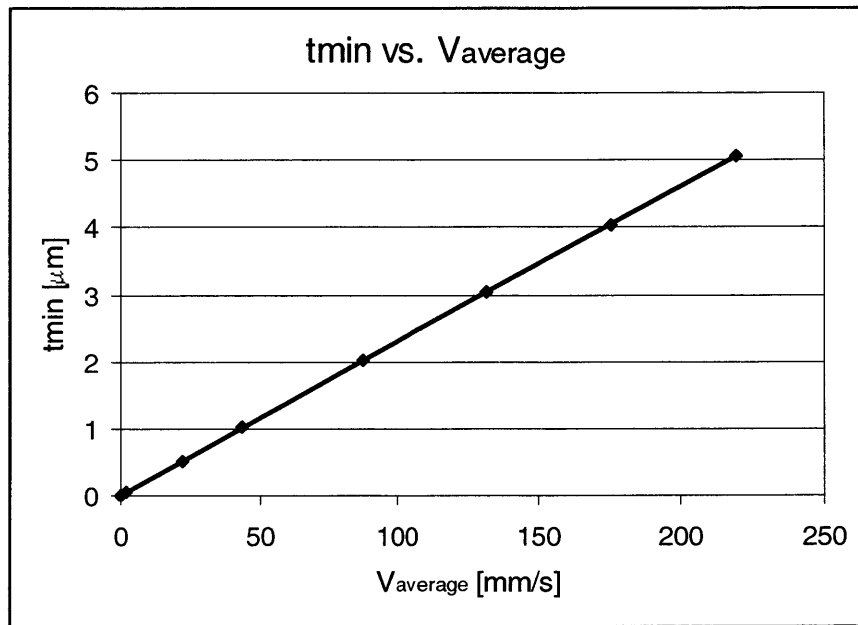


Figure 2.15. A plot of the minimum membrane thickness (t_{min}) for the average velocity of flow in the channels (V_{average}) for a fluid with the viscosity and density of water

An extremely thin gel can withstand surprisingly high flow velocities (for $v_{\text{average}} = 10 \text{ mm/s}$, $t_{\text{min}} = 0.23 \text{ } \mu\text{m}$). The limiting membrane thickness will be determined by ΔP across the membrane, rather than flow-induced shear stress.

2.3.3.2 Pressure Difference-Induced Stress Results

For a range of values for membrane thickness, t , critical pressures that will cause the gel to rupture for both bending effects and surface tension-induced strain were calculated, and the smaller ΔP_{crit} value was identified. For values of t less than 10 microns (*i.e.*, in the range of the Space of Disse), these pressures were very small, on the order of a few millimeters of water (Figure 2.16). The minimum membrane thickness will be determined by how well the pressure difference across the membrane can be controlled. The results show that these effects, and not the fluid flow shear stress, will determine the minimum thickness value of the membrane.

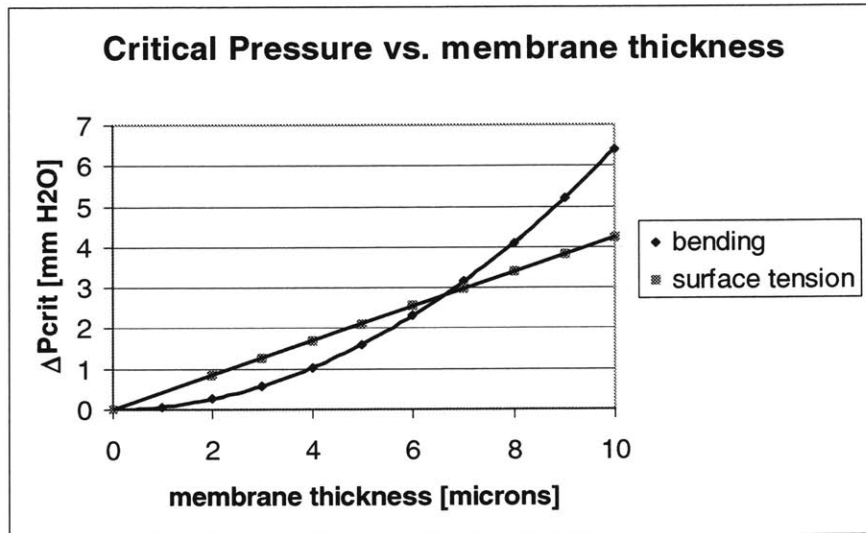


Figure 2.16. The pressure required to fracture the membrane for a range of membrane thicknesses

2.3.4 Transport Considerations

Initially during cell culture, oxygenated cell culture media is to be infused through the channel containing endothelial cells, as well as through the hepatocyte channel. However, once the cell culture is established, oxygenated cell culture medium will flow only through the endothelial cell (“capillary”) channel to mimic the *in vivo* environment. It is important to

determine if oxygen and other nutrients will diffuse through the membrane in sufficient amounts to sustain the viability of the hepatocytes.

For a gel formed from a 10 mg/ml peptide solution (approximately equivalent to a 1 weight percent solution), the pore size is roughly 100 nanometers [24]. The gel is 99% water, so it is assumed that the diffusivity of solute through the gel is the same as through water. In our device, the hepatocytes will line channel b no more than 1 or 2 cells deep (see Figure 2.6). For such a low number of cells, it can be assumed that the rate of oxygen flux across the membrane is greater than or equal to the rate at which oxygen is consumed.

During membrane formation, the rate at which the peptide solution gels depends on how fast the salt ions diffuse into the peptide. If the salt ions are assumed to have the same mobility through the gel as in water, the time required for salt ions to diffuse completely through the peptide stream can be estimated. The approximate diffusional length scale, δ , for a species with diffusivity D is

$$\delta \sim 2\sqrt{D\tau_{diff}} \quad (2.5)$$

where τ_{diff} is the diffusional time scale. The width of the desired membrane, and thus the width of the peptide stream is t . Saline ($D_{NaCl} = 1.483 \times 10^{-5} \text{ cm}^2/\text{s}$ at NaCl concentration = 0.1 M, at 25°C [32]) will infiltrate the peptide stream from both sides, so

$$\delta = \frac{t}{2}. \quad (2.6)$$

Substituting Eq.2.6 into Eq.2.5 gives

$$\tau_{diff} \sim \frac{t^2}{16D}, \quad (2.7)$$

the time for salt to diffuse distance $\frac{t}{2}$ in water (see Table 2.3).

2.4 Macro-Scale Device Design

In the device design of the micron-scale devices, ‘macro-scale’ refers to anything that is outside of the converged-channel region: inlet and outlet channels, hardware, and other instrumentation. Design requirements and constraints at the macro-scale will influence device design parameters at the micron-scale.

2.4.1 Flow Delivery

A standard syringe pump consists of a syringe mount and an actuator, which pushes or pulls the syringe plunger. A single-actuator syringe pump allows multiple syringes to be mounted, but the actuator will move all the attached plungers at the same linear speed. The cross-section dimensions of the channels were chosen so that a single syringe pump pushing multiple syringes could infuse fluids into the channels at equal average velocities. For the trivial case of three equal-dimensioned channels, three identical syringes are attached to the syringe pump. For micron-scale channels with differing dimensions, syringes are chosen that have cross-sectional area ratios that are equal to those of the channels. With this equal average velocity constraint, the finite number of different commercially available syringes limits the possible combinations of channel geometries.

2.4.2 Visibility, Cost Reduction, and Pressure Regulation

The device area must be unobstructed by fluidic fittings or tubing, and there must be sufficient clearance on the top surface of the device to allow close positioning of the objective lens of an optical microscope. This requires that the glass-silicon device inlets and outlets be spaced some distance away from the converged-channel device area; hence, the inlet and outlet

channels will be quite long compared to the dimensions of the membrane-forming area. Additionally, to reduce costs, the outside dimensions of the devices were kept as small as possible to maximize the number of devices that could be laid out on a single 100 mm in diameter silicon wafer.

A side effect of long channels with cross-section dimensions on the order of micrometers is high fluid resistance, and subsequent high pressures. Typical physiologic average fluid velocity through capillaries is ~ 1 mm/s. Membrane-forming experiments can employ average velocity flows ranging from 3 to 12 mm/s. The pressures along the channels will be much larger than the cross-membrane pressure required to fracture the gel (see Table 2.4). Careful control of flow operations across the membrane are required to keep the pressure symmetric and the gel intact. Values of $\% \Delta P_{\text{crit}} / \text{tot } \Delta P_{\text{channels}}$ seem prohibitively small, but experimental results showed that the gels displayed at least temporary stability under similar flow conditions.

2.5 Fabricated Device Specifications

Eight different devices (Fc1 through Fc8) were designed (Table 2.3). $\Delta P_{\text{crit,bending}}$ and $\Delta P_{\text{crit,surface tension}}$ were calculated for the devices using the equations derived in the bending and surface tension analysis. The lower of the two values is highlighted in red.

Table 2.3. Dimensions and syringes combinations for devices Fc1-Fc8, critical pressures for the gel membrane in these devices, and estimated times for salt to diffuse into the peptide stream

	<i>a</i> [μm]	<i>b</i> [μm]	<i>c</i> [μm]	<i>L</i> [μm]	<i>h</i> [μm]	$\Delta P_{crit, bending}$ [mm H ₂ O]	$\Delta P_{crit, surf\ tens.}$ [mm H ₂ O]	ch. area ratios	Syringe sizes* [μl]	$\tau_{diff, salt}$ [sec]
Fc1	24	24	24	100	24	40.10	10.58	1:1:1	3 equal	~0.0243
Fc2	60	60	6	100	24	2.51	2.65	10:1:10	250:25:250	~0.0015
Fc3	60	60	6	500	24	2.51	2.65	10:1:10	250:25:250	~0.0015
Fc4	24	24	6	500	24	2.51	2.65	4:1:4	100:25:100	~0.0015
Fc5	15	30	6	100	15	6.41	4.23	10:5:2	50:25:10	~0.0015
Fc6	15	30	6	500	15	6.41	4.23	10:5:2	50:25:10	~0.0015
Fc7	2500	2500	--	1×10 ⁴	24	--	--	1:1	2 equal	--
Fc8	1000	1000	1000	5000	24	--	--	1:1:1	3 equal	~42.144

* for equal average velocity flows; sizes for Hamilton Gastight™ syringes

Table 2.4. Comparison of 100×(critical pressures)/(pressure required for flow) for the devices at physiologic average fluid velocities

		conditions in inlet and outlet channels for devices							
		Fc1	Fc2	Fc3	Fc4	Fc5		Fc6	
						a	b	a	b
1	Q [μl/min]	0.035	0.216	0.216	0.035	0.014	0.027	0.014	0.027
	mm/s	243	140	139	242	620	382	625	385
	in [mm H ₂ O]	214	123	122	212	544	335	549	338
	out [mm H ₂ O]	2.32	4.02	4.05	2.33	0.91	1.48	0.90	1.46
		% $\Delta P_{crit}/(\text{tot } \Delta P \text{ channels})$ [mm H ₂ O]							
3	Q [μl/min]	0.104	0.648	0.648	0.104	0.041	0.081	0.041	0.081
	mm/s	729	420	417	726	1860	1146	1875	1155
	in [mm H ₂ O]	642	369	366	636	1632	1005	1647	1014
	out [mm H ₂ O]	0.77	1.34	1.35	0.78	0.30	0.49	0.30	0.49
		% $\Delta P_{crit}/(\text{tot } \Delta P \text{ channels})$ [mm H ₂ O]							
12	Q [μl/min]	0.415	2.592	2.592	0.415	0.162	0.324	0.162	0.324
	mm/s	2916	1680	1668	2904	7440	4584	7500	4620
	in [mm H ₂ O]	2568	1476	1464	2544	6528	4020	6588	4056
	out [mm H ₂ O]	0.19	0.34	0.34	0.19	0.076	0.12	0.075	0.12
		% $\Delta P_{crit}/(\text{tot } \Delta P \text{ channels})$ [mm H ₂ O]							

The features of each device were (see Figure 2.7):

- Fc1:
- Channels *a*, *b*, and *c* have equal dimensions to simplify flow regulation using three identical syringes.
 - The channel widths *a* and *b* are scaled to the dimensions of the hepatocytes, the larger cell type.
 - The width of the membrane-forming channel (channel *c*) is large so that pressure across the gel will not need to be as carefully regulated as for the other devices.

- Fc1: (con't) – The length of the converged channel region, L , is fairly short. It will be easier to form a stable membrane over a short distance than a long length.
- Fc2: – Channels a and b are have equal dimensions to simplify flow regulation.
- The width of these channels is several times larger than the typical diameter of a hepatocyte; if cells are introduced into the channel, the additional resistance caused by the cells will have a smaller impact on pressure than for a narrower channel.
- The width of channel c is smaller than that of Fc1, and is closer to the thickness of an ideal membrane.
- Fc3: – Channel widths are the same as for Fc2.
- The length of the converged channel region, L , is much larger than for Fc2. The longer interface region may be more useful to co-culture experiments, allowing a greater number of cells to be cultured.
- Fc4: – Similar to Fc3. Channels a and b have equal dimensions to simplify flow regulation.
- The width of channels a and b is scaled to the dimensions of the hepatocytes, the larger cell type.
- The width of channel c is on the order of the thickness of the ideal membrane.
- The length of the converged region, L , is long to provide more space for co-culture interaction.

- Fc5:
- The width and height of channel a are scaled to the diameter of a large capillary. The width of channel b is scaled to the diameter of a hepatocyte.
 - The width of channel c is on the order of the thickness of the ideal membrane.
 - The length of the converged channel region, L , is short, to facilitate stable membrane formation.
- Fc6:
- Similar to Fc3. The length of the converged region, L , is long to provide more space for co-culture interaction.
- Fc7:
- There are only two channels of macro-scale width (2.5mm). Salt solution is flowed through one channel, and peptide solution through the other. The device was designed to determine the time necessary for the salt to diffuse through and gel the peptide stream.
- Fc8:
- Channels a , b , and c have equal dimensions to simplify flow regulation using three identical syringes.
 - The channel widths a , b , and c , and the converged channel region length, L , are all very large. The device can be used to fabricate a macro-scale peptide gel.

The design motivations for the devices are listed in Table 2.5:

Table 2.5. Design motivations for the devices

Fc1	Width of a , b , and c Width of a and b Width of c Length L	Equal dimensions to simplify equal-viscosity flow rate regulation using three identical syringes. Approximately the diameter of a hepatocyte Large to withstand a large ΔP across the membrane Short, to facilitate stable membrane formation
Fc2	Width of a and b Width of c Length L	Equal dimensions to simplify flow regulation; 2 or 3 syringes are identical Greater than the diameter of a hepatocyte to reduce the effect on pressure when cells are introduced Closer to the ideal membrane thickness Short, to facilitate stable membrane formation
Fc3	Width of a and b Length L	See Fc2 Long, to increase the overall co-culture size (cell number, interface region)
Fc4	Width of a and b Width of c Length L	Equal dimensions to simplify flow regulation Approximately the diameter of a hepatocyte Closer to the ideal membrane thickness Long, to increase the overall co-culture size
Fc5	Width of a Width and height of b Width of c Length L	Approximately the diameter of a capillary Approximately the diameter of hepatocyte Closer to the ideal membrane thickness Short, to facilitate stable membrane formation
Fc6	Dimensions of a , b and c Length L	See Fc5 Long, to increase the overall co-culture size
Fc7	Width of a and b	Equal dimensions to simplify flow regulation Macro-scale, to measure diffusion of salt through peptide solution/gel
Fc8	Width of a , b , and c	Equal dimensions to simplify flow regulation using three identical syringes Large, macro-scale dimension, to fabricate a macro-scale peptide gel

2.6 Summary

The device design required the consideration of a wide range of factors. The parameters were chosen based on the physiology of the liver and the mechanical properties of the self-assembling peptide biomaterial. Dimensions were further influenced by the available macro-scale experimental instrumentation. Fluid and solid mechanics analysis techniques were used to

determine minimum membrane thickness values and maximum allowable pressures. The devices were then fabricated and placed in the experimental setup (Chapter 3).

Chapter 3

Fabrication and Experimental Setup

The micron-scale geometry of the bioreactor was fabricated using MEMS technology and standard machining techniques. In this chapter, the fabrication of the glass-silicon device is described and outlined: designing the photomasks, etching the silicon and glass wafers, drilling the glass wafers, and bonding and dicing the silicon-glass devices. Fluidic fittings were designed, machined, and assembled, then attached to the glass-silicon devices. The experimental setup incorporated high-precision syringe pumps, a reflectance microscope capable of fluorescence, and a CCD camera connected to image and video capture hardware and software.

3.1 Silicon-Glass Device Fabrication

3.1.1 Mask Fabrication

The preliminary mask layout for the silicon wafer design was produced on a Pentium PC using SolidWorks99 solid modeling software (SolidWorks Corporation, Concord, MA). The converging channels were designed to merge at angles $\geq 20^\circ$ to minimize distortion to the geometry caused by etching small angles. Detail drawings for the silicon layout were generated in SolidWorks99, and were used to reproduce the geometry in CADENCE layout software (Cadence, Chelmsford, MA) running on a Sun Ultra 1 system (Sun Microsystems, Palo Alto, CA). The design for the glass wafer, consisting of cross hairs for drilling holes and patterns for alignment to the silicon wafer, was also laid out in CADENCE. GDS II-format files were

generated for the silicon and glass wafer photomasks. The silicon wafer layout was patterned on a glass mask (chrome e-beam type mask, Align-Rite Corporation, Middlebury, CT). The glass wafer design was printed on a Mylar transparency using a high-resolution printer by Advance Reproductions (North Andover, MA) (see Appendix A3.1 for mask layouts).

3.1.2 Silicon Wafer Processing

The silicon wafers were standard P-type semiconductor-grade silicon wafers, 100 mm in diameter by 525 microns thick (Virginia Semiconductor, Powhatan, VA). The wafers were cleaned in a 3:1 $\text{H}_2\text{SO}_4:\text{H}_2\text{O}_2$ solution for 20 minutes, then rinsed and spin dried (Figure 3.1a). AZ4620 photoresist (Clariant Corporation, Charlotte, NC) was spin-coated on the surface of the wafer (Figure 3.1b). The mask was aligned to the wafer, and the resist was exposed using a Karl-Suss MA6 contact mask aligner (SUSS MicroTec, Munich, Germany) (Figure 3.1c). The photoresist was developed with a 4:1 $\text{H}_2\text{O}:\text{AZ400K}$ developer solution (Clariant Corporation, Charlotte, NC) for 3 minutes 30 seconds. The exposed resist was removed, and the wafer was cleaned and dried (Figure 3.1d). The mesa etch process, performed in a STS Reactive Ion Etch (RIE) machine (Surface Technology Systems, Newport, England) at 200 mTorr and 75 watts, removed 24 ± 1 microns of silicon from the wafer (Figure 3.1e). Finally, the resist was removed by rinsing the wafer with acetone, methanol, and dionized water (Figure 3.1f) [5,19].

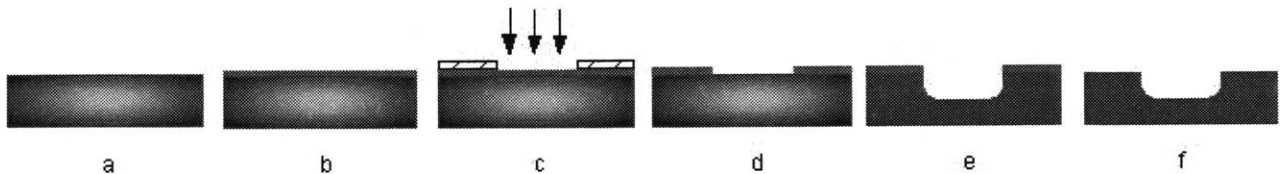


Figure 3.1. Diagram showing the silicon photolithography process

3.1.3 Glass Wafer Processing

The glass wafers were Schott Borofloat[®] wafers made of Pyrex[®] (composition identical to Corning 7740, Corning Glass Works, Corning, NY), 100 mm in diameter by 780 microns thick, polished to a near-optical finish (Schott Corporation, Technical Glass Division, Yonkers, NY). The wafers were cleaned in a 3:1 H₂SO₄:H₂O₂ solution for 20 minutes, then rinsed and spin dried (Figure 3.2a). The wafers were spin coated with Shipley 1822 photoresist (Figure 3.2b) (Shipley Company, Marlborough, MA), aligned to the mask, and exposed by standard photolithography techniques (Figure 3.2c). The photoresist was developed in Shipley MF319 developer for 30 seconds, then rinsed and dried (Figure 3.2d). Recesses were etched to a target depth of $1700 \text{ \AA} \pm 200 \text{ \AA}$ in an HF buffered oxide etch (BOE) for ~7 minutes (Figure 3.2e). The wafer was rinsed and dried, then sputter coated with titanium (400 \AA), then platinum (700 \AA), gold (850 \AA), and platinum (500 \AA), in a Mill Lane sputter machine (Mill Lane Engineering, Lowell, MA) (Figure 3.2f). SVC-12 solution (Silicon Valley Microelectronics, San Jose, CA) was used for the metal lift-off process. The wafer was cleaned, dried, and inspected (target metal height $750 \text{ \AA} \pm 250 \text{ \AA}$) (Figure 3.2g).

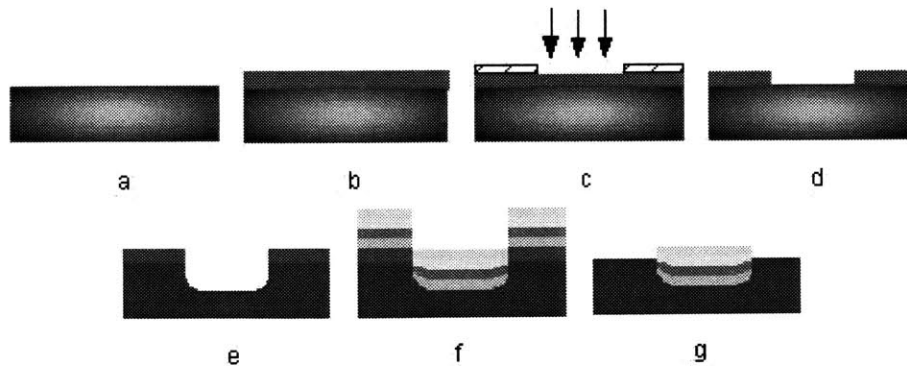


Figure 3.2. Diagram showing the metal-on-glass deposition process

The glass wafer was then fixed to a platen with wax and holes were drilled on a 3-axis CNC Vertical Machining Center (Mitsui Seiki Corporation, Tokyo, Japan). Areas around the holes on

the unpatterned side of the glass wafer (the outer surface of the final device) were bead-blasted with 50 micron aluminum oxide particles to roughen the surface for improved epoxy adhesion to the fluidic fittings (described in Section 3.2.2).

3.1.4 Glass-Silicon Bonding and Dicing

The silicon wafers were cleaned in a 1:1 $\text{H}_2\text{SO}_4\text{:H}_2\text{O}_2$ solution for 10 minutes, rinsed in deionized water, and dried under a stream of N_2 gas. The Pyrex wafers were cleaned in a 1:1 $\text{H}_2\text{SO}_4\text{:H}_2\text{O}_2$ solution for 30 seconds, then rinsed in deionized water, sprayed with isopropyl alcohol, rinsed in deionized water, and dried under a stream of N_2 gas. The etched side of the silicon wafer was positioned against the patterned side of the Pyrex wafer using the alignment features, and the wafers were anodically bonded at 335°C for 1 hour at a bias of 970 volts across the wafers. The holes in the Pyrex wafer were sealed with tape and the devices were cut from the wafer with a Disco DAD321 Automatic Dicing Saw (Disco Corporation, Tokyo, Japan).

3.2 Fluidic Fittings

3.2.1 Design of the Fittings

Fittings for delivering fluid to and from the bonded silicon-glass device were machined from stainless steel rod and tubing. The fittings were designed to have a low profile to avoid interference with the microscope objective (see Section 3.4). Two types of fittings were made to attach to either large-bore or small-bore tubing. The large-bore fittings were attached to holes at the ends of the inlet and outlet channels for infusing water or allowing the outflow of refuse and waste fluids. The small-bore fittings were attached to holes that sit along each of the three inlet channels for introducing the reactive fluids (peptide solution and saline) (Figure 3.3).

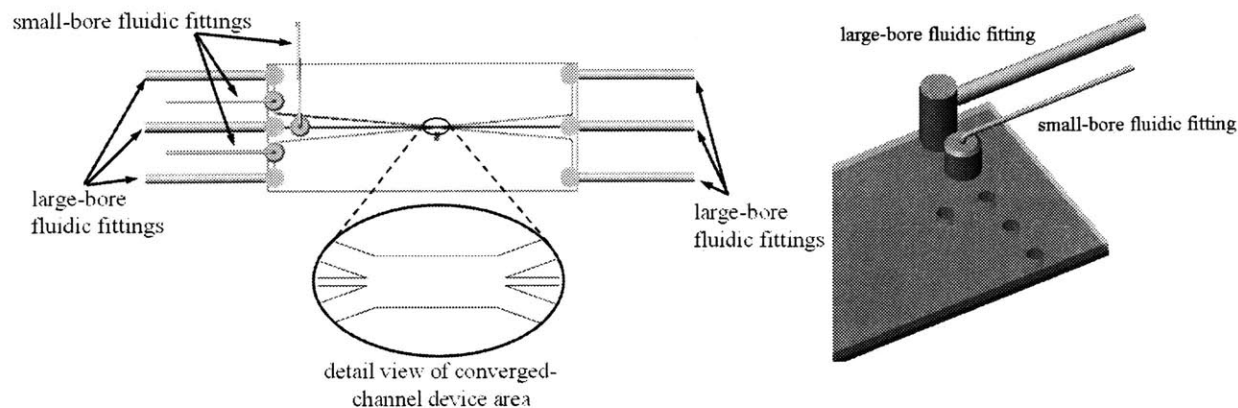


Figure 3.3. A top view of the device, looking through the glass. The detail image shows a magnified view of the converged-channel area (*left*). An isometric drawing of a large-bore and small-bore fluidic fitting (*right*).

The small inner-diameter of the delivery tubing and the fluidic fitting itself minimizes the amount of dilution that can occur before the fluids enter the silicon-glass device (Figure 3.4).

(see Appendix A3.2 for machine drawings and assembly procedure)

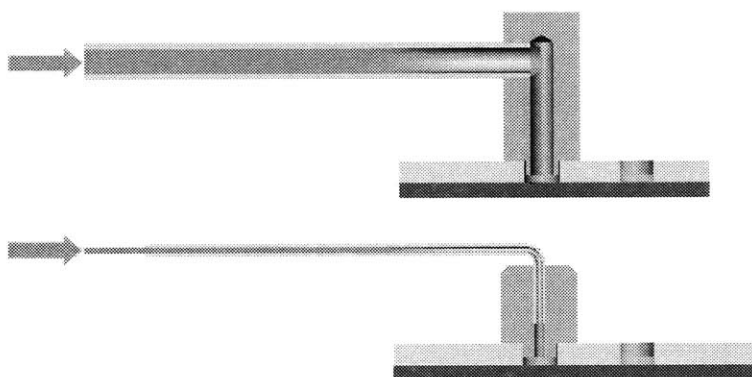


Figure 3.4. A smaller volume of solution becomes diluted in the small-bore tubing (*bottom*) than in the large-bore tubing (*top*).

3.2.2 Assembly Procedure

After dicing, the bonded glass-silicon devices were inspected under a microscope to make sure that the channels were clear of debris. In the case that there was debris in the channels, it was often possible to attach fluidic fittings to either the outlet or inlet holes, depending on the location of the blockage, then flush the channels with water to clear them (an

ultrasonic cleaner was used sparingly to dislodge blockage; extended use broke the epoxy-glass bond between the fittings and the glass wafer).

When attaching the metal fluidic fittings to the glass surface of the device, it was important to ensure that no epoxy leaked into the silicon channels. An adhesive gasket was used to hold the fluidic fitting in place and maintain a seal between the glass and the fitting while the epoxy was curing (see Appendix A3.3 for fabrication of the adhesive gasket).

Once the fluidic fitting was held in position on the silicon-glass device by the adhesive gasket, a small amount of MSD 505-3 epoxy (manufactured under contract to the Navy by Bacon Industries, Watertown, MA) was applied around the fitting-glass interface (Figure 3.5). The epoxy was allowed to harden at room temperature for 12 hours, then cured in a 60°C oven for 24 hours. The procedure tended to minimize reflow of epoxy into the device channels.

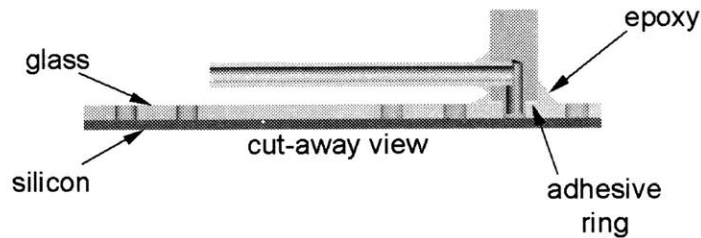


Figure 3.5. A cut-away view of an assembled large-bore fluidic fitting, showing placement of the adhesive ring and the application of the epoxy

3.3 Device Validation

The device was tested to make sure that the channels were open and obstruction-free. Water was pumped through each of the fluidic fittings with a syringe attached to elastic Tygon™ tubing (Saint-Gobain Performance Plastics, Wayne, NJ). For the large-bore fluidic fittings, S-54-HL Tygon™ tubing (O.D. Ø0.090 in., I.D. Ø0.050 in.) was attached to the syringe with a 21 gage disposable needle; the other end was slipped snugly over the metal fluidic fitting. For the small-bore fittings, R-3603 Tygon™ tubing (O.D. Ø0.0795 in., I.D. Ø0.0075) was attached to the

syringe with a 33 gage needle, and the other end was slipped over the end of the metal fluidic fitting.

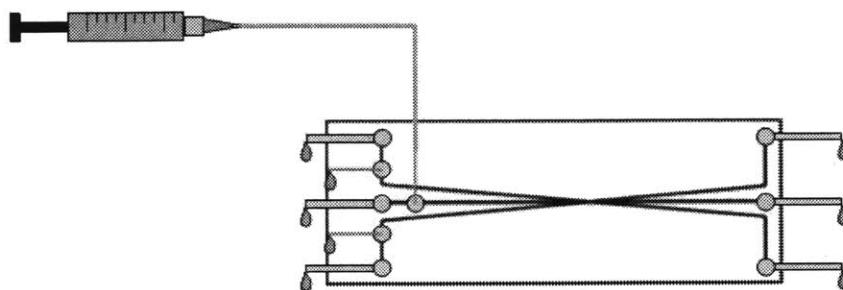


Figure 3.6. Testing the device to verify that the channels are unoccluded

Deionized 0.22 μm filtered water was then infused into a fluidic fitting. If droplets were observed emerging from the other fluidic fittings, the length of channel was clear (Figure 3.6). All fittings were checked to ensure that the channels were open and unoccluded.

3.4 Experimental Setup

While the specific fluid paths and connections varied throughout the experiments, most of the experimental hardware remained constant. One or two PHD2000 syringe pumps (Harvard Apparatus, Holliston, MA) were used to control flows in the system. These pumps can infuse or withdraw fluid at flow rates ranging from 0.0001 $\mu\text{l/hr}$ to 220.82 ml/min (depending on the inside diameter of the syringe), and can exert up to 50 pounds of force at low speeds, 30 pounds of force at high speeds. One syringe pump was a standard 2-syringe infuse-withdraw pump. The other was a modified push-pull pump, customized to simultaneously infuse 4 syringes and withdraw 4 syringes (Figure 3.7) (see Appendix A3.4 for details of the pump modification).

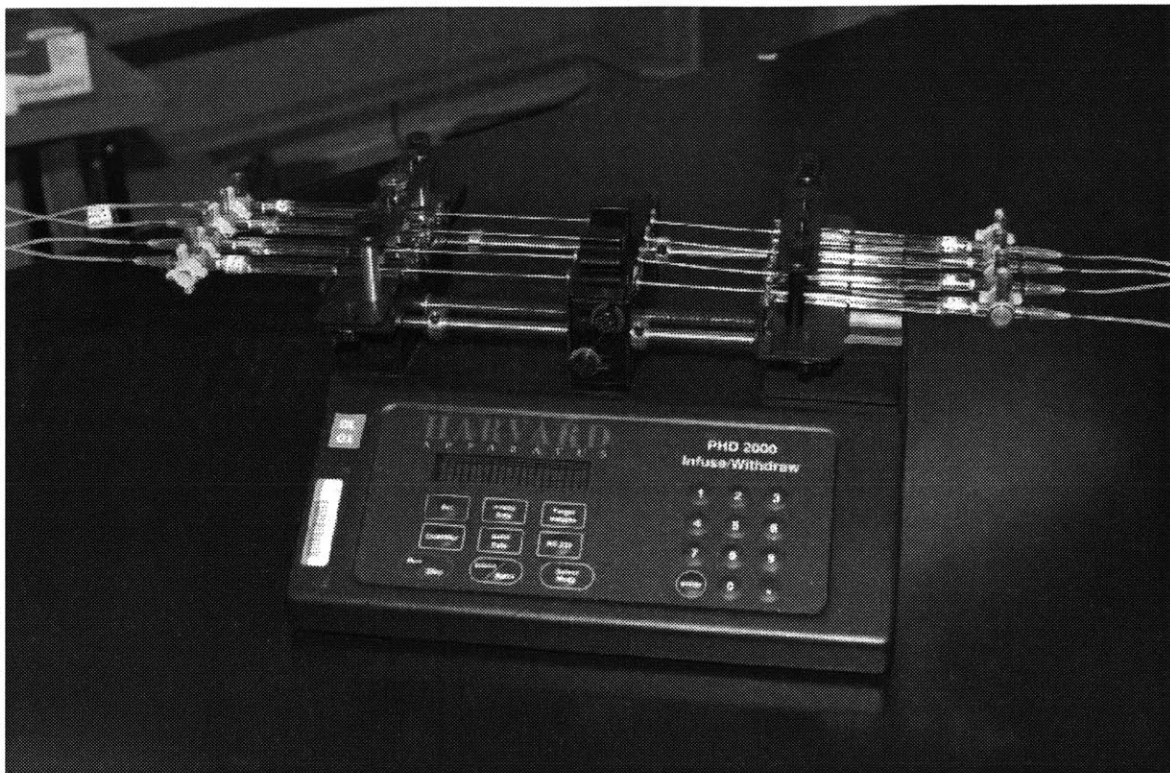


Figure 3.7. The modified Harvard PHD2000 syringe pump

In early experiments, Tygon[™] tubing was used to make the fluidic connections. For the large-bore fluidic fittings, S-54-HL Tygon[™] tubing, O.D. Ø0.090 in., I.D. Ø0.050 in., was used; for the small-bore fluidic fittings, R-3603 Tygon[™] tubing, O.D. Ø0.0795 in., I.D. Ø0.0075 in. For later experiments, small-bore Teflon[™] ETFE tubing, O.D. Ø0.063 in., I.D. Ø0.012 in., was used.

Plastic Luer-connector stopcocks, barb fittings, and female-female fittings were used. To connect the tubing, disposable needles with plastic Luer fittings (16, 21, and 33 gage, Becton, Dickinson, and Company, Franklin Lakes, NJ) were dulled and deburred with a grinder. Tygon[™] tubing was stretched over the needles to make a seal. The Teflon[™] tubing was attached by boring the tubing ends to a depth of ~¼ inch, cleaning the debris, and pressing them onto the needle ends.

A custom-built reflectance microscope, based on an Olympus SZX12 (Olympus America, Melville, NY, configured and assembled by Kramer Scientific, Valley Cottage, NY), was used to observe the fluidic device. Fluorescence capability was provided by an arc lamp (Ludlum Electronic Products Ltd., Hawthorne, NY) and a UV filter. An integrated CCD camera (Optronics, Goleta, CA) was used for data collection. The camera sent both an RGB signal and an S-video signal to a DC30 Pro video capture card (Pinnacle Systems, Mountain View, CA) installed in a Gateway E-5200 PC (Gateway, Inc., San Diego, CA). Still images were captured from the RGB signal and analyzed using Image Pro Plus image acquisition and analysis software (Media Cybernetics, Silver Spring, MD). Video from the S-video signal was captured using microVideo Capture software (Pinnacle Systems). AVI video files were edited using Adobe Premiere 5.0 (Adobe Systems Inc., San Jose, CA), and were compressed and converted to MPEG files using the Honestech MPEG Encoder software (Honestech Technology, Marlton, NJ). To adjust the height of the microscope, the entire assembly was mounted on a single vertical stainless-steel post measuring 1.5 inches in diameter. This configuration made the microscope extremely susceptible to vibration. To reduce vibration and improve the video image, the microscope, syringe pumps, and fluidic assembly were placed on an air table (Figure 3.8).

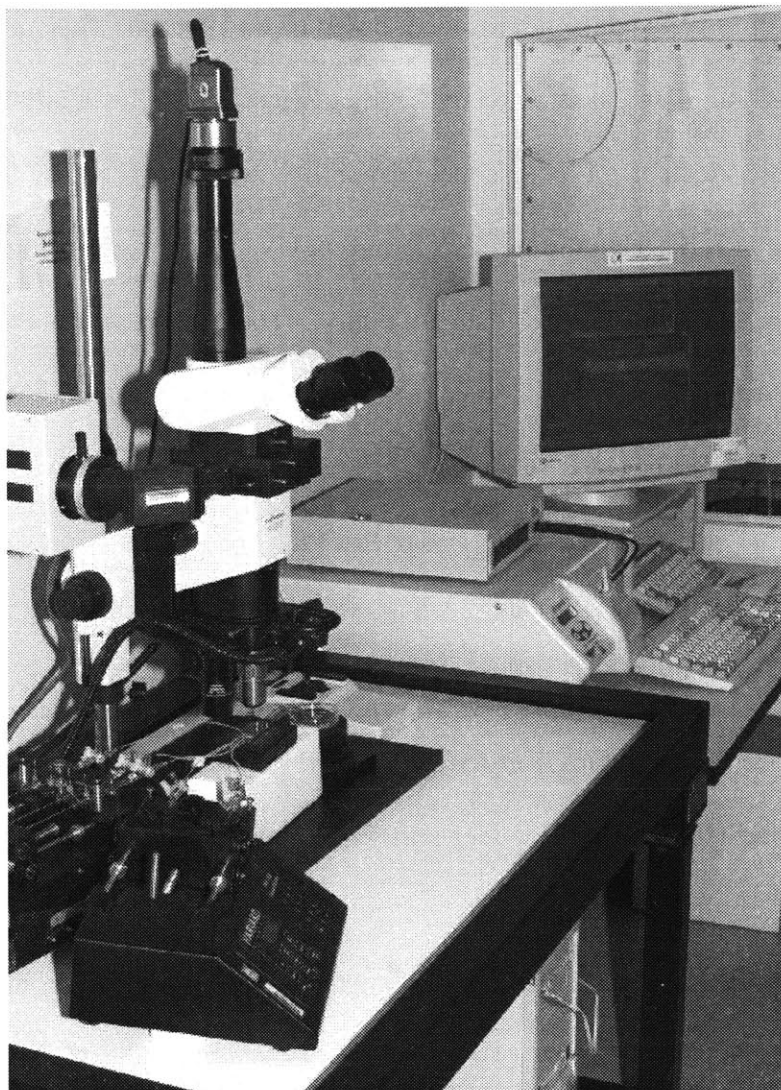


Figure 3.8. The experimental setup

3.5 Summary

The micron-scale fluidic devices were fabricated using current standard microlithography technology. The silicon-glass devices were interfaced with macro-scale devices to allow observation and control at the micron-scale. The setup enabled the observation of features as small as 1 micron and control of flow rates as low as $0.0001 \mu\text{l}/\text{hour}$. Digital video equipment was used to acquire still and moving images of flow and gel-forming processes to aid in device characterization and process refinement.

Chapter 4

Computational Analysis

Flow and transport within the capillary-parenchymal element (CPE) bioreactor during membrane formation was analyzed and optimized with the objective of maintaining three distinct flow streams, minimizing mixing, and controlling the final dimensions of the gelled membrane. For a device with given dimensions, the controllable parameters are the viscosity and flow rates of the fluids. The flow field and mass transfer was analytically and numerically simulated for the device to determine the optimal values of these parameters that produce the desired membrane properties. The fluid dynamics solutions for flows of different fluids in the device (water, peptide solution, and saline solution, each fluid possessing different properties) were non-trivial. Modeling led to better understanding of flow and mass transfer in the device during gel formation and facilitated the design of experimental protocols.

4.1 Flow Parameters and Constraints

The controllable parameters in the experimental set-up included the flow rates of the fluids and the fluid viscosities, which could be increased by adding Dextran or some another thickening reagent. From the models, the following can be determined:

- Inlet flow rates and fluid viscosities that will result in laminar flow in the axial direction of the device with no recirculation or vortex formation (Figure 4.1)

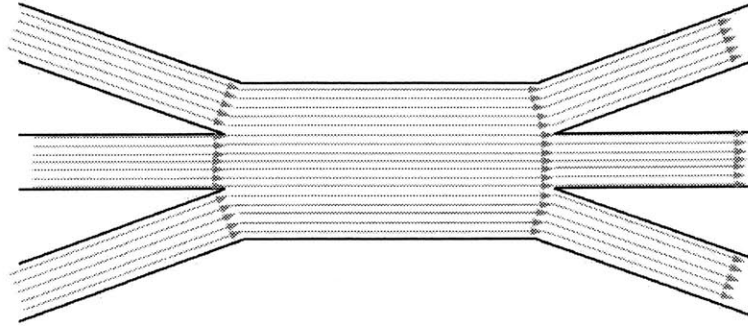


Figure 4.1. Flow rates are chosen that provide laminar flow conditions.

- Inlet flow rates and fluid viscosities that will result in constant peptide solution/gel width along the entire length of the converged-channel region (Figure 4.2)

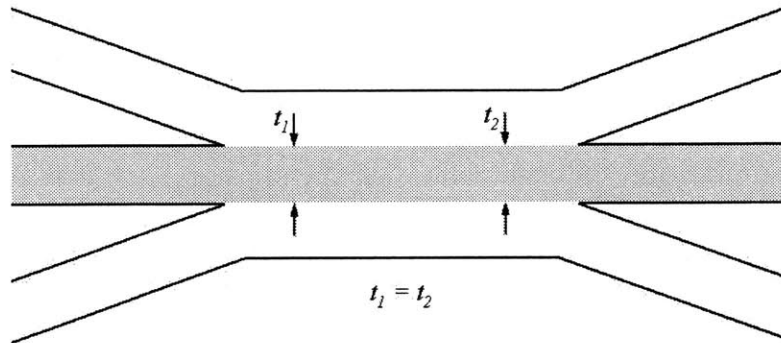


Figure 4.2. The membrane is to be of uniform thickness along the entire converged-channel area.

- The initial gelling patterns of the peptide – Once gelation begins, the model becomes more complex owing to the growing region of solid gel. Here, only the initial stages are considered, prior to gel formation.

The fully developed flow field was solved analytically in the converged-channel device area of the fabricated geometry to determine the necessary values for the inlet flow rates and fluid viscosities. From this solution, the values that affect the desired peptide solution stream dimensions were determined (Figure 4.3, second from top). A fully three-dimensional finite element model of the converged-channel device area was set up and numerically solved for the flow field with the optimized flow rates and viscosity values (Figure 4.3, second from bottom).

The finite element model was then solved for mass transfer of the saline to shed light on the gelation process and time scales (Figure 4.3, bottom).

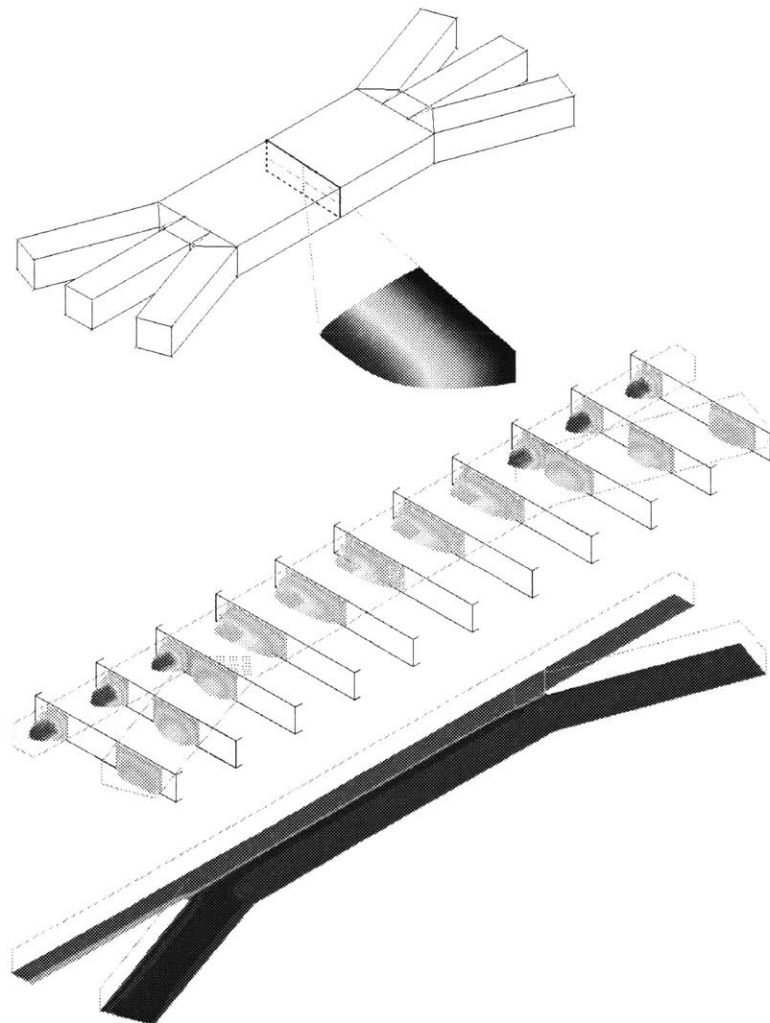


Figure 4.3. Modeled geometry (*top*), $\frac{1}{4}$ analytic solution of the velocity field (*second from top*), $\frac{1}{4}$ model of the numerical flow solution (*second from bottom*), $\frac{1}{4}$ model of the mass transfer solution for concentration (*bottom*)

4.2 Analytic Solution to the Three-Dimensional Flow

4.2.1 Derivation of the Analytic Solution

A top view of the device is shown in Figure 4.4. Q_s is the flow rate in each of the side channels. This fluid, either water or saline, flows on either side of the incoming peptide solution (flow rate Q_p). Q_{os} is the outlet flow rate through the side channels, and Q_{oc} is the outlet flow

rate through the center channel. Depending on the flow conditions in the device, Q_{Os} and Q_{Oc} may contain purely saline and purely peptide solution, or combinations of these (as well as gelled peptide particles).

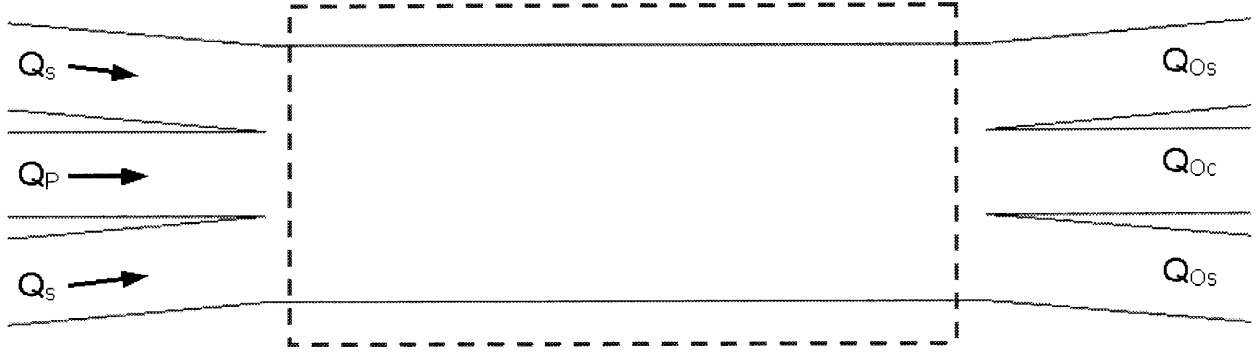


Figure 4.4. A top view of the converged-channel area; the red box shows the fully-developed region for low Reynolds number flow

The Reynolds number (Re) for the system using the geometry from device Fc1 (see Table 2.3) and an average flow velocity from typical experimental flow rate values is defined as

$$Re = \frac{LV}{\nu} = \text{inertial force} / \text{viscous force}. \quad (4.1)$$

The length scale L is the hydraulic diameter of the channels, D_h , which is calculated by:

$$D_h = \frac{4 \cdot (\text{cross-sectional area})}{(\text{wetted perimeter})} = 36 \mu\text{m}. \quad (4.2)$$

The average velocity in the center region of the device, V , is calculated from typical experimental flow rates:

$$Q_s = 0.0863 \mu\text{l/min}$$

$$Q_p = 0.133 \mu\text{l/min}$$

A total flow rate of $0.3056 \mu\text{l/min} = 5.0933 \times 10^{-12} \text{ m}^3/\text{s}$ results in an average fluid velocity

$$V = Q_{\text{tot}} / A_{\text{x-sectional area}} = \frac{5.0933 \times 10^{-12} \text{ m}^3/\text{s}}{1.728 \times 10^{-9} \text{ m}^2} = 2.948 \times 10^{-3} \text{ m/s}.$$

The kinematic viscosities of the peptide and saline are calculated from their absolute viscosities and densities:

$$\mu_P = 0.006 \text{ Ns/m}^2 \quad (\text{See appendix A4.2 for measurement})$$

$$\rho_P = 1022.3 \text{ kg/m}^3 \quad (\text{See appendix A4.1 for measurement})$$

$$\nu_P = 5.87 \times 10^{-6} \text{ m}^2/\text{s}$$

$$\nu_{\text{saline}} \approx \nu_{\text{water}} = 0.995 \times 10^{-6} \text{ m}^2/\text{s}$$

The value for kinematic viscosity used to calculate an effective Reynolds number is weighted between peptide and saline according to the cross-sectional area of each different fluid (see Figure 4.6),

$$\nu_{\text{mixture}} = 2.62 \times 10^{-6} \text{ m}^2/\text{s}.$$

Thus,

$$Re = \frac{(3.6 \times 10^{-5} \text{ m}) \left(2.948 \times 10^{-3} \frac{\text{m}}{\text{s}} \right)}{2.62 \times 10^{-6} \frac{\text{m}^2}{\text{s}}} = 0.0405. \quad (4.3)$$

The Reynolds number for this system is very low and flow is therefore viscous-dominated and laminar. Consequently, soon after the convergence of the three streams, the flow becomes unidirectional and fully-developed.

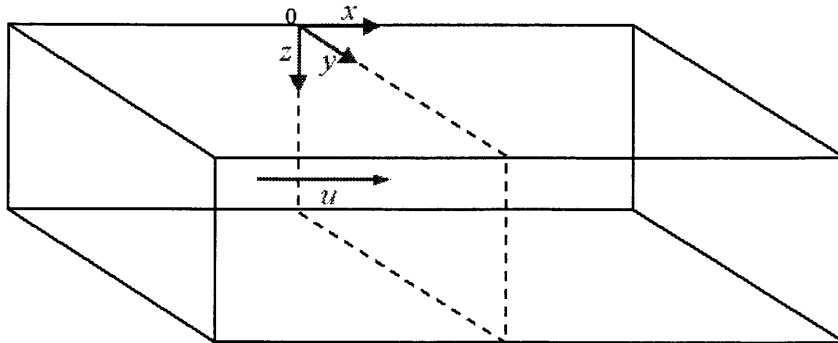


Figure 4.5. An isometric view of the boxed-region in Figure 4.4

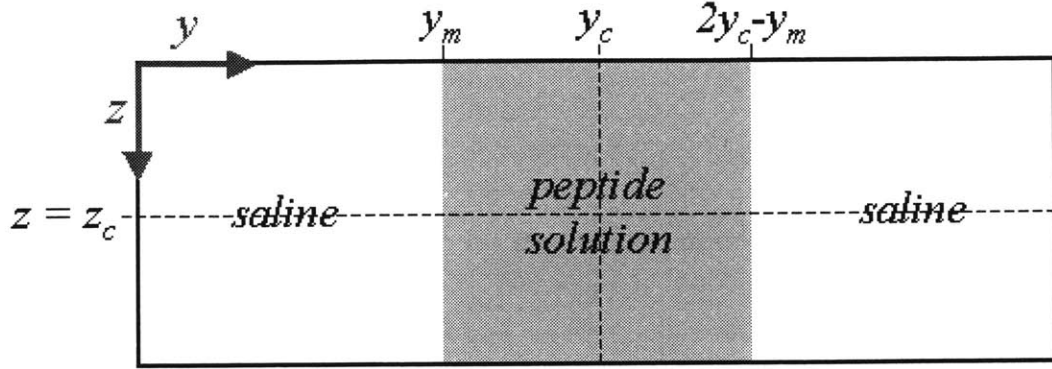


Figure 4.6. A cross-section view of the converged-channel region corresponding to the area denoted by the dashed line in Figure 4.5

At any cross-section in the converged-channel region (Figure 4.5, Figure 4.6), the geometry is symmetric about y_c and z_c , so it is sufficient to consider one quadrant of the flow domain (Figure 4.7). y_m and $2y_c - y_m$ indicate the y -position of the interface between the saline and peptide flows. In Figures 4.6 and 4.7, the grayed area denotes the part of the cross-section that is filled with peptide. The width of this area depends on the flow rate and viscosity ratios of saline to peptide ($Q_S:Q_P$ and $\mu_S:\mu_P$).

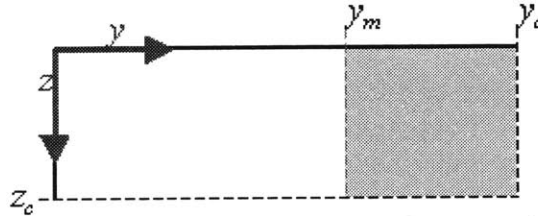


Figure 4.7. A single quadrant of the cross-section shown in Figure 4.6

Flow is governed by the Navier-Stokes equation for flow in the x -direction:

$$\frac{\partial u}{\partial t} + u \frac{\partial u}{\partial x} + v \frac{\partial u}{\partial y} + w \frac{\partial u}{\partial z} = -\frac{1}{\rho} \frac{\partial p}{\partial x} + \frac{\mu}{\rho} \left(\frac{\partial^2 u}{\partial x^2} + \frac{\partial^2 u}{\partial y^2} + \frac{\partial^2 u}{\partial z^2} \right) \quad (4.4)$$

where u is flow in the x -direction, v is flow in the y -direction, and w is flow in the z -direction

The flow is assumed to be fully-developed at steady state, solely in the x-direction, with no slip at the walls and a zero velocity gradient at the centerlines. The series solution to this problem is found using the Finite Fourier Transform method [9] (see Appendix A4.3).

4.2.2 Application and Execution of the Analytic Model

The series solution for the fluid velocity u was computed and projected onto a discrete matrix for one quadrant using MATLAB (The Mathworks, Natick, MA) (see Appendix A4.4.1 for the MATLAB code,). The velocity matrix was then mirrored onto the other quadrants and plotted to visualize the fluid velocity field. The user-specified values are: $\frac{\partial p}{\partial x}$, the pressure gradient parallel to the channel axis; y_m , the y-position of the interface between the saline/water and peptide solution; μ_{saline} , the viscosity of the saline solution; and μ_{peptide} , the viscosity of the peptide solution. The code computes the velocity profile, which is integrated to give side and center flow rates. The mesh size and n in the series expansion were optimized (see Appendix A4.4). The ratio $Q_S:Q_P$ is determined by y_m and $\mu_{\text{peptide}}:\mu_{\text{saline}}$ (Figure 4.8, Figure 4.9). The magnitudes of Q_S and Q_P are linearly related to $\frac{\partial p}{\partial x}$ while the ratio $Q_S:Q_P$ is independent of $\frac{\partial p}{\partial x}$ (Figure 4.10).

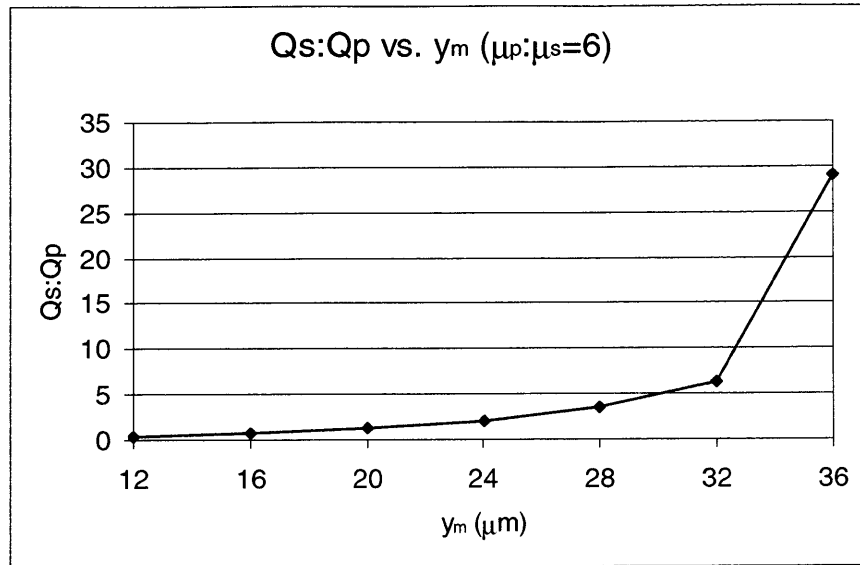


Figure 4.8. A plot of the flow ratio $Q_s:Q_p$ as a function of y_m

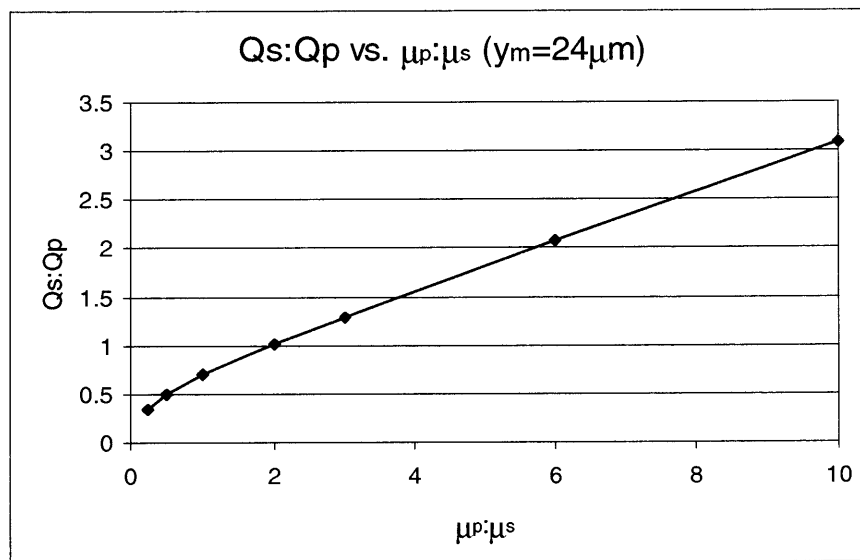


Figure 4.9. A plot of the flow ratio $Q_s:Q_p$ as a function of $\mu_{\text{peptide}}:\mu_{\text{saline}}$

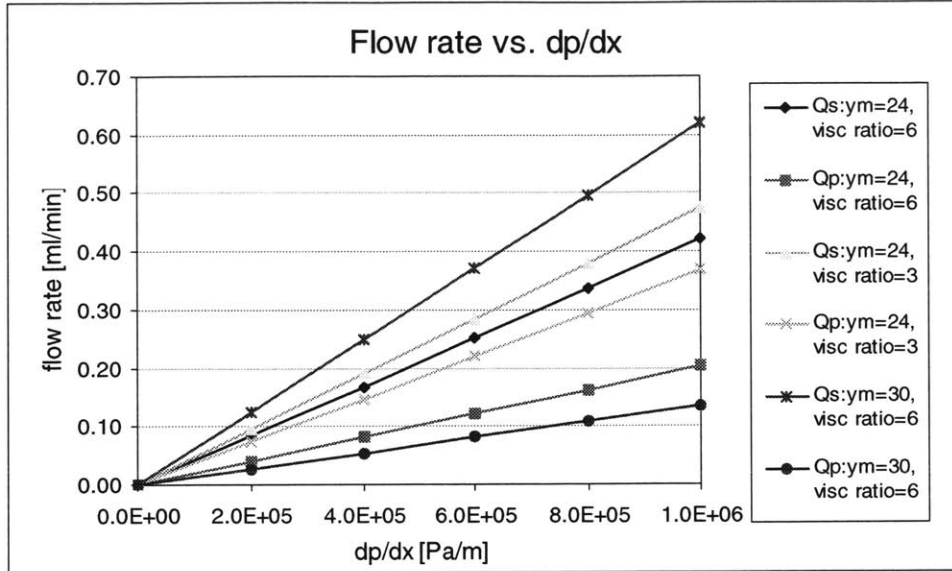


Figure 4.10. A plot of the absolute flow rates (Q_s and Q_p) as linear functions of the axial pressure gradient over the converged-channel region (dp/dx)

4.2.3 Results from the Analytic Model

A gel with the width of the center channel sets y_m . The $\frac{\partial p}{\partial x}$ value is then adjusted to produce flow rates that will result in low Reynolds number laminar flow. When viscosity values typical of those for the saline and peptide solutions ($\mu_{\text{saline}} \approx \mu_{\text{water}} = 0.001 \text{ Pa}\cdot\text{s}$, $\mu_{\text{peptide}} = 0.0060 \text{ Pa}\cdot\text{s}$) and the geometry for device Fc1 are used, the flow profile has the appearance of that shown in Figure 4.11.

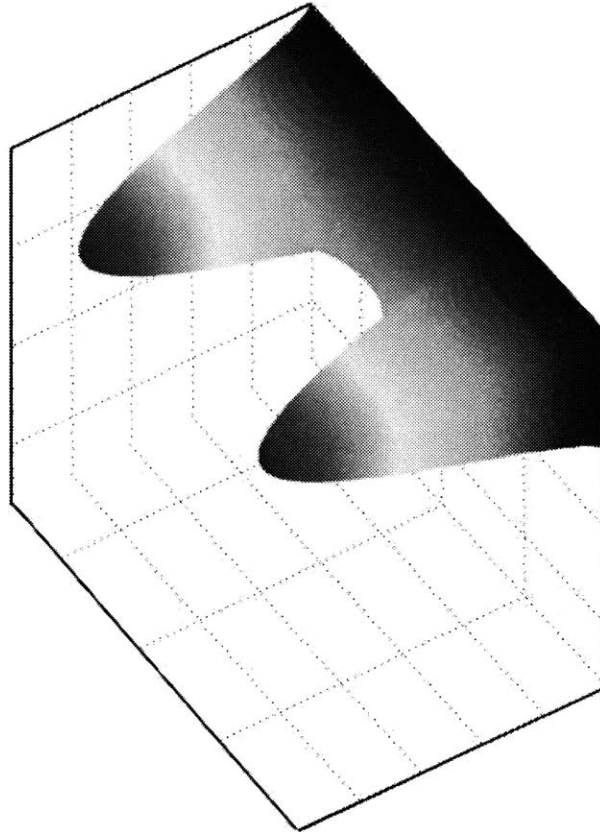


Figure 4.11. The flow profile for $\mu_{\text{saline}} = 0.001 \text{ Pa}\cdot\text{s}$, $\mu_{\text{peptide}} = 0.0060 \text{ Pa}\cdot\text{s}$, $y_m = 24 \text{ }\mu\text{m}$

The slope of the velocity profile is discontinuous at the interface between the two fluids due to the difference in viscosities and the fact that shear stress is continuous across the fluid interface. To attain the specified y_m at these viscosity values, the saline flow rate must be 2.1388 times that of the peptide solution for the viscosity ratio of $\mu_{\text{peptide}}:\mu_{\text{saline}} = 6:1$.

The problem can be further defined by placing conditions on the actual flow values themselves. Syringe pumps drive the flow rates; pressure at the convergence of the three channels will be equal, but pressures at the syringes are unspecified, determined by the inlet flow rates and the resistance of the inlet channels and tubing. To minimize the complexity of the system, all the outlets are to be maintained at atmospheric or some other equal pressure environment. To maintain constant y_m over the distance of the saline-peptide interface, the outlet flow rates for the three streams must be the same as their respective inlet flow rates; this causes

the composition of the outlet flows to be purely saline or peptide solution. The resistances of the center and side outlet channels must be controlled to achieve this. If the fabricated geometry of the device is considered fixed, the only variables that can be adjusted to meet this requirement are the fluid viscosities. In the analytic model, the viscosity of the saline solution was varied to obtain a $Q_{\text{saline}}:Q_{\text{peptide}}$ flow rate ratio, then the outlet pressure drops were calculated, based on the center and side outlet channel resistances, and compared. The viscosity values were adjusted and this step repeated until the side and center pressure drops were equal. The values which satisfied these conditions ($\mu_{\text{saline}} = 0.00711 \text{ Pa}\cdot\text{s}$, $Q_{\text{saline}} = 0.087961 \text{ }\mu\text{l}/\text{min}$; $\mu_{\text{peptide}} = 0.0060 \text{ Pa}\cdot\text{s}$, $Q_{\text{peptide}} = 0.13512 \text{ }\mu\text{l}/\text{min}$) were the optimized viscosity and flow rate values for the geometry (see Figure 4.12 for the plot of the flow profile).

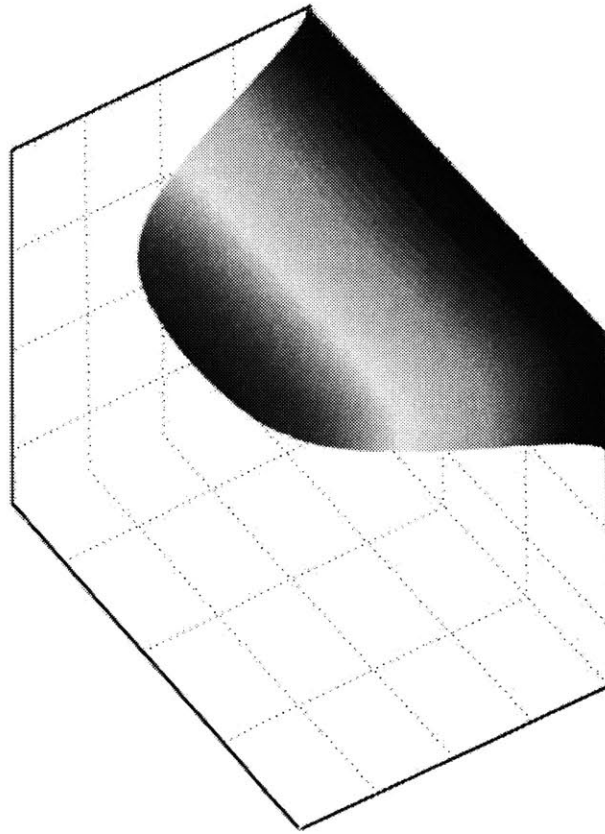


Figure 4.12. The flow profile for $\mu_{\text{saline}} = 0.00711 \text{ Pa}\cdot\text{s}$, $\mu_{\text{peptide}} = 0.0060 \text{ Pa}\cdot\text{s}$, $y_m = 24 \text{ }\mu\text{m}$

4.3 The Numerical Model: Fluid Flow and Mass Transfer

4.3.1 Setting up the Numerical Model

The analytic model can represent the velocity profile in the fully-developed flow region within the converged-channel device area, but it does not model flow outside of this limited domain. To examine flow throughout the device and to model the mass transfer in the system, a numerical model was employed. The analytic model, while limited, is still important, as it provides the flow rate and viscosity values to be used in the numerical model.

Before modeling the mass transfer problem, the Peclet number (Pe , the ratio of the effect of convection to that of diffusion) for the fluids can be studied to assess the need for a mass transfer model. For the peptide solution,

$$Pe_{peptide} = \frac{VL}{D_{peptide}} = \frac{(3.0 \times 10^{-3} \text{ m/s})(3.6 \times 10^{-5} \text{ m})}{1.58 \times 10^{-12} \text{ m}^2/\text{s}} = 68,354 \quad (4.5)$$

where $L = D_h = 36 \text{ } \mu\text{m} = 3.6 \times 10^{-5} \text{ m}$; average fluid velocity $V = 3.0 \times 10^{-3} \text{ m/s}$;

$D_{peptide} \approx 1.58 \times 10^{-8} \text{ cm}^2/\text{s} = 1.58 \times 10^{-12} \text{ m}^2/\text{s}$ (for calculation, see Appendix A4.5).

A Peclet number of 68,354 indicates extreme convection dominance for the peptide solution. Thus, in the experiments the peptide solution is present only in the regions determined by the streamlines with virtually no diffusion effects. For saline,

$$Pe_{saline} = \frac{VL}{D_{saline}} = \frac{(3.0 \times 10^{-3} \text{ m/s})(3.6 \times 10^{-5} \text{ m})}{1.483 \times 10^{-9} \text{ m}^2/\text{s}} = 72.8 \quad (4.6)$$

A Peclet number of 72.8 also shows strong convection dominance, but Pe_{saline} is orders of magnitude lower than $Pe_{peptide}$. The extent of saline diffusion into the peptide stream will have an effect on the initial thickness of the gel membrane, so it is important to model the mass transfer of the salt, using the experimental parameters to control the initial gelling conditions.

Again, flow in device Fc1 was modeled. Rather than modeling the entire device, focus was placed on the converged-channel device area and lengths of the adjoining inlet and outlet channels. The channels were truncated at a sufficient distance from the membrane-forming region to ensure fully-developed flow at the channel convergence. To reduce computing time, the model was quartered along the two planes of symmetry (Figure 4.13).

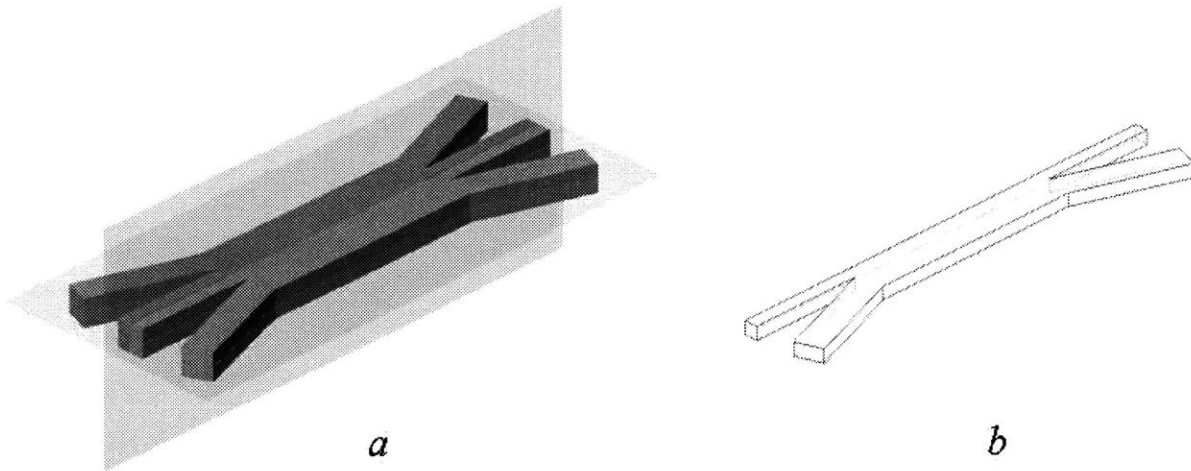


Figure 4.13. (a) The converged-channel device area geometry for Fc1;
(b) $\frac{1}{4}$ model of the geometry, cut along two planes of symmetry

Inlet flow rates and fluid viscosities determined from the analytic model were used in the numerical model. The initial configuration of the model was set up with the peptide and saline solutions spanning the device area with widths equal to those of their respective inlet channels. Element groups, material types, and mass transfer properties were defined for saline and the peptide solution to represent the density and viscosity of these materials. The flow was assumed to be incompressible and laminar. The velocity loads were applied at the three inlets and the two side outlets; the flow rate out of the center outlet was unspecified to not over-define the problem. The model was normalized and the material properties (density, viscosity, and diffusivity) were non-dimensionalized to eliminate potential computational problems that can arise from very small and very large values (see Appendix A4.6).

The finite element model was solved using ADINA 7.4 finite element modeling software (ADINA R&D, Watertown, MA). The finite element model contained 110,400 linear tetrahedral elements with 22,221 nodes. The mesh was generated using the Delauney algorithm with 4 nodes per element. The mesh was refined near the interfaces between the two fluids to accurately model the behavior of the two fluids at their interface.

4.3.2 Numerical Results

The numerical model was set up for the Fc1 geometry and flow parameters determined by the analytic solution. Normalized vector plots of the flow field at the center z-plane and y-plane of the device are shown in Figure 4.14 and Figure 4.15.

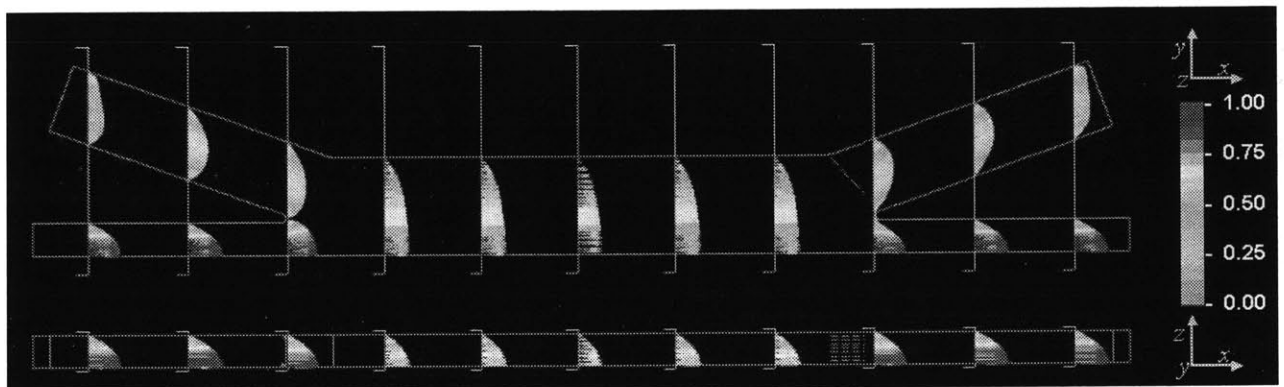


Figure 4.14. A vector plot of the numerical results for the normalized velocity field; flow is left to right

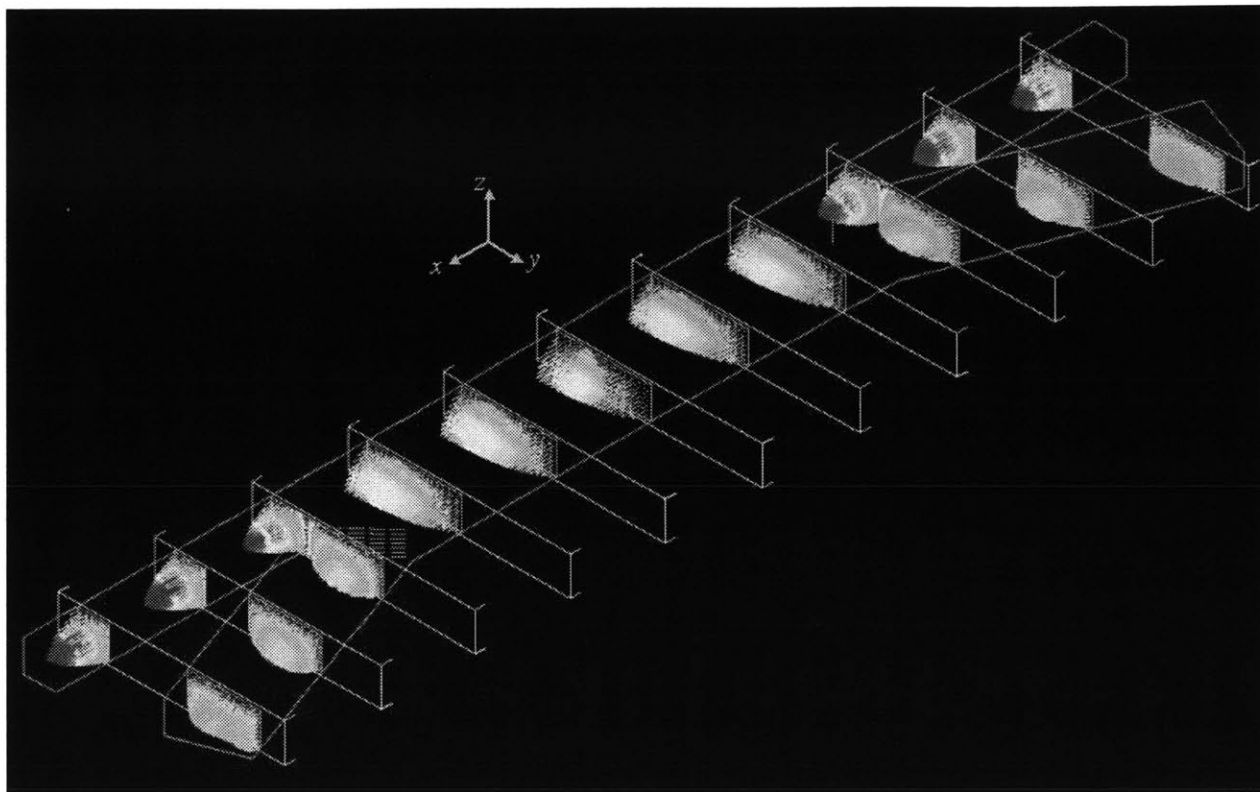


Figure 4.15. An isometric vector plot of the numerical results for the normalized velocity field; flow is upper right to lower left

Flow in the device is parallel to the channel axis with no recirculation in the corners. The high Peclet number for the peptide flow indicates that the peptide solution will be constrained to the streamlines that flow from the center inlet channel, across the device area, to the center outlet channel. To confirm this prediction, the concentration of peptide solution in the device was modeled. The plot of normalized peptide concentration at the center z -plane is shown in Figure 4.16. The peptide solution remains confined to the center of the device with the stream width determined by the viscosities and in-flow rates. The sharp, almost step-function-like concentration gradient between 1.00 and ~ 0.00 is in agreement with the high Peclet number; progressive refinement of the mesh along this interface sharpened the gradient further.

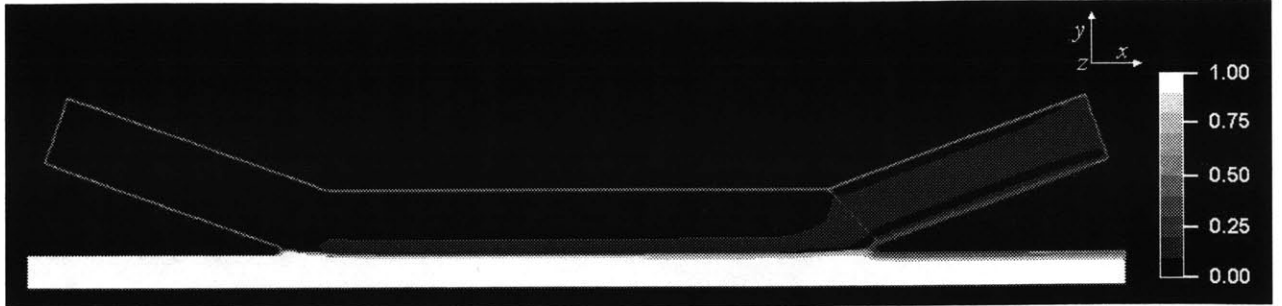


Figure 4.16. A band plot of the numerical results for the normalized mass transfer solution for peptide concentration

For saline, diffusion will play a more significant role in the concentration profile (Figure 4.17). The normalized plot of salt concentration shows that salt ions will diffuse deeper into the peptide solution further from the beginning of the peptide-saline interface. At the beginning of the peptide-saline interface, salt is barely present in the peptide solution stream. To get an estimate of the early gelling pattern, the plot of saline concentration can be superimposed over the plot of peptide concentration. Inside the regions where peptide and saline concentrations overlap, the areas where the saline concentration is above the critical coagulation concentration (CCC) can be identified (for NaCl, the range of the CCC = 1×10^{-4} to 1×10^{-3} M [7]). The peptide solution can be predicted to gel here, starting along the top edge of the overlap region and progressing toward the center of the device (Figure 4.18).

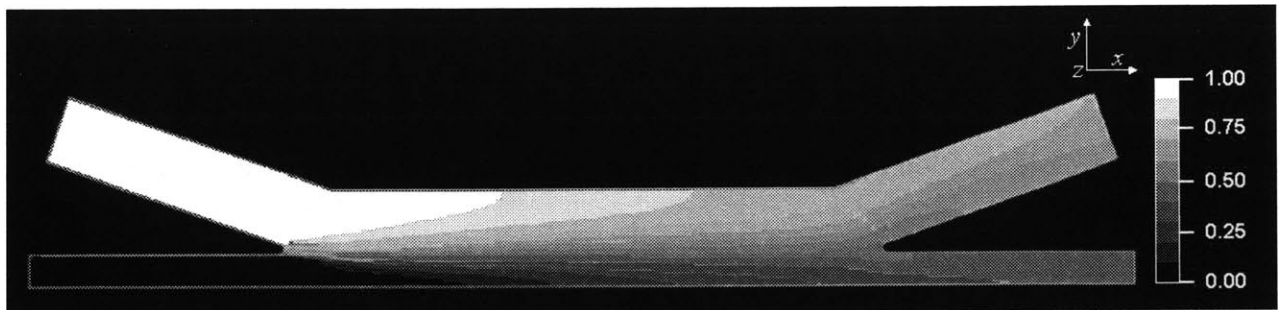


Figure 4.17. A band plot of the numerical results for the normalized mass transfer solution for saline concentration

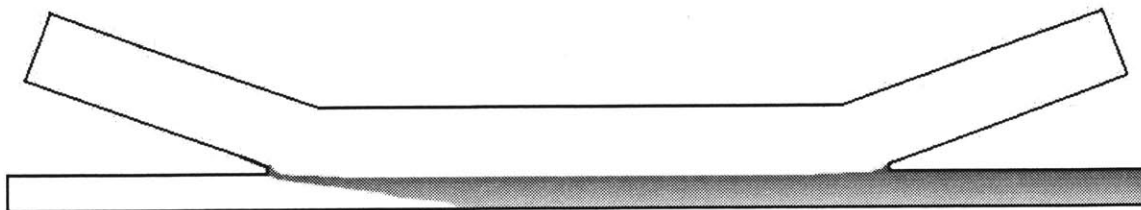


Figure 4.18. The overlapping region where concentrations of peptide and saline are sufficient for gelling

Pressure can be plotted to verify that it is equal in the y -direction in the converged-channel area of the device (Figure 4.19). In the truncated geometry, the pressure gradient in the saline inlet channel is not the same as that observed in the peptide inlet channel. Dissimilar gradients are also observed in the saline outlet channel and the peptide outlet channel. As long as the pressure differences between the beginnings of the inlet paths (the syringes) and the converged channel are not large enough to deform the hardware, the values are unimportant. The pressure differences between the converged channel and the ends of the center and side outlet paths will be equal in the setup; tubing from the outlet fittings will terminate at equal depth in a fluid reservoir. Prior analytic calculations for the outlet channel resistances and pressure drops will ensure that the outlet flow rates are properly regulated in the experimental work.

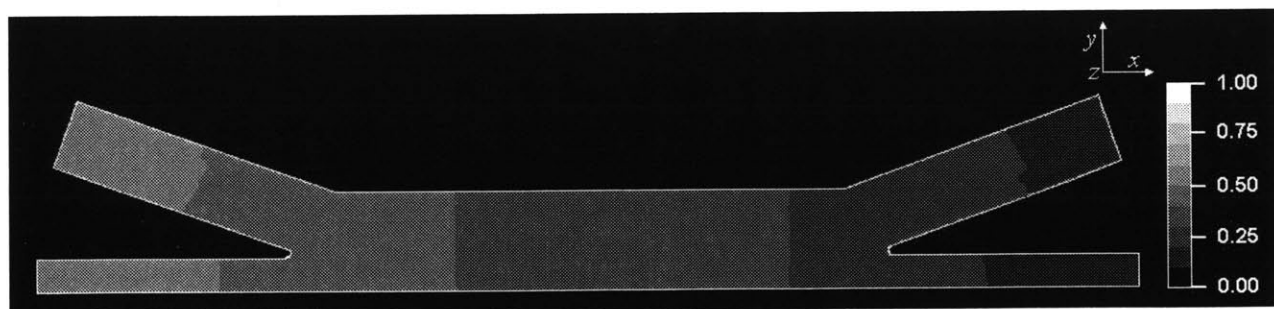


Figure 4.19. A band plot of normalized pressure in the device

4.4 Summary

Computational methods have been developed to optimize the experimental parameters. The analytic and numerical solutions of the Navier-Stokes and mass transfer equations were used

together to computationally determine the ideal flow rates and viscosity ratios for forming a peptide stream of desired width in the microfluidic devices. The numerical mass transfer solution was used to predict the initial gelling pattern of the peptide. These conditions were applied to the experimental protocols, as described in Chapter 5.

Chapter 5

Experimental Studies

The process of fabricating a peptide membrane between two micron-scale channels was developed and refined over several iterations. As a proof of concept, the process of membrane fabrication was first successfully attempted on a large scale (channel widths on the order of millimeters instead of micrometers). These experiments enabled the identification of problems that existed at both the macro- and micron-scale to be addressed in the micron-scale experiments. At the micron-scale, the analytic solution for flow was used to determine flow patterns and estimate optimal viscosity values for fluid flows in the devices. The subsequent micron-scale gel-forming experiments helped to further refine the methodology, and provide confidence in the future success of the project.

5.1 Macro-Scale Experiment

5.1.1 Macro-Scale Experiment: Introduction

The experimental setup for the membrane-forming experiment employed a single syringe pump equipped to simultaneously “push” and “pull” multiple syringes at a single plunger speed (see Figure 3.7). To infuse specific fluids, the appropriate syringes were mounted on the pump, and the unused syringes removed. By controlling flow rates in and out of the device, the need to address pressure and resistance effects in the inlet and outlet channels would, in theory, be

eliminated. In these early experiments, highly compliant Tygon™ tubing was used to make fluidic connections to and from the device (Figure 5.1).

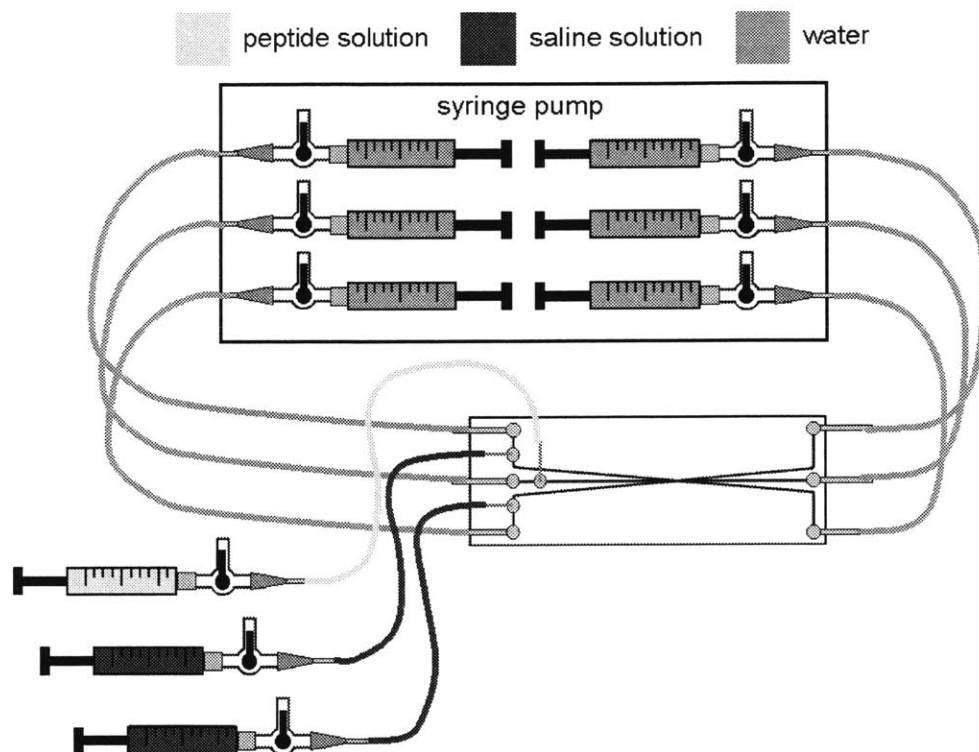


Figure 5.1. Schematic of the macro-scale experimental setup; tubing and syringes are not to scale. Syringes were mounted on and removed from the pump as they were needed (See Section 5.1.2 for the protocol).

To test the concept, device Fc8 (see Table 2.3 and Figure 5.2) was used. The larger geometries (channel widths on the order of millimeters instead of micrometers) exhibited much lower fluid resistances, exerting lower pressures on the fluidic setup. A gel formed at this scale would be much stronger than one that is micrometers wide, and would be easier to form and maintain.

5.1.2 Macro-Scale Experiment: Materials and Methods

For these experiments, fluidic connections were made with Tygon™ tubing (see Section 3.4 for specifications).

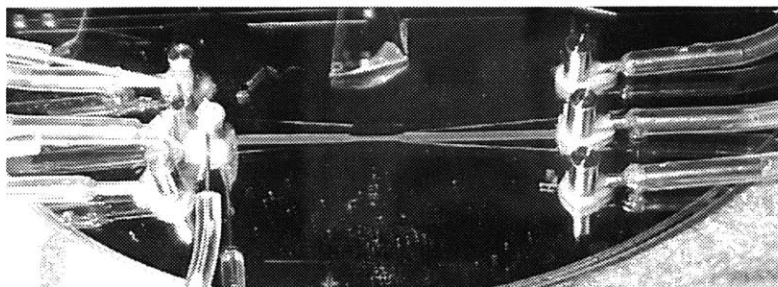


Figure 5.2. Device Fc8, shown with fluorescein dye flowing in through the center channel and out the outlet channels on the right

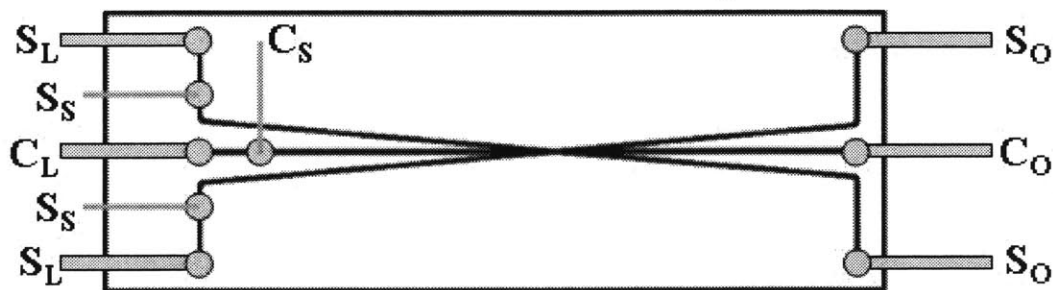


Figure 5.3. Device Fc8 fluidic ports, labeled as followed: C_L = large-bore center inlet, C_S = small-bore center inlet, C_O = large-bore center outlet; S_L = large-bore side inlets, S_S = small-bore side inlets, S_O = large-bore side outlets

The following protocol was followed to form the gel:

- A 1.0 weight percent KFE8 peptide solution was prepared and incubated for approximately two hours (see Appendix A5.1).
- The device was filled with water and all air bubbles were removed. Water was “pushed” into the device through the large bore inlets (C_L and both S_L ’s, see Figure 5.3 for inlet and outlet labels), and simultaneously “pulled” out through the outlets (Figure 5.4). Two syringe sizes were used: 5ml syringes attached to the center inlet and outlet, and 10ml syringes attached to the side inlets and outlets (Hamilton Gastight™ syringes, Hamilton Company, Reno, NV). This syringe configuration was chosen to flow a peptide stream in the center of the device of narrower width than the side saline streams.

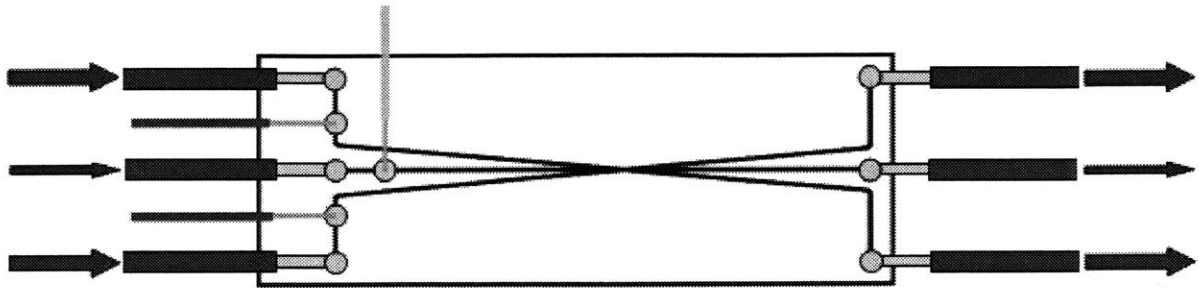


Figure 5.4. Water was “pushed” into the device through the large bore inlets and “pulled” out through the large-bore outlets.

- The water flow into the large-bore center inlet (C_L) was stopped and the syringe removed from the pump. The syringe containing the peptide solution was mounted on the pump and solution was infused through the small-bore center inlet (C_S) at $10\ \mu\text{L}/\text{min}$ (average velocity $6.67\ \text{mm}/\text{s}$, $Re = 0.0553$, $Pe = 205,825$). Water continued to be infused through the side channels (S_L 's) of the device at $20\ \mu\text{L}/\text{min}$ (average velocity $13.33\ \text{mm}/\text{s}$, $Re = 0.654$) (Figure 5.5).

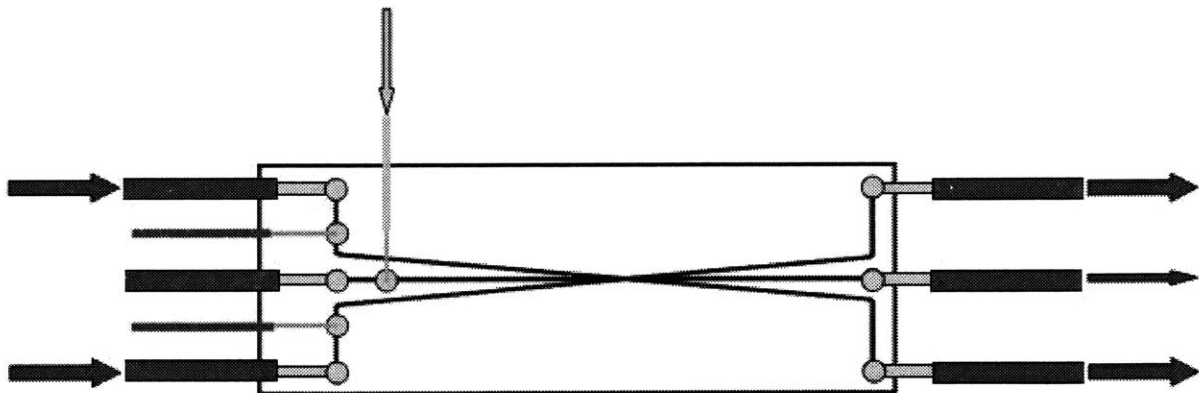


Figure 5.5. Peptide solution was infused through the center channel at $10\ \mu\text{L}/\text{min}$, while water was infused through the side channels at $20\ \mu\text{L}/\text{min}$.

- After a sufficient volume of peptide solution had been infused (a volume greater than the inner volume of the small bore inlet fitting and the inlet channel), water flow into the side channels (S_L 's) was stopped and these syringes were removed from the pump. The syringes containing a solution of saline, fluorescein, and Congo Red ($0.15\ \text{M}\ \text{NaCl}$, $0.01\ \text{M}$

fluorescein salt, 0.05 mg/ml Congo Red) were mounted on the pump, and this solution was infused through the side channel small-bore inlets (S_s) at 20 $\mu\text{l}/\text{min}$ ($Pe = 439$). The peptide flow was maintained at 10 $\mu\text{l}/\text{min}$ (Figure 5.6).

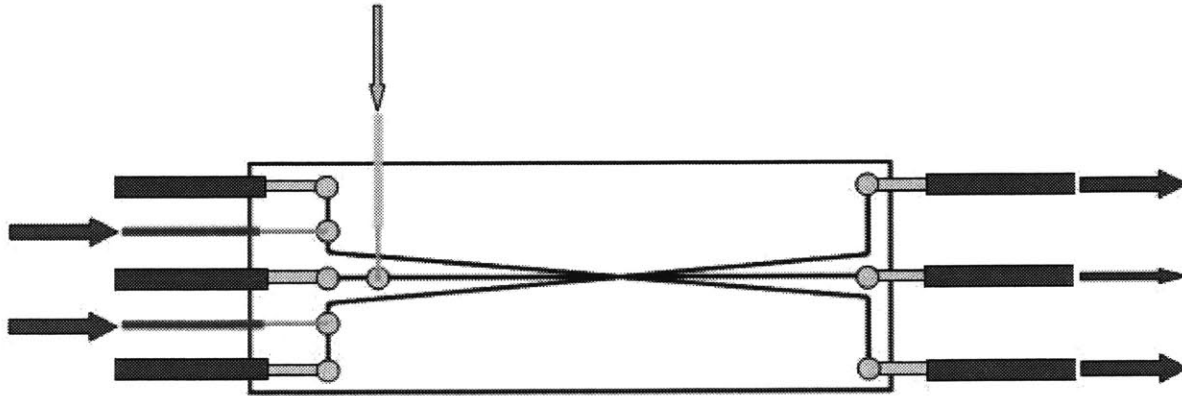


Figure 5.6. A solution of saline, fluorescein, and Congo Red was infused through the side inlets at 20 $\mu\text{l}/\text{min}$; peptide flow was maintained at 10 $\mu\text{l}/\text{min}$.

- When the saline solution was observed approaching the convergence of the channels (fluorescein in solution appears yellow through the microscope optics, and emits fluorescent green when observed with the naked eye through the glass wafer), the syringe pump was stopped.
- Fluid flow to and from the syringes was stopped (though as discussed later, this did not cause cessation of flows in the device). Salt diffused toward the center of the device, and the peptide formed a gel between the two side channels.

5.1.3 Macro-Scale Experiment: Results

In the experiment described above, nothing was observed until the saline-fluorescein-Congo Red solution was introduced into the device. As the solution approached the convergence of the channels, the pumps were stopped. However, fluid continued to flow through the device. A few seconds after the pump was stopped, the dye solution was clearly visible in the lower half

of the channel, and appeared very faintly in the top half (Figure 5.7). The center peptide stream (clear fluid) was pumped at a lower flow rate than the side saline streams, narrowing drastically at the convergence of the channels.

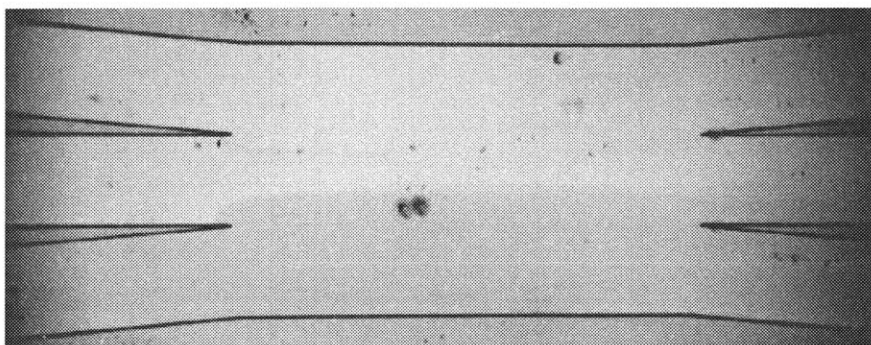


Figure 5.7. $t \sim 0$. The observed black marks and nicks were imperfections on the glass surface. This and the following images have been reversed to show flow from left to right.

At $t = 1:30$ [min:sec] after the pump had been stopped, the dye appeared to be at approximately equal concentrations on both sides of the center peptide stream (Figure 5.8). The interface between the peptide solution and saline solution was very clean at the leading edge of the convergence (left), but appeared to billow near the divergence of the channels.

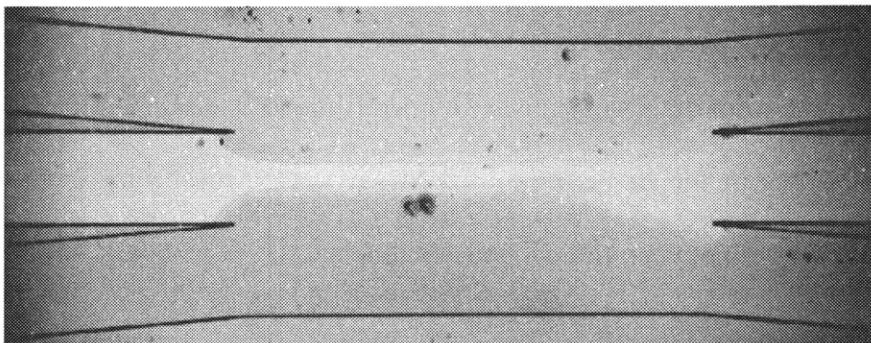


Figure 5.8. $t = 1:30$. The dye appeared to be at approximately equal concentrations on both sides of the center peptide stream.

At $t = 3:45$, some red staining of the peptide gel, though not readily visible in the CCD camera image, was perceived through the microscope eyepiece, due to the higher color and spatial resolution capabilities of the human eye (Figure 5.9). By $t = 24:00$, fluorescein had diffused

throughout the converged area and into the region where it was assumed that the peptide solution or gel was present. A dark line of stain was clearly visible along the top peptide-saline interface.

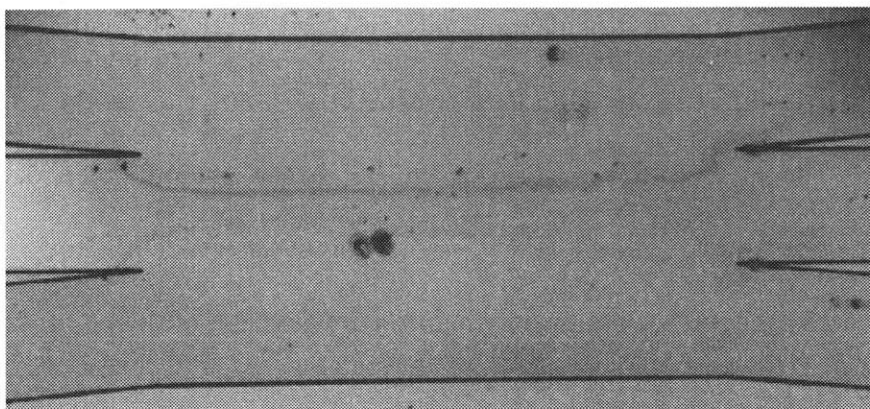


Figure 5.9. $t = 24:00$. Fluorescein has diffused throughout the converged-channel area.

At high magnification (Figure 5.10), Congo Red staining was visible along the upper leading edge of the interface, indicating the presence of peptide gel, and somewhat less so on the bottom. It appears that the peptide continued to be infused (from the left) for longer than it had been “pulled” from the right in the center channel, resulting in the left-right asymmetry, and suggesting that the flows did not cease at the time that the pump was stopped. As discussed later, this was due to compliance in the connecting tubing.

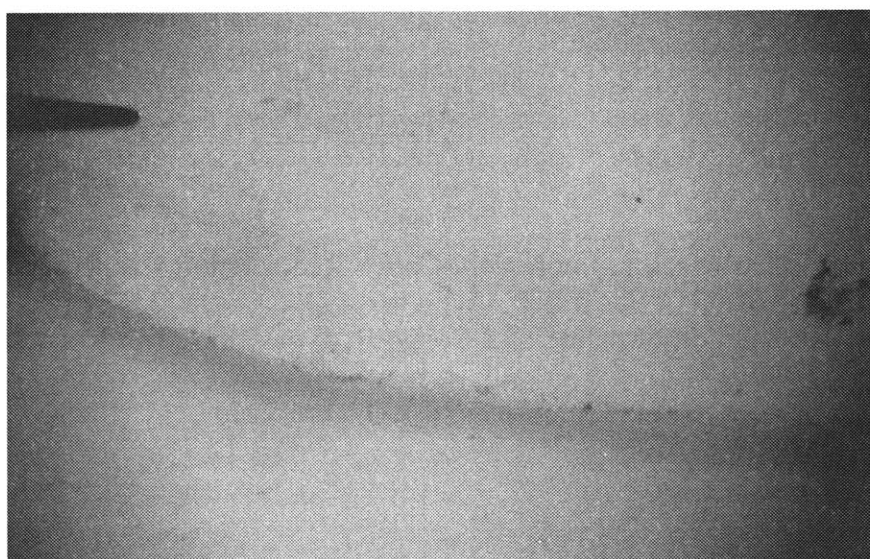


Figure 5.10. $t = 36:00$. High-magnification image showing Congo Red staining along the upper leading edge of the saline-peptide interface, indicating the presence of peptide gel

40 minutes after the saline was introduced and the pump stopped, the intensity of the Congo Red stain increased further. A region of peptide gel was observed that began on the left at the full channel width, narrowed in the middle, then widened to fill and exceed the width of the center outlet channel. The quality of the edge of the gel began smooth, then deteriorated in the downstream direction and appeared billowy, suggesting the presence of fluid vortices. Sections of gel also appeared in the saline and water channels downstream of the point where the channels diverge (Figure 5.11).

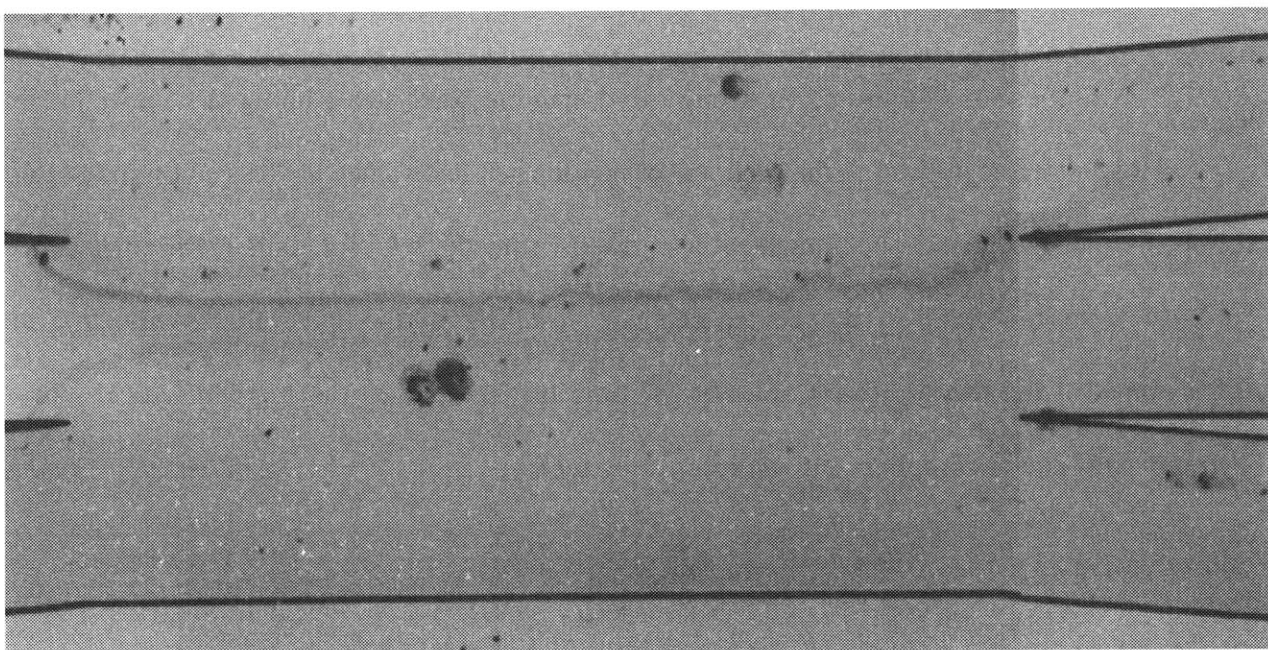


Figure 5.11. $t = 40:00$. The converged-channel area stitched from two images

Beginning at $t = 83:00$, the saline-fluorescein-Congo Red solution was flushed out through the side channels, and a solution of saline and Congo Red was flowed in to continue the staining process without the presence of the fluorescein dye (Figure 5.12).

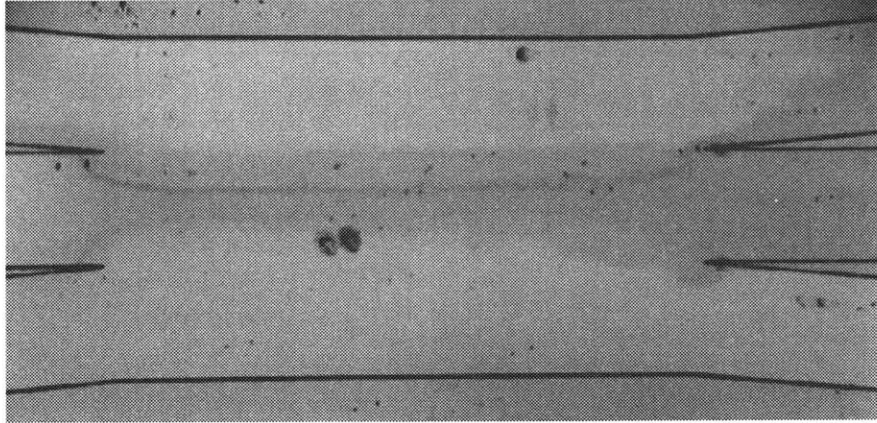


Figure 5.12. $t = 83:00$. Fluorescein was flushed from the device. Congo Red staining was very visible.

At $t = 86:00$, as fluorescein was flushed out, a crack was observed in the gel (Figure 5.13). Upon further examination, this feature was visible at $t = 83:00$, and was likely caused by a pressure difference across the gel.

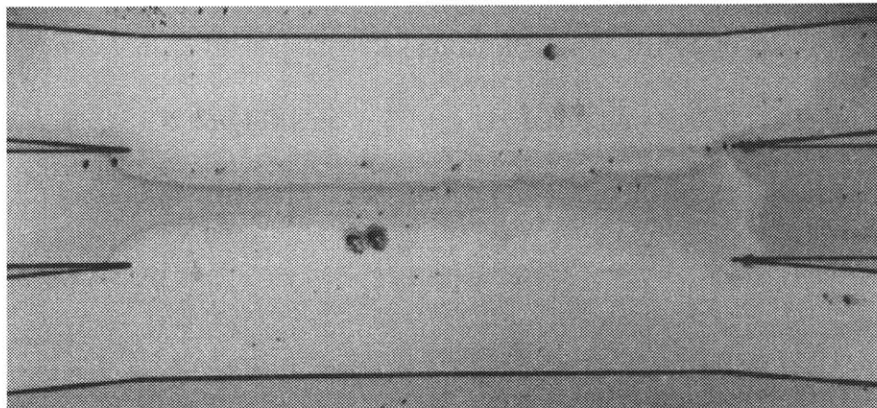


Figure 5.13. $t = 86:00$. The gel appeared torn at the divergence of the channels.

At $t = 164:00$, fluorescein had been flushed out of the channels and the device was left overnight filled with saline-Congo Red solution to stain (Figure 5.14).

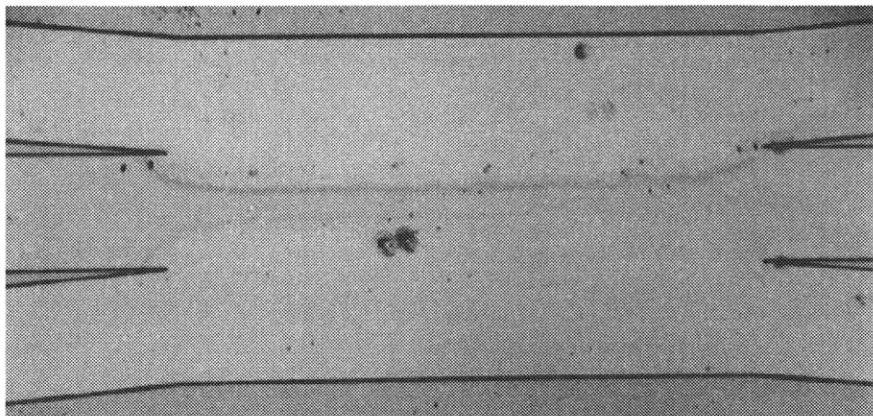


Figure 5.14. $t = 164:00$. Fluorescein has been removed from the device.
Congo Red stain is visible along the edges of the peptide region.

At $t = 19:30:00$ [hours:minutes:seconds], pumping of water through the device was started to flush out the saline-Congo Red solution. The syringe pump was mistakenly set to a high flow rate (20 ml/min). The pump was quickly stopped, but not before the peptide gel was damaged; the gel (stained very strongly by now with Congo Red) appeared to have more ruptures and the upper outlet channel contained many stained gel fragments (Figure 5.15). Because only the side channels had been used to flush fluids in and out, there was still fluorescein dye visible in the center outlet channel.

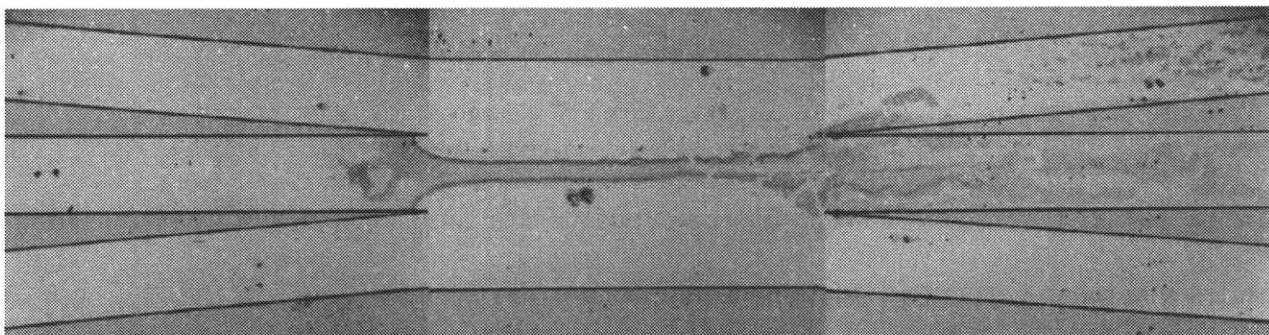


Figure 5.15. A “panoramic” view of device, showing the inlet channels (*left*) and the outlet channels (*right*).
Note the gelled and stained peptide particles in the upper right outlet channel.

High magnification images enabled inferences to be made on the nature of the gel structure (Figures 5.16, 5.16a, 5.16b, and 5.16c).

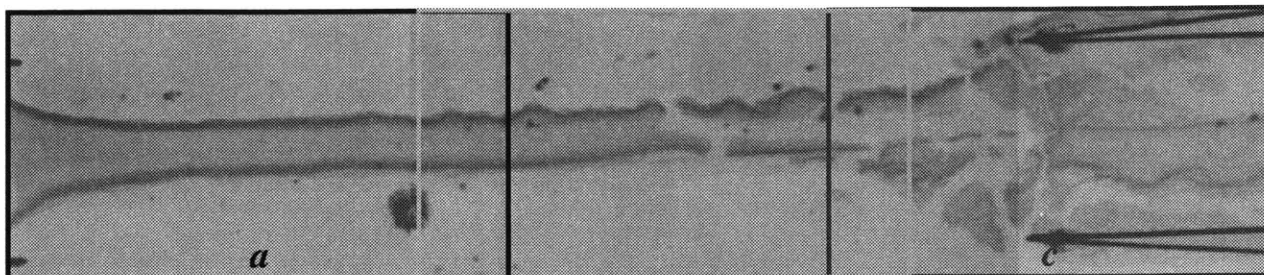


Figure 5.16. $t = 19:49:00$. High-magnification image of the fractured peptide gel membrane.

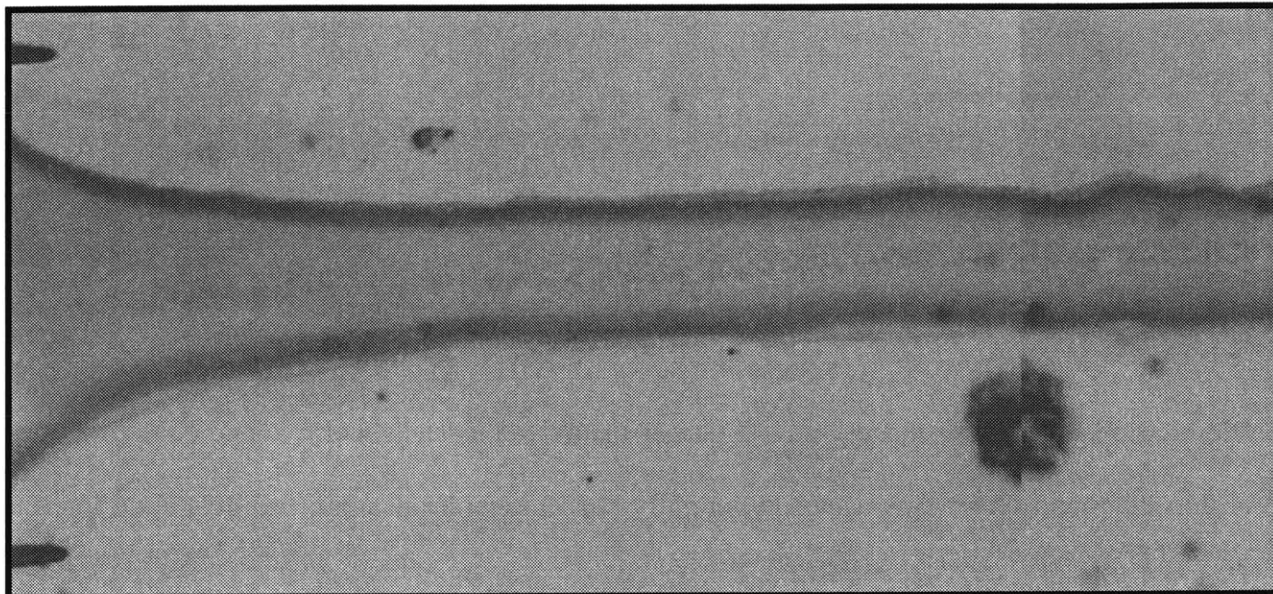


Figure 5.16a. Detail view *a* of Figure 5.16.

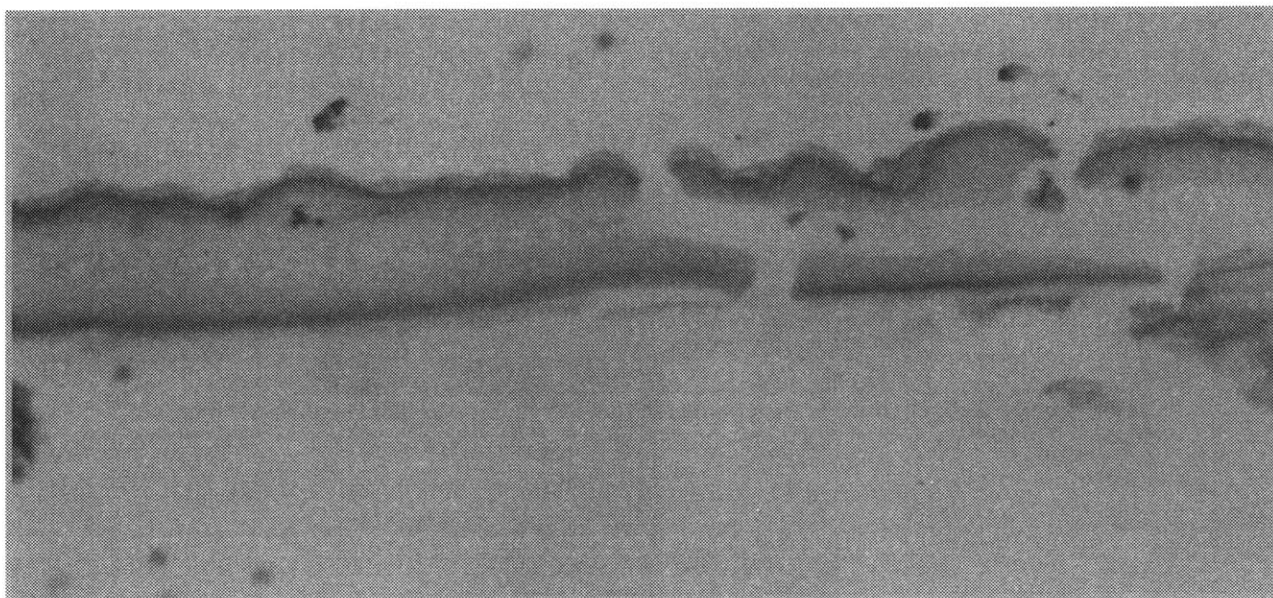


Figure 5.16b. Detail view *b* of Figure 5.16.

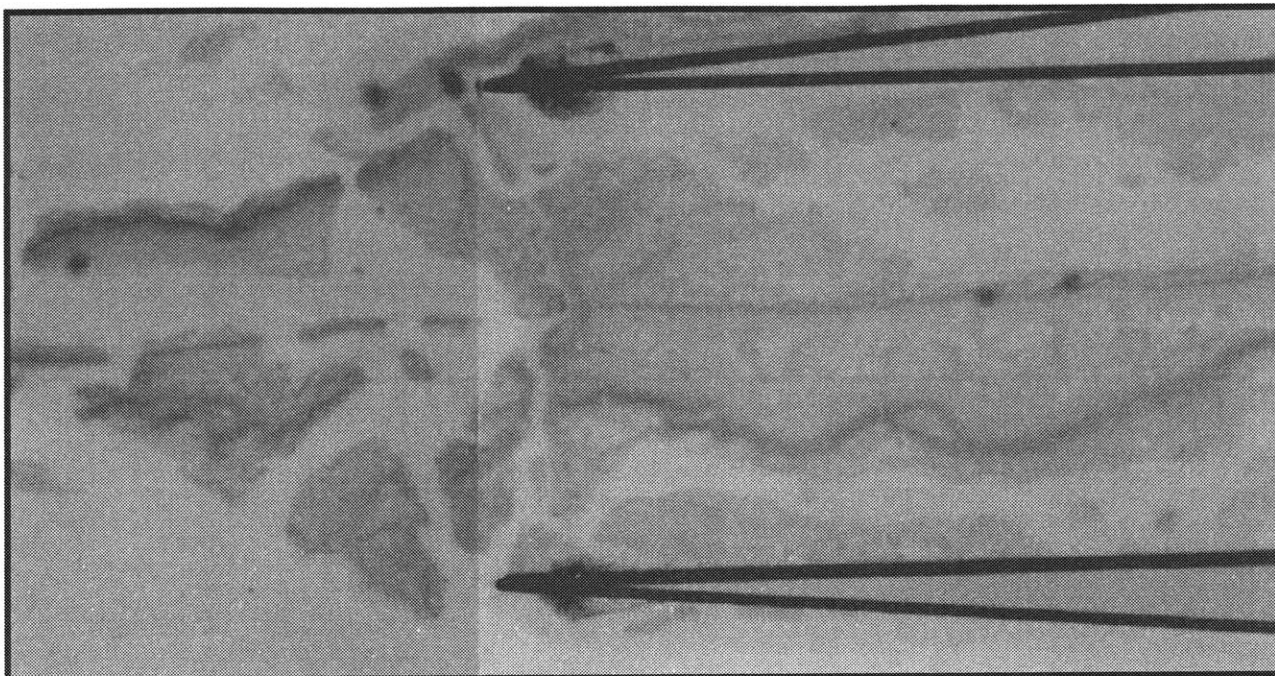


Figure 5.16c. Detail view *c* of Figure 5.16.

The high magnification images show a darker band of consistent width at the edge of the gel. Within this band, there was a narrow, slightly darker region all along the gel-saline interface (Figure 5.17b).

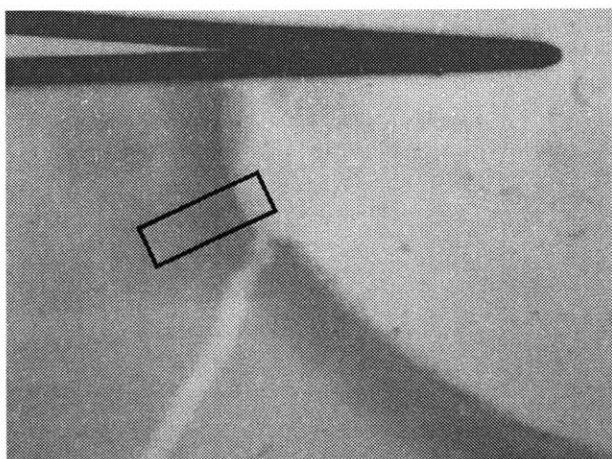


Figure 5.17. High-magnification image showing the Congo Red staining gradient.

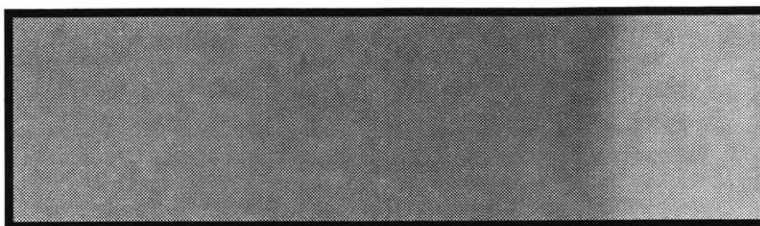


Figure 5.17b. Detail view of Figure 5.17. Note the staining gradient and the dark edge of the stained region on the right.

5.1.4 Macro-Scale Experiment: Discussion (The Congo Red Stain Gradient)

These images provided insight into the structure of the gel. It was fairly certain that the stained areas filled the full height of the channel, and were not stuck to the top or bottom surface. The broken gel (Figures 5.15, 16, and 17) showed clean, well-defined edges where the gel appeared to have fractured, suggesting that these fragments spanned the entire height of the channel.

The gradient in color caused by the Congo Red stain can be explained in one of two ways. One hypothesis is that the gradient was a result of the diffusivity time scale for the Congo Red. If it is assumed that the gel spanned the full height of the channel, only the edge was initially exposed to the Congo Red solution, and staining first occurred in a band along the edge of the gel. If the Congo Red was allowed to diffuse further into the gel, the width of this band would have increased over time.

Alternatively, there could be a gradient in peptide gel density. Congo Red may have infiltrated the entire center stream region and stained areas of higher β -sheet concentration more intensely than areas of lower concentration. The concentration gradient could be caused by capacitance in the center water inlet path. This capacitance could cause water to be infused through the device after gel formation had started at the edges, diluting the peptide solution in the center of the stream (Figure 5.18).

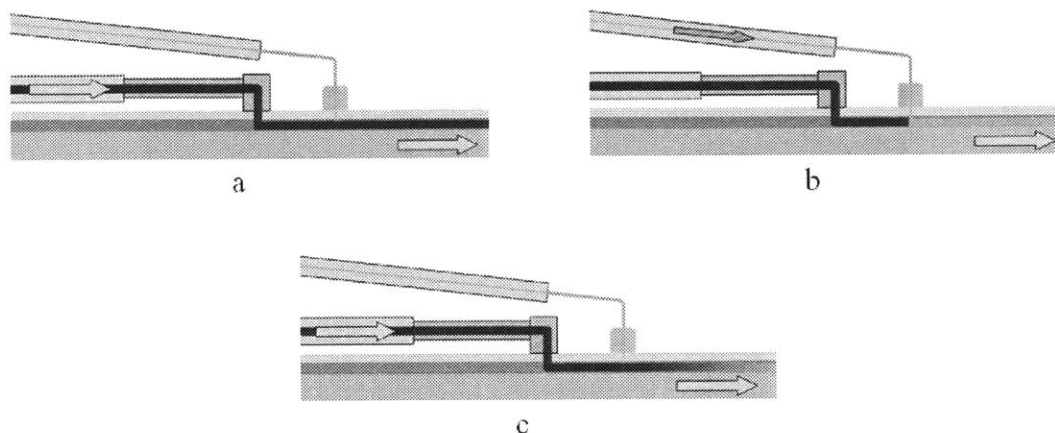


Figure 5.18. (a) Water is flowed through a large-bore inlet, while the peptide solution is in the small-bore inlet path. (b) Peptide solution is infused into the device, causing pressure to build up and expand the large-bore inlet tubing. (c) The syringe pump infusing the peptide is stopped and pressure in the small-bore path falls. The tubing in the large-bore inlet path contracts and causes water to flow into the device.

Another possible cause of the concentration gradient is the mechanics of peptide gelation. Filaments could nucleate at the edges of the peptide stream, then monomers in the center of the stream could migrate and join the cross-linked filaments at the edges. The inside edge of the stained band was fairly discrete, implying that except for a background level of stained peptide monomers and filaments, all of the monomers may have been drawn to the edges and “settled,” much like sediment, in a band of nearly uniform width.

5.1.5 Macro-Scale Experiment: Conclusions

In this experiment, formation of a gel between two channels was successful. The second goal was to identify potential problems and address them when formulating the micron-scale protocol. Either a staining or peptide gradient was observed in the gel. Further work will be necessary to determine the cause and mechanism of this phenomenon, which may not be an issue at the micron-scale (see Section 6.3).

One issue that will definitely have effects at the micron-scale is compliance. Compliance in the system is quite high; after the syringe pump was stopped, flow in the device continued for

times on the order of minutes. The silicon-glass device and the syringes (glass syringes with Teflon plungers) were quite rigid. The stopcocks were made of fairly hard plastics. The tubing, however, was quite elastic. Because flow rates were specified by the syringe pump, pressure drops along the fluid paths were uncontrolled, and the diameter of each compliant section of tubing varied depending on the distribution of internal pressure. When the pump was stopped the tubing contracted or expanded, pushing or pulling fluid through the device as it returned to a state of uniform internal pressure.

The center peptide stream was infused at one-half the flow rate of the side saline flows, but it narrowed further due to pressure buildup in the tubing. In the process of initiating, stopping, and switching flows, flow paths became pressurized and de-pressurized at the stopcock connection. This de-pressurization caused higher pressure drops in the side flow paths, resulting in uncontrolled saline flow rates higher than those specified by the syringe pump, and causing the center peptide stream to be narrower than expected. By eliminating or minimizing compliance, these effects would also be minimized, and the peptide stream width could be controlled by the syringe pump flow rates.

To minimize problems due to compliance, small-bore, thick-wall Teflon™ tubing (ETFE tubing, O.D. Ø0.063 in., I.D. Ø0.012 in.) was used in the micron-scale experiments in place of the larger bore, more compliant tubing. The material is flexible and partially transparent, allowing visual monitoring of fluids and air bubbles.

To further reduce compliance, the total length of tubing in the system was reduced by simplifying the fluid paths. The large-bore center inlet (C_L) (see Figure 5.3 for inlet and outlet labels) was plugged. The switch from water to peptide flow through the center channel was modified to be implemented by detaching the water syringe and tubing at the metal fluidic

fitting, then attaching the peptide solution syringe and tubing (Figure 5.21). This eliminated the tubing that connected the large-bore center inlet (C_L) to the water syringe assembly, and reduced the possibility of peptide flowing out through the large-bore inlet, or water flowing in through the large-bore inlet into the peptide solution, resulting in a diluted peptide concentration.

The “pulling” syringes at the outlet were eliminated; large-bore tubing attached to the outlets (C_O and S_O ’s) simply drained into a constant-pressure fluid reservoir. This reduced tubing compliance and eliminated the deleterious effects of negative pressure on the system. The negative pressure created by “pulling” sometimes caused dissolved gasses in the fluids to come out of solution. The resulting air bubbles can be another source of system compliance, and are hard to find and eradicate, especially if they form inside the stainless steel fluidic fittings. An unfortunate consequence of removing the pulling syringes is that the outflow rates can no longer be directly controlled. The remaining parameter, viscosity, can be adjusted to control the outflow rates to create the desired flow pattern (see Section 4.2.3).

5.2 Micron-Scale Viscosity Experiment

5.2.1 Micron-Scale Viscosity Experiment: Introduction

Both the macro-scale experiments and analytic studies suggested that membrane formation in the micron-scale system can be accomplished by exerting close control over the viscosity ratio between the peptide solution and the saline solution, $\mu_{\text{saline}}:\mu_{\text{peptide}}$. The width of the peptide stream and the outlet flows can thus be controlled through the viscosity ratio and the inflow rates. This is complicated by the fact that the viscosity of the peptide solution changes with time as the peptide incubates due to polymerization over a long time scale, even in the absence of salt [25]. It is therefore critical to have a simple and reliable means of measuring and

adjusting the solution viscosities just prior to an experiment. In this section, development of the micron-scale device as a rough viscometer is described. The device can be used immediately before attempting a gel-forming experiment to measure the viscosity of the peptide solution. A pre-mixed saline-Dextran solution of appropriate viscosity can then be chosen based on the measured value.

5.2.2 Micron-Scale Viscosity Experiment: Methods

For these experiments, two syringe pumps were used to infuse fluids at different flow rates (Figure 5.19).

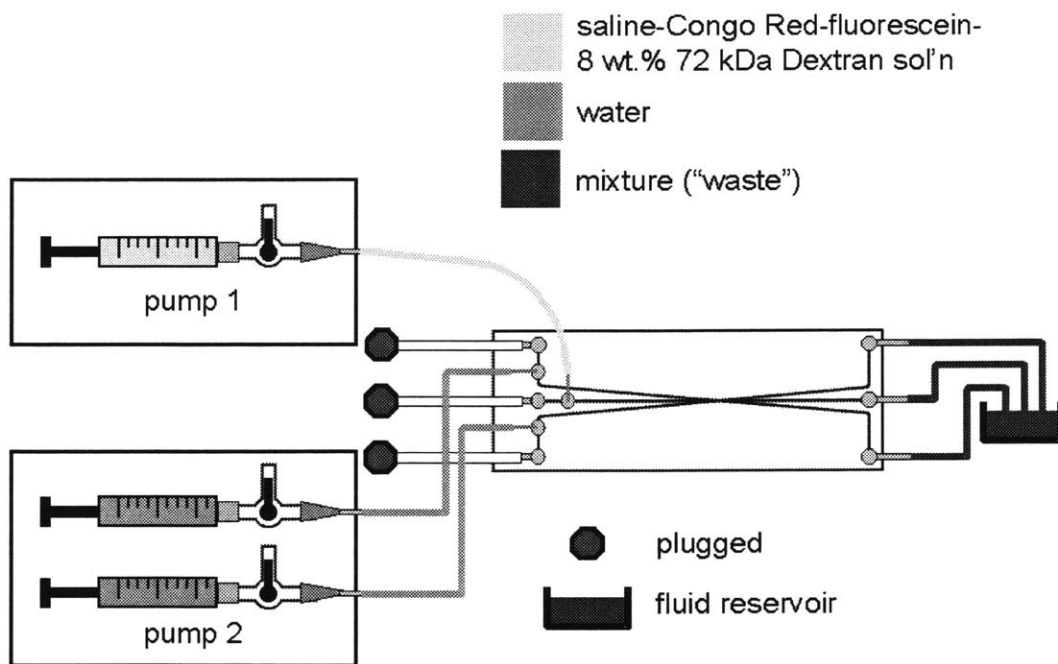


Figure 5.19. Schematic of setup for the micron-scale viscosity experiment

Device Fc1 was used with the following protocol:

- All fluids were held at room temperature for several hours after being removed from storage at 4°C.
- The device was filled with water and all air bubbles were purged.

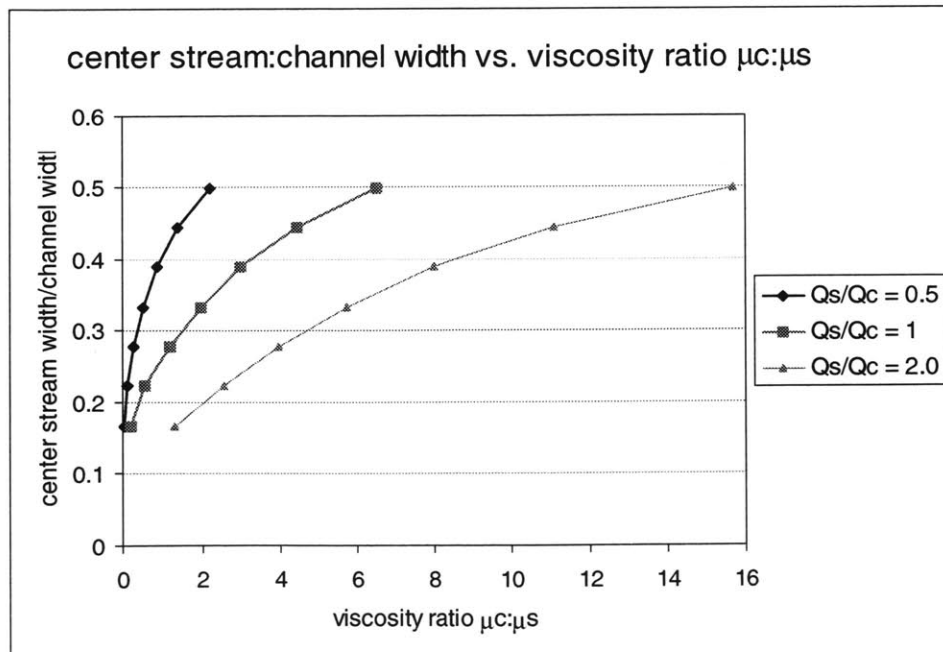
- Water was infused into the side channels of the device through the large-bore side inlets S_L 's. A solution of 0.15 M saline, 0.05 mg/ml Congo Red, 0.01 M fluorescein salt, and 8.00 weight percent 72 kDa Dextran was infused through the center small-bore inlet channel C_S . An 8.00 weight percent solution of 72kDa Dextran has a relative viscosity $\mu/\mu_0 = 5.963$; the relative viscosity of a 0.15 M solution of saline is $\mu/\mu_0 = 1.016$ (where μ_0 is the viscosity of water) [32]. The viscosity of fluorescein salt in solution was not measured or available. The total viscosity of the saline-Congo Red-fluorescein-Dextran solution is dominated by the Dextran. Thus, the viscosity of the solution is at least 5.963 times that of water, most likely slightly higher due to the viscosity contributions of the other species.
- The fluids were pumped at a specified flow rate for five minutes. After this time, an image of the converged-channel region was captured with the microscope-CCD camera system. The field was illuminated with both the UV fluorescence source and white light.
- The flow rates were changed and held for five minutes, and an image of the converged-channel region was captured. This step was repeated until images for all the specified flow rates had been collected.

The flow rates were chosen to give a range of side flow rate-to-center flow rate ratios ($Q_{side}:Q_{center}$). The order in which the flow rates were specified jumped between $Q_{side}:Q_{center} \leq 1$ to $Q_{side}:Q_{center} > 1$ to negate potential compliance effects that might accumulate if the flow rates were either continually increasing or decreasing (Table 5.1). To calculate the maximum Reynolds numbers (max Re), the viscosity of the center stream was set to that of water, which is the lower-bound of the actual value, yielding the maximum Reynolds number. Using this artificially lower value still shows flow in the viscous-dominated regime for all flow rates.

Table 5.1. Flow rate data for the micron-scale viscosity experiment

time [min]	inlet flowrate		Qs/Qc	max <i>Re</i> [LV/v]	<i>Pe</i> fluorescein [VL/D]
	sides [μl/min]	center [μl/min]			
0	0.33	1.00	0.33	5.787	1753.648
5	1.50	1.00	1.50	13.889	4208.754
10	0.50	1.00	0.50	6.944	2104.377
15	2.00	1.00	2.00	17.361	5260.943
20	1.00	1.00	1.00	10.417	3156.566
25	3.00	1.00	3.00	24.306	7365.320

The width of the center fluorescent stream was measured in each image (see Appendix A5.2 for the measurement procedure). The Peclet numbers (*Pe*) show strong convection dominance, indicating the minimal effect of fluorescein diffusion on the measurements. For values of center stream width, side flow viscosity (water), and flow rate ratio $Q_{\text{side}}:Q_{\text{center}}$, the analytic solution (developed in Section 4.2) can be used in an iterative process to determine the viscosity of the center flow (sample values shown in Figure 5.20). The experimental values obtained were used in this process to determine the unknown center flow viscosity (μ_{center}) (see Appendix A5.3 for this procedure).

**Figure 5.20.** A plot of the normalized center stream width as a function of the viscosity ratio $\mu_{\text{center}}:\mu_{\text{side}}$

5.2.3 Micron-Scale Viscosity Experiment: Results and Discussion

From the micron-scale velocity experiments, six data points were recorded, producing six different values for the calculated viscosity of the saline-fluorescein-Congo Red-Dextran solution (Table 5.2).

Table 5.2. Calculated viscosity values from center stream measurements

Qs/Qc	dye width [μm]	calc. rel. viscosity $\mu_{\text{test}}(\text{sol'n})/\mu_0$	
0.33	13.690142	3.19	for n = 6
1.50	21.191491	6.0086	mean = 5.87
0.50	14.151525	5.58	st. dev. = 1.47 25.12 % of mean
2.00	22.212766	7.36	
1.00	17.493059	7.022	for n = 5 (discarded Qs/Qc = 0.333 point)
3.00	26.553193	6.055	mean = 6.41
			st. dev. = 0.75 11.72 % of mean

Most of the values vary within or close to a standard deviation from the mean, except for the viscosity value corresponding to $Q_{\text{side}}:Q_{\text{center}} = 0.333$. The viscosity calculation is quite sensitive to the measured center stream width. While the image measurements can be highly repeatable, measuring to the edges of the center fluid stream is more subjective due to the “fuzziness” of the interface between the fluorescent dye and the water. Small changes in this measurement can have a large effect on the calculated viscosity value. Using the Student’s t test, the $Q_{\text{side}}:Q_{\text{center}} = 0.333$ point is found to be an outlier at a confidence level of 99 percent and is discarded. The standard deviation for the n = 5 sample reduces to less than 12% of the sample mean. The mean value of the remaining five points, $\mu/\mu_0 = 6.41$, is a rough estimate for the relative viscosity of the saline-fluorescein-Congo Red-Dextran solution. The expected viscosity is a value that is slightly higher than the viscosity of an 8.0 weight % 72kDa Dextran solution; the experimental result is therefore a reasonable value for viscosity.

5.2.4 Micron-Scale Viscosity Experiment: Conclusions

By performing simple flow experiments with the device, a rough approximation of fluid viscosity can be obtained using very small sample volumes. This will be useful for the gel-forming experiments, where the ratio of peptide to saline viscosity must be controlled, but the peptide viscosity changes with time and must be determined prior to the gel-forming experiment. The measured value agrees with the predictions, confirming that the micron-scale device can be confidently used as a rough viscometer.

5.3 Micron-Scale Membrane-Forming Experiment:

Micro Experiment Design I- μ

5.3.1 Micro Experiment Design I- μ : Introduction

The primary focus of the experimental work was the fabrication of a peptide gel between two cell-scale channels in a micron-scale device. Prior to in-depth analytic and numerical inquiry, peptide gelling experiment parameters were determined through trial-and-error. Despite the lack of these theoretical studies, an encouraging level of success was achieved. Although fabrication of a peptide gel with the desired properties was not successful, feasibility was demonstrated. It is expected that further efforts taking advantage of past experimental work and the computational results are very likely to produce a successful result.

5.3.2 Micro Experiment Design I- μ : Methods and Results

For the initial micron-scale experiments, formation of a gel membrane was attempted in device Fc1. This device, with its wide center channel (dimension 'c' in Table 2.3), was designed

to form a wide gel membrane that would be more stable and stronger than those formed in the other micron-scale devices. The approach was to flow a stream of peptide solution between two streams of saline. When the peptide solution began to gel, the syringe pump driving the center flow was stopped; due to compliance, flow in the center channel slows, but does not completely stop. To accommodate this flow, when the peptide solution began to gel the saline flows in the side channels were reduced by $\sim \frac{2}{3}$; after some time, the saline pump was stopped and gelation was allowed to proceed. The system setup was simplified to minimize the length of tubing used. Small-bore Teflon™ tubing (see Section 3.4 for specifications) was used for all fluid connections. A plug was placed in the large-bore center inlet (C_L). Tubing was connected to the large-bore outlets C_O and S_O 's. The ends of these three tubes were held at equal depth in a shallow fluid reservoir. The reservoir was used to eliminate droplet formation (and the associated pressure fluctuations) that would occur if the tubes terminated in air; the depth was kept shallow to minimize additional hydrostatic pressure on the outlets.

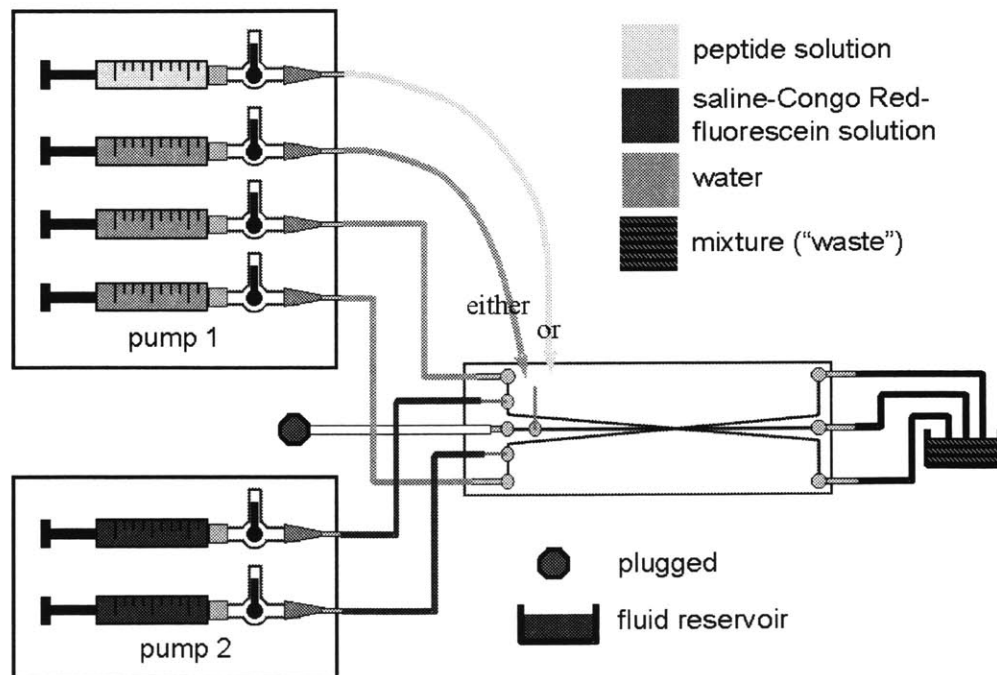


Figure 5.21. Schematic of the setup for the micron-scale membrane forming experiment designated Micro Experiment Design I-μ

Below, the protocol and experimental results for a trial run are presented (Table 5.3).

Table 5.3. Quantitative outline of the micron-scale membrane forming experiment

Stage of the experiment	t [min:sec]	inlet	fluid	flow rate [$\mu\text{l}/\text{min}$]	total inlet [$\mu\text{l}/\text{min}$]
Prepare experiment, confirm equal resistance	-	center (C_s)	water	1.0	1.0
		sides large-bore (S_L)	water	0.0	
		small-bore (S_S)	saline	1.0	
Infuse peptide	-	center (C_s)	peptide	1.0	1.0
		sides large-bore (S_L)	water	1.0	
		small-bore (S_S)	saline	0.0	
Infuse saline, begin gelation	0:00	center (C_s)	peptide	0.09	0.42
		sides large-bore (S_L)	water	0.09	
		small-bore (S_S)	saline	0.33	
Slow flow, continue gelation	0:40	center (C_s)	peptide	0.00	0.11
		sides large-bore (S_L)	water	0.00	
		small-bore (S_S)	saline	0.11	
Slow flow further, continue gelation	1:22	center (C_s)	peptide	0.00	0.003
		sides large-bore (S_L)	water	0.00	
		small-bore (S_S)	saline	0.003	

5.3.2.1 Prepare Experiment, Confirm Equal Resistance

- A 1.0 weight percent KFE8 peptide solution was prepared and incubated for approximately 2 hours (see Appendix A5.1 for the procedure).
- The entire device was filled with water, and air bubbles were removed.
- Saline-fluorescein-Congo Red solution was pumped into the two side channels through S_S 's while water was pumped through the center channel C_S (Figure 5.22).

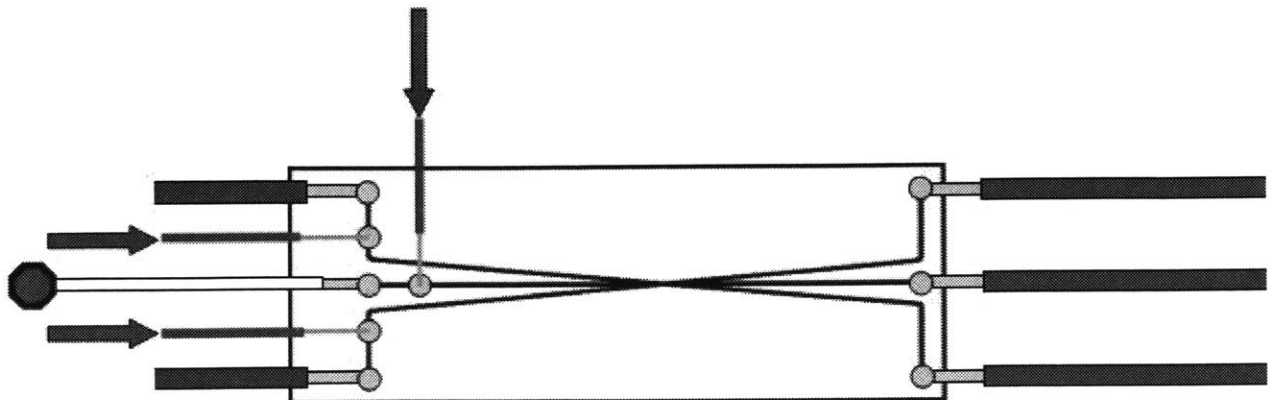


Figure 5.22. Saline-fluorescein-Congo Red solution was pumped into the two side channels through S_S 's while water was infused through the center channel.

Flow appeared to be symmetric, laminar and parallel to the center channel axis. This implied that the side outlet channels had approximately equal resistances, and were clear of obstruction. The faint red marks were Congo Red stain marks left on the top and bottom inside surfaces from previous gelling attempts. They did not appear to disrupt the flow (Figure 5.23).

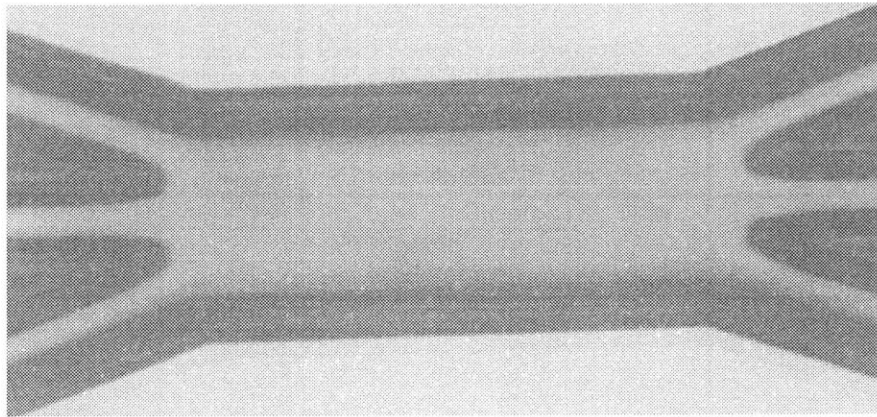


Figure 5.23. Laminar flow and an unclogged device were verified.

- Water was flowed through the large-bore side inlets S_L 's and the small-bore center inlet C_S until fluorescein dye was no longer visible flowing through the converged-channel device area (Figure 5.24).

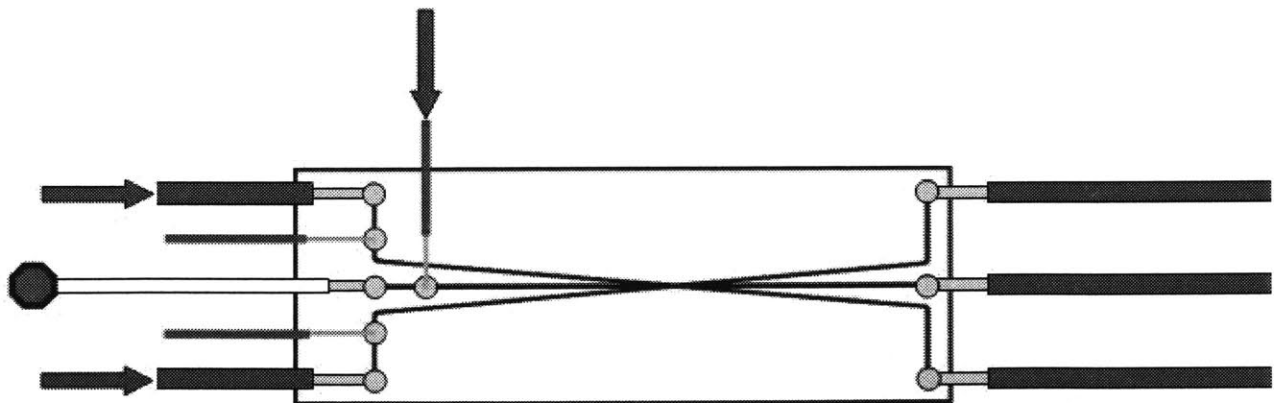


Figure 5.24. Water was flowed through the device until fluorescein dye was no longer visible.

At this point, saline solution should fill the fluidic path up to the fluid fitting-glass interface (Figure 5.25).

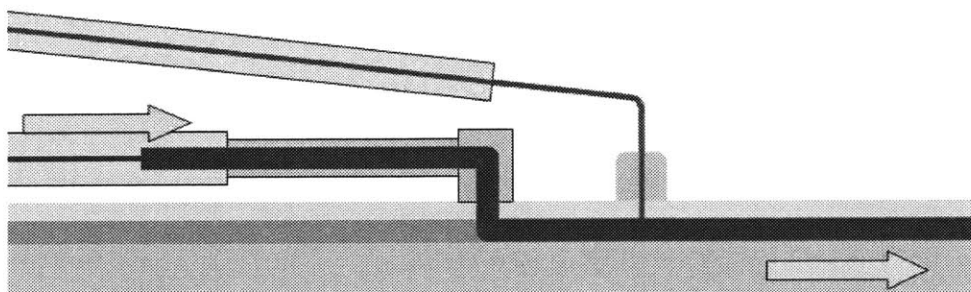


Figure 5.25. When solution is pumped through a small-bore inlet and stopped, then solution is infused through the large-bore inlet, solution in the small-bore path should be present right up to the intersection of the two flows, not accounting for diffusion effects.

5.3.2.2 Infuse Peptide

- The center water syringe was removed from the device by detaching the tubing at the small-bore fluidic fitting, and the peptide syringe was attached. Peptide was infused through the center channel while water was flowed through the side channels (S_L 's). Approximately 15 μ l from the peptide and each water syringe was infused through the system to ensure that full-concentration peptide solution was flowing across the converged-channel region (Figure 5.26).

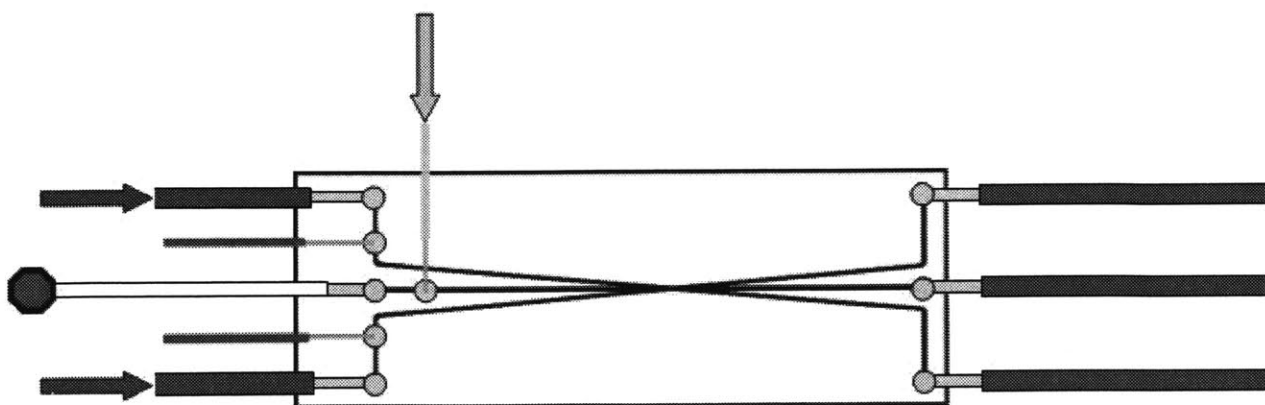


Figure 5.26. Peptide was infused through the center channel while water was flowed through the side channels.

5.3.2.3 Infuse Saline, Begin Gelation

- For the pump driving the peptide solution (C_S) and the side channel water flows (S_L 's), the flow rate on Pump 1 (see Figure 5.21) was set to 0.09 $\mu\text{l}/\text{min}$ ($v_{\text{average}} = 0.06 \text{ mm/s}$, $Re_{\text{center}} = 2.25 \times 10^{-4}$, $Pe_{\text{center}} = 911$). Pump 2, the syringe pump infusing the side saline flows (S_S 's), was set to 0.33 $\mu\text{l}/\text{min}$, making each side flow rate 0.42 $\mu\text{l}/\text{min}$ (0.28 mm/s, $Re_{\text{sides}} = 0.68$, $Pe_{\text{sides}} = 453$) ($Q_S:Q_C = (0.42 \text{ } \mu\text{l}/\text{min}):(0.09 \text{ } \mu\text{l}/\text{min}) = 4.67:1$). This flow rate ratio was chosen empirically through trial and error to produce a peptide stream one-third the width of the converged-channel device area. The pressure drops across the outlet channels were not accounted for in these experiments. The infusion of water and saline solution in the side channels lowered the salt concentration to 0.118 M, which was still well above the concentration necessary for gelation [7]. Both pumps were started. As soon as saline-fluorescein-Congo Red solution was visible in the converged-channel area, video recording was started and the experiment time was reset to $t = 0$.
- The peptide began to gel immediately. Figure 5.27 shows the device at $t = 0:31$ [minutes:seconds]. A thin skin appeared to form on the outer surfaces of the center peptide stream. The quality of the interface appeared to deteriorate, however, toward the downstream end of the system, suggesting that some peptide solution had spread out from the central channel.

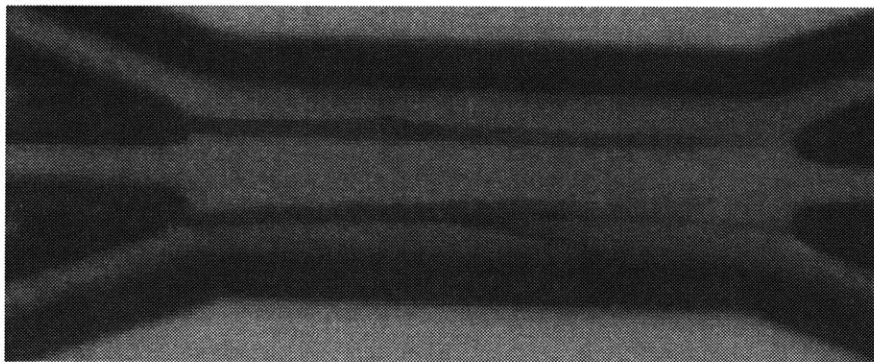


Figure 5.27. $t = 0:31$. A thin 'skin' appeared to form on the outside surfaces of the center peptide stream.

5.3.2.4 Slow Flow, Continue Gelation

- At this stage, it would be desired to stop all flows simultaneously so that gelation could proceed without any flow disturbance. Due to the remaining compliance in the system, stopping the pumps would not cause immediate flow cessation. In previous micron-scale experiments, the flow in the center channel appeared to continue after flow in the side channels had stopped; this could be the result of higher pressures generated in the peptide flow path due to the higher viscosity of peptide solution. Control over the flow rates was attempted so that the flows would gradually slow and stop simultaneously. Pump 1 was stopped (driving the center peptide flow (C_S) and the side water flows (S_L 's)) and the flow rate of Pump 2 was reduced (driving the side saline flows (S_S 's)) to $0.11 \mu\text{l/min}$ at $t = 0:41$ (Figure 5.28).

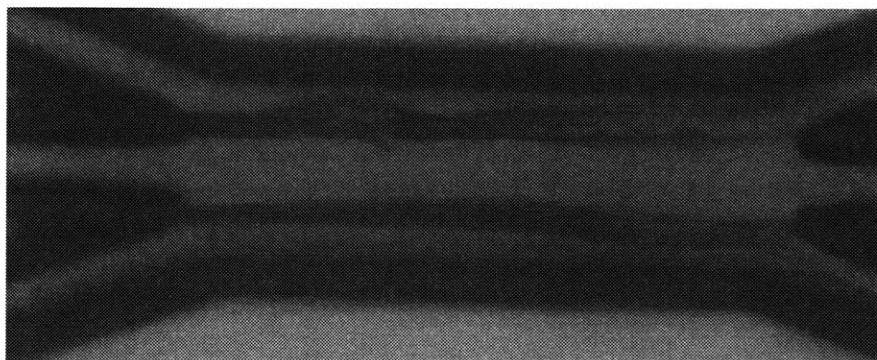


Figure 5.28. $t = 0:41$. Infusing flow rates were reduced to allow further gelation of the peptide solution.

- At $t = 1:22$, the side saline flow rate (S_s 's) was reduced to $0.003 \mu\text{l}/\text{min}$, but not stopped, to maintain pressure on the syringes and prevent back-flow.
- The gelling pattern of the peptide solution was monitored (Figure 5.29). At this point there appeared to be a central region of ungelled peptide contained within a continuous gelled “skin.”

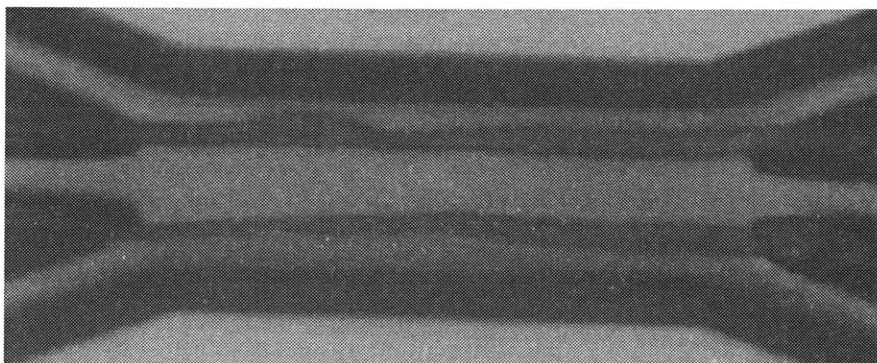


Figure 5.29. $t = 1:28$. The peptide gel ‘skin’ appeared quite thick with distinct edges.

- At $t = 6:05$ the dark gelled areas seemed to wash away, revealing a transparent, Congo Red-stained structure (Figure 5.30). Fluorescein dye began to appear in the center stream, indicating either diffusion through the gel, or a rupture in the peptide gel skin.

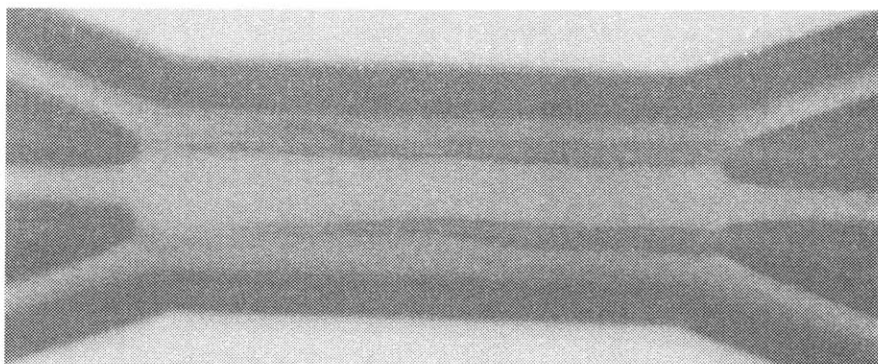


Figure 5.30. $t = 6:05$. The dark gelled regions appeared to wash away, leaving transparent Congo Red-stained structures.

- As time passed, it became clear that the peptide gel skin had reached its thickest dimension. Saline-fluorescein-Congo Red solution had infiltrated the center of the device, but no further

gelling was visible (Figure 5.31). This implies that peptide solution was no longer present in the center of the device.

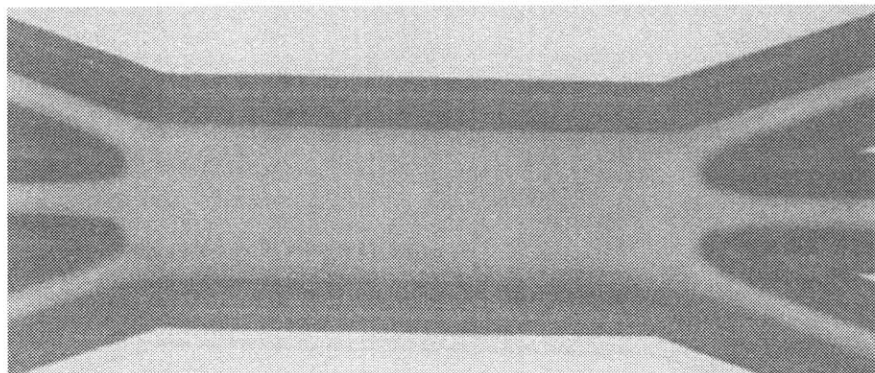


Figure 5.31. $t = 4:54:15$. No further gelling was observed. Peptide solution was no longer present in the device.

This result occurred often. The skin would form beautifully, but the center area either would not form a fully solidified gel or would not take on Congo Red dye. Images from a different experiment (July 24, 2001, trial 4) are shown in Figure 5.32.

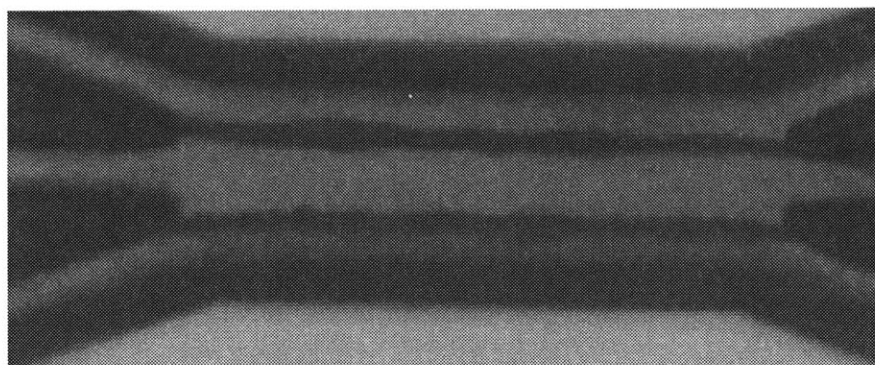


Figure 5.32. $t = 0:15$ from July 24, 2001, trial 4. The peptide solution formed a dark gel on the surfaces of the peptide stream that were exposed to saline.

For this trial, the pumps were stopped at $t = 0:20$ without a gradual flow rate reduction. At 3:13 the peptide gel skins appeared to be translucent and stained with Congo Red, although a break appeared in the lower right of the figure and peptide was leaking into one of the saline outlet channels (Figure 5.33).

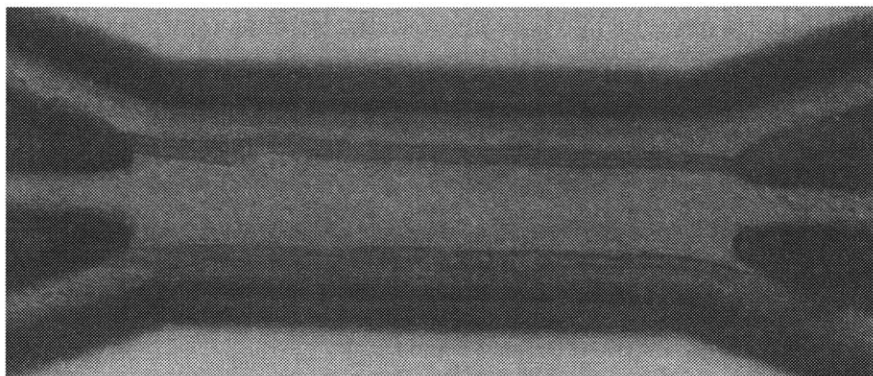


Figure 5.33. $t = 3:13$ from July 24, 2001, trial 4. The dark gel appeared to wash away, leaving thin, transparent Congo Red-stained gel 'skins.' The 'skins' seemed to be a barrier to fluorescein.

By $t = 4:24$, fluorescein had infiltrated the entire converged-channel region and the gel structure was nearly invisible (Figure 5.34).

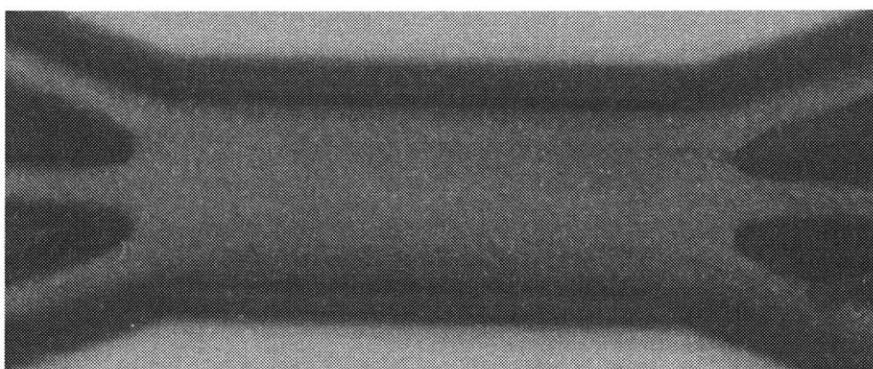


Figure 5.34. $t = 4:24$ from July 24, 2001, trial 4. The gel structure was nearly invisible.

These results indicated that peptide solution was no longer present in the device. Peptide solution was certainly present in the center of the device at $t = 0$. Although compliance in the system was minimized, there was evidently still significant compliance since flow continued after the pumps had been stopped (small particles could be observed flowing through the device on the video capture setup). One hypothesis is that compliance upstream in the center inlet path caused water to flow into the device and displaced peptide solution from the center stream region (Figure 5.35). This problem was addressed by filling the plugged fluid path (between the point where the small-bore fitting meets the silicon-glass device, through the large-bore fluid fitting, to

the plug) with peptide solution before running the experiment. However, there may be hidden compliance contributors (air bubbles) in the large-bore metal fluidic fitting.

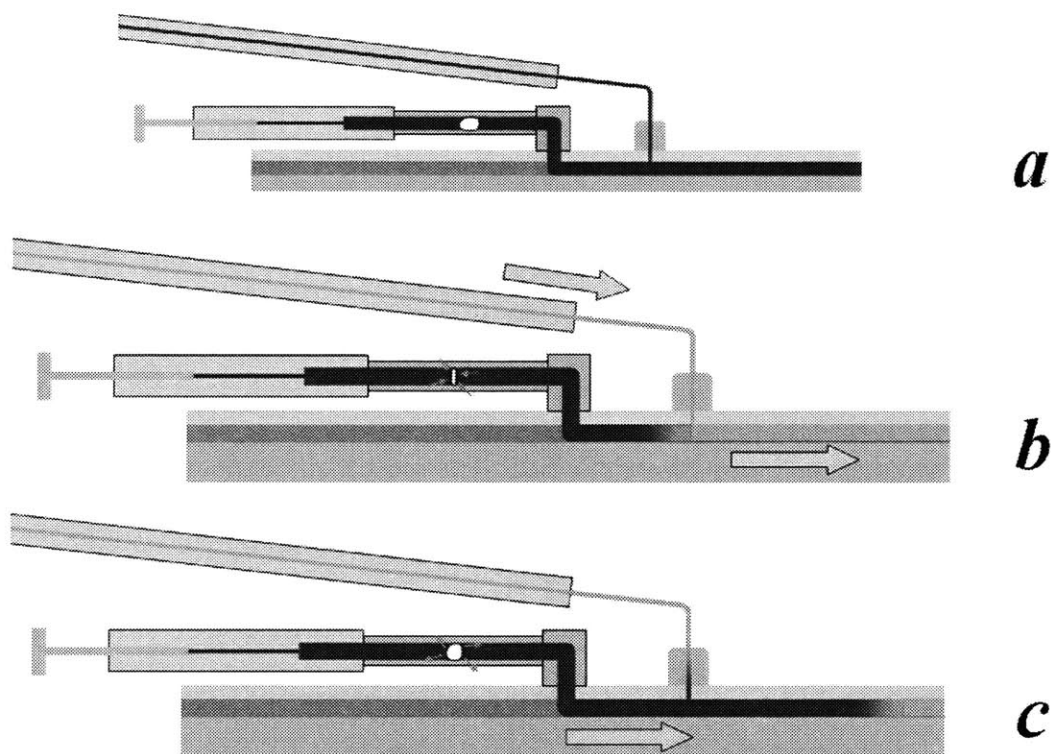


Figure 5.35. (a) Air bubbles may be hidden in the stainless steel large-bore tubing of a plugged inlet. (b) As fluid is pumped through the small-bore inlet, the pressure caused by resistance in the device causes the air bubble to contract. (c) When the pump is stopped, the air bubble expands, driving fluid through the device.

A consistent observation in these experiments is that the peptide appears to form a thin gel at both edges of the solution stream, then ceases to grow any thicker. A potential hypothesis is that peptide filaments may be nucleating at the edges of the peptide stream, as previously proposed (see Section 5.1.4). If this causes a reduction in peptide concentration in the core of the central channel, concentration there may fall below the minimum required for stable gel formation. This seems unlikely, however, since new, full-concentration peptide solution is constantly being supplied, due to flows that persist even when the pump is stopped as a consequence of upstream compliance. If the rate of peptide flow is high, it could be reasoned that the peptide solution might flow at a rate that prevents the formation of a stable gel. As the

peptide solution gels, it may be prevented from adhering to the established gel by shear stress. The presence of a skin may act as a barrier to diffusion and limit the rate of salt diffusion into the central flow, further slowing gelation. While a gel skin was initially able to form at flow rates that were likely higher, the saline concentration may be lower due to the skin. At this lower concentration, there could be a critical value, either of shear stress or flow velocity, which prevents gelation. To decisively confirm or rule out these hypotheses requires a reliable and quick method of stopping flow in the device.

Results from Micro Experiment Design I- μ suggested that peptide continued to flow through the system after the pumps were stopped. The most likely explanation for this is that the compliance of the system remained high, due to either remaining compliance in the tubing, or the presence of air bubbles in the system, despite purging efforts. In the next system, Micro Experiment Design II- μ , further refinements were incorporated to stop flow quickly.

5.4 Micro Experiment Design II- μ

Micro Experiment Design II- μ incorporated pressure-release fixtures at the peptide syringe and the two saline syringes (Figure 5.36).

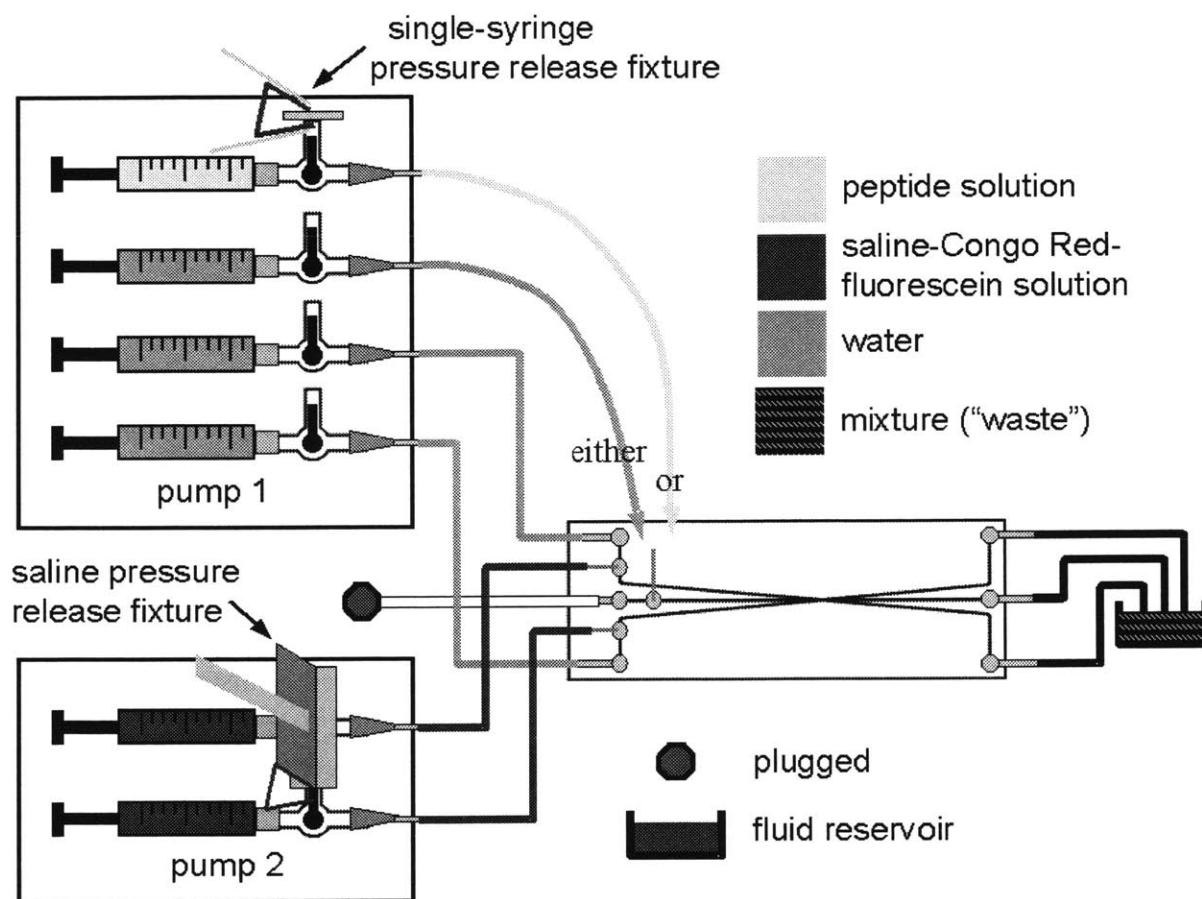


Figure 5.36. Schematic of the setup for the micron-scale membrane forming experiment designated Micro Experiment Design II- μ

The pressure release fixtures were designed to allow manual opening of all three inlet channels to atmospheric pressure at once (see Appendix A5.4 for the fixture designs). If the outlets are already held at near-atmospheric pressure, opening the inlets to the atmosphere should make the pressure difference across the device equal to zero and instantaneously stop all flow. Compliance in the tubing should relax and drive fluid to the outlet through the pathway of lowest resistance, away from the device rather than through it. The protocol is outlined below.

5.4.1 Prepare Experiment, Confirm Equal Resistance

- Saline solution is prepared (0.15 M NaCl, 0.01 M fluorescein salt, 0.05 mg/ml Congo Red). The saline solution is measured into small vials and varying amounts of 72 kDa Dextran are added to the different samples (from 0.0 to 20.0 weight percent). The peptide is prepared and incubated. The viscosity of the peptide and each saline solution is determined using the previously developed method (see Section 5.2). Saline-fluorescein-Congo Red-Dextran solution is selected with a viscosity that is close to that of the peptide solution.
- The entire device is filled with water, and air bubbles are removed.
- Fluidic connections are made as shown above (Figure 5.36), using small-bore Teflon[™] tubing (see Section 3.4 for specifications).
- Saline-fluorescein-Congo Red-Dextran solution is infused through the small-bore side inlets (S_S 's) while water is infused through the small-bore center inlet (C_S). Observation of laminar, symmetric flow confirms that the outlet channels are clear of obstruction.
- Water is flowed through the small-bore center inlet (C_S) and the large-bore side inlets (S_L 's) to flush saline from the device. Saline solution should fill the fluidic path up to the fluid fitting-glass interface (see Figure 5.25).

5.4.2 Infuse Peptide

The tubing from the center small-bore water syringe is detached from the device at the small-bore fluidic fitting, and the syringe containing the peptide syringe is attached. The syringe is attached to a plastic stopcock, to which the single-syringe pressure release fixture is mounted. Peptide is infused through the center channel (through C_S) while water is flowed through the side channels (S_L 's) (see Figure 5.26). Approximately 15 μ l from each peptide and water syringe is

pumped to ensure that full-concentration peptide solution is flowing across the converged-channel region.

5.4.3 Infuse Saline, Begin Gelation

The peptide and water flow rates that give the desired peptide stream width are calculated based on the viscosities of the peptide solution and the saline-fluorescein-Congo Red-Dextran solution. The syringe pumps are set to these flow rates and pumping is started. As soon as saline-fluorescein-Congo Red solution is visible in the device, the video recording apparatus is started and time is reset to $t = 0$.

5.4.4 Stop Flow, Continue Gelation

Once thin gel “skins” are observed flanking the center peptide stream, the syringe pumps are stopped and the pressure is released by using the simultaneous pressure release fixtures, causing flow in the device to stop immediately. If pressure differences across the center stream are controlled or eliminated (see Section 6.2.1), the gel skins will remain intact and confine the peptide solution to the center of converged area. It is expected that the porous gel skins will allow salt ions to diffuse into the peptide solution, resulting in a completely gelled membrane between the two side channels.

5.5 Summary

While the processes that comprise the Micro Experiment Design II- μ gel forming protocol have been developed, the protocol was not completely executed and proven effective due to device cost and non-optimal geometry (see Section 6.1). Early large-scale gel forming

experiments proved the feasibility of the membrane-forming concept. Procedures were developed to use the micron-scale device in concert with the analytic solution for flow to perform viscosity measurements. Attempts to form a gel membrane at the micron-scale have produced promising precursors. Further understanding of the gelation process will help achieve the goal of a full width gel membrane. In the next chapter, improvements to the device design and experimental setup are proposed to successfully fabricate a stable thin peptide gel membrane. Procedures for testing the gel and the modifications necessary for cell culture are outlined.

Chapter 6

Recommendations for Further Development of the Capillary-Parenchymal Element (CPE) Bioreactor

While attempts to form a micron-scale membrane were unsuccessful, the micron-scale gel-forming experiments yielded positive results and set a strong foundation for the future success of the project. At the same time, improvement of several areas of the experimental design can be formulated in the pursuit of successful gel-membrane formation. Membrane formation would be aided as well by further understanding the peptide gelation process. Once a membrane is successfully fabricated, the device can be used to test the transport and mechanical properties of the oligopeptide gel. Development of the cell-culture capabilities of the device will require further complexity of the device geometry and surface chemistry, as well as additional protocol and experiment design and refinement. The concepts presented here are ideas and outlines, rather than in-depth studies, for future development of the device.

6.1 Improvements for Successful Membrane Formation: Processes and Materials

6.1.1 Mask Selection

Serious drawbacks of the glass-silicon paradigm include the time and cost required to produce the devices. Photomasks must be designed then sent out to be manufactured, with a turnaround time of days; the silicon and glass wafers must be processed in a clean room environment, using costly and hazardous chemicals; the glass wafers must be drilled in the

machine shop and bead blasted; the wafers must be cleaned, bonded, and diced; fluidic fittings must be precision-machined and epoxied to the devices; then, when the devices are finally used in fluidic studies, they risk becoming permanently clogged and unusable. The devices can end up costing hundreds of dollars each, and the cost of the photomasks for silicon use can be prohibitive to multiple design revisions; in this study, only one glass photomask for silicon wafer patterning was manufactured.

One way to reduce the cost of design revisions is to use Mylar photomasks patterned with a high-resolution laser printer. The turnaround time for this process is, at most, on the order of hours. The cost of these masks is much lower than for glass masks; however, glass masks are capable of much higher patterning resolution. While they may not be suitable for patterning geometry with cell- and capillary-scale features, Mylar masks can be very useful for fast and inexpensive design revisions. Ideas could be tested, refined, and proven on a larger scale (less than millimeters, larger than single micrometers); a glass mask would then be made for fabricating the cell-scale device.

6.1.2 Material Selection

Another factor contributing to the high-cost of device fabrication is the processing involved. One alternative to the silicon-glass paradigm is to use cast polymer devices that can be made cheaply and quickly and do not require a clean room environment [20]. The main drawback of cast polymer fluidic devices is that they are inherently more compliant than glass-silicon devices (as mentioned Section 2.2). Despite the many efforts to reduce this effect in our experiments, compliance was a problem due to the high pressures caused by high resistances in the devices. By revising key aspects of the device geometry (see Section 6.2.1), resistance can be

drastically reduced, and therefore pressure, so that a highly compliant device will exhibit little channel-volume change under flow conditions. As with the photomask, cast polymer devices can be used for fast, inexpensive design prototypes and revisions, and final versions can be fabricated from silicon and glass.

6.2 Improvements for Successful Membrane Formation: Geometry Design

6.2.1 Resistance Reduction

A simple means to drastically lower the resistance in the devices while retaining the designed converged-channel device area geometries is to widen and deepen the channels a short distance away from the channel convergence and divergence (Figure 6.1).

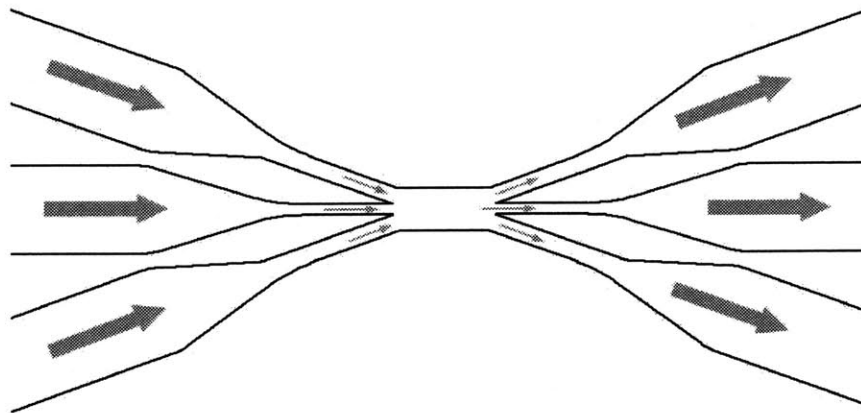


Figure 6.1. Inlet and outlet channels become deeper and wider away from the converged-channel device area.

Using an additional mask to either twice-etch specific areas of a silicon wafer or to deposit additional layers SU-8 epoxy resin (capable of pattern thickness of 10 to 1000 μm , MicroChem Corporation, Newton, MA) for polymer casting, channels of multiple depths can be made. The resistance for a device with the device area geometry of Fc1 (see Table 2.3), but with inlet and outlet channels of varying widths and depths, can be calculated (Figure 6.2). Increasing the width and depth of the inlet and outlet channels results in an extreme reduction in resistance-

caused pressure. Pressures required to drive the fluids can be lowered to the same scale of the membrane-fracturing pressures, a further significant benefit of the redesign.

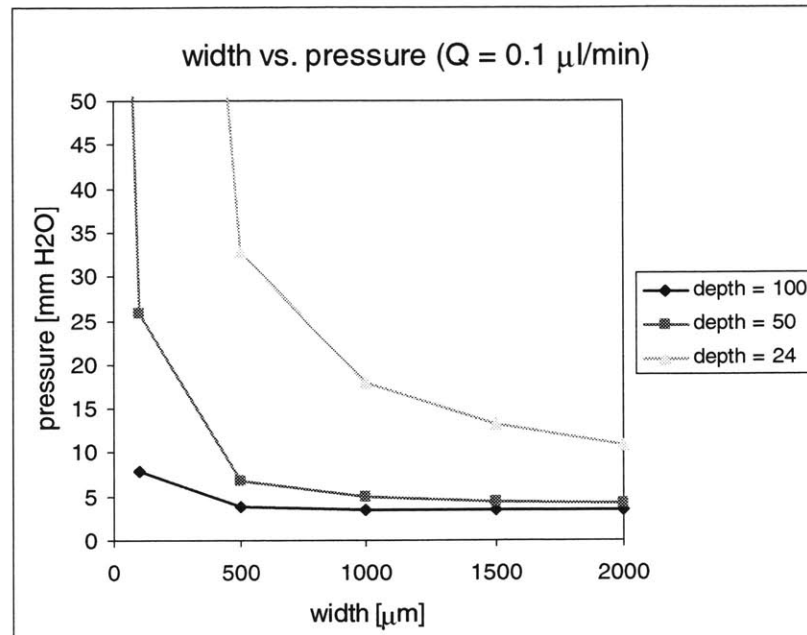


Figure 6.2. A plot of pressure versus width for various channel depths. The smallest pressure for inlet and outlet channels calculated here was 3.44 mm H₂O for 2000x100 μm channels.

The small-bore fittings must interface with the device over the narrowed channel to prevent the fluids from possibly mixing and becoming diluted in a wide channel (Figure 6.3).

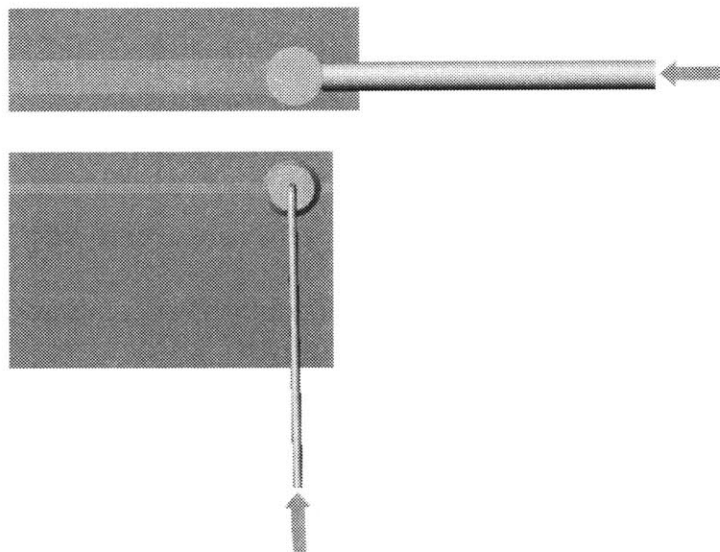


Figure 6.3. A wider channel (*top*) results in a larger volume of diluted solution due to diffusion.

6.2.2 Center Channel Dimension

A persistent problem in the micron-scale experiments was that the peptide solution gels as predicted at the saline interface, but does not gel further (Figure 6.4).

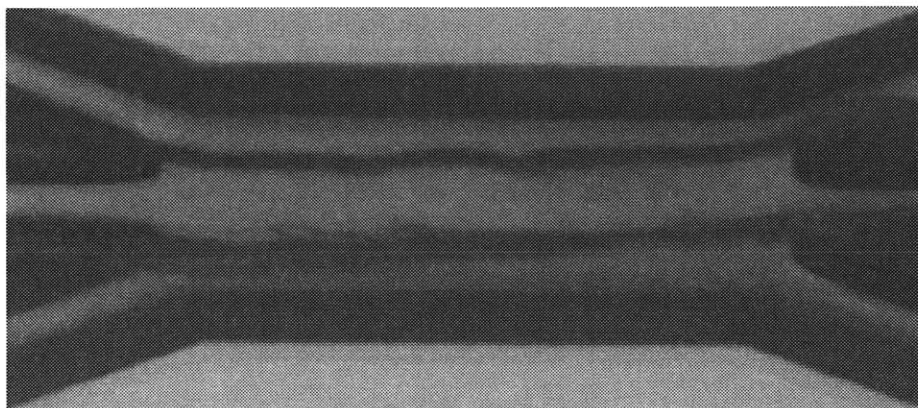


Figure 6.4. The edges of the peptide stream have gelled, but the center appears to be a fluid.

One way to avoid this problem is to make the peptide stream narrower so that the initial gelling pattern spans the entire peptide stream. The flow conditions must be either of the following: the peptide flow must be stopped as soon as gelling begins, as the gel would block and disrupt the peptide stream; or, the peptide flow must be stopped before saline reaches the converged-channel device area, prior to gelation. The inlet and outlet channel resistances can be reduced, as detailed above, so that pressures across the membrane can be controlled and kept below the fracture pressures for these thinner membranes. The experiment was modeled and solved numerically for center inlet and outlet channels of half and quarter widths of Fc1 (see Table 2.3) dimensions (channels of width 24-12-24 microns and 24-6-24 microns).

6.2.2.1 Numerical Results for a 24-12-24 Device

For this device geometry, the inlet and outlet channels are designed so that their resistances are equal for a saline solution viscosity equal to that of the peptide ($\mu_{\text{saline}} = \mu_{\text{peptide}}$).

These parameters give very smooth flow profiles in the converged-channel device area for the flow rate ratio $Q_{\text{saline}}:Q_{\text{peptide}} = 1.38:1$ (Figure 6.5 and Figure 6.6).

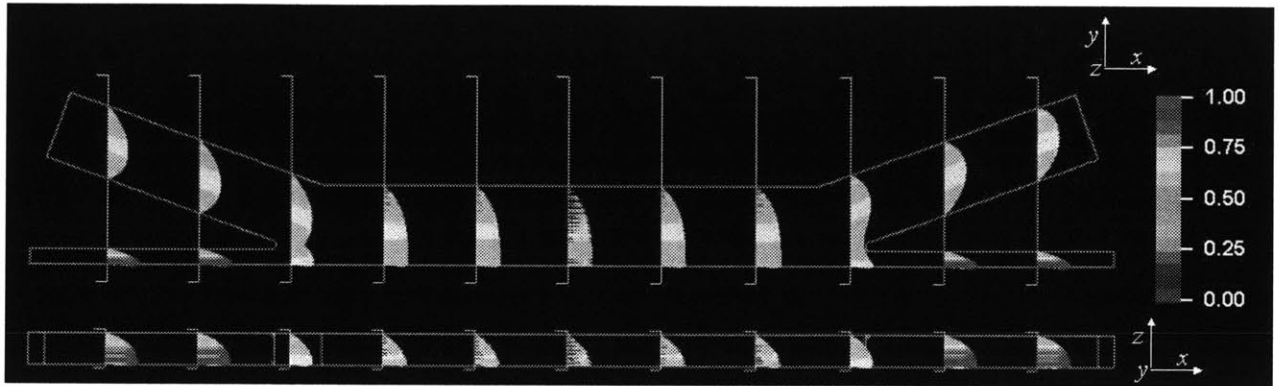


Figure 6.5. A vector plot of the velocity profile for channel widths 24-12-24 μm , $\mu_{\text{saline}}:\mu_{\text{peptide}} = 1:1$, and $Q_{\text{saline}}:Q_{\text{peptide}} = 1.38:1$

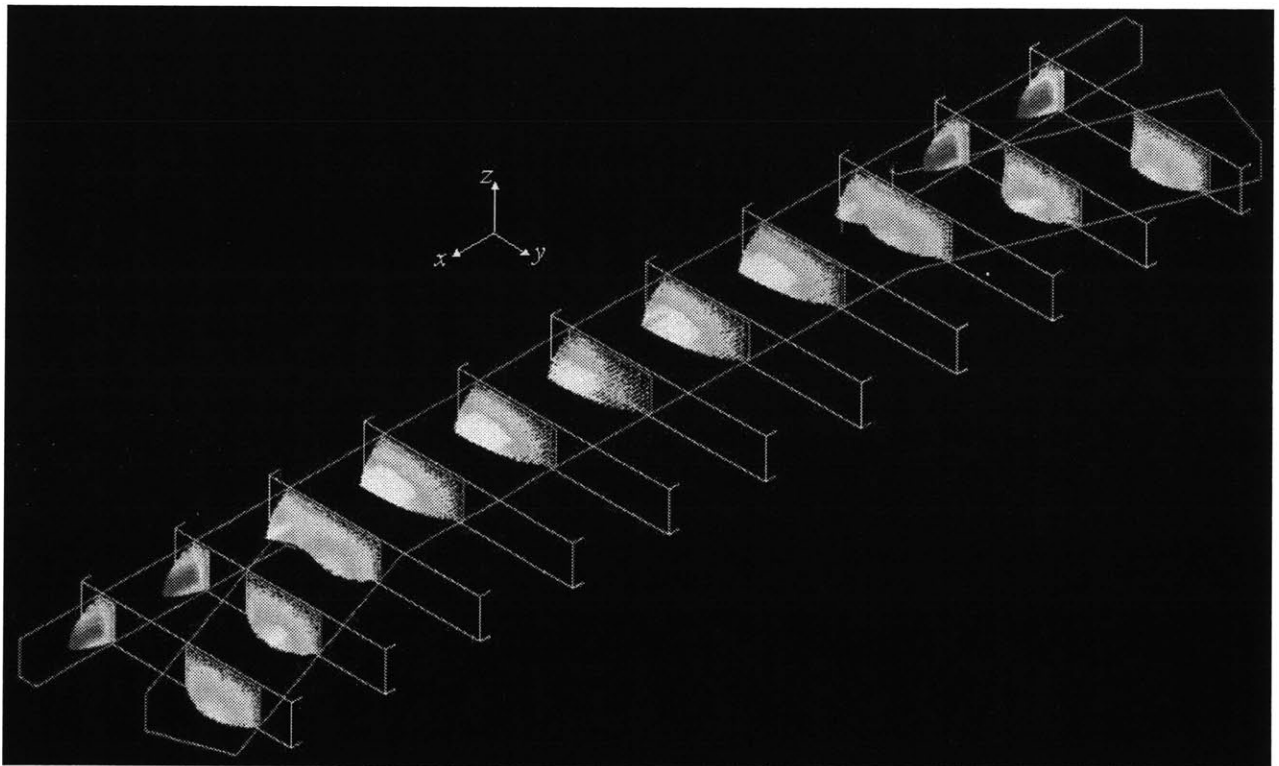


Figure 6.6. An isometric vector plot of velocity profile for channel widths 24-12-24 μm , $\mu_{\text{saline}}:\mu_{\text{peptide}} = 1:1$, and $Q_{\text{saline}}:Q_{\text{peptide}} = 1.38:1$

The salt concentration profile for these parameters shows high concentrations reaching the center of the peptide stream close to the initial channel convergence (Figure 6.7).

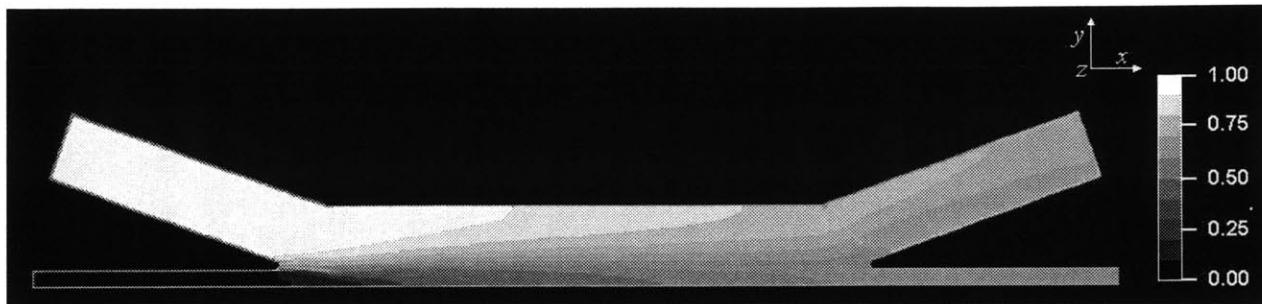


Figure 6.7. A band plot of the concentration profile of saline for a device with channel widths 24-12-24 μm

6.2.2.2 Numerical Results for a 24-6-24 Device

The peptide solution stream can be narrowed further by reducing the width of the center inlet and outlet channels to 6 microns wide (these are the converged-channel device area dimensions of device Fc4, see Table 2.3). Velocity vector plots for the flow rate ratio $Q_{\text{saline}}:Q_{\text{peptide}} = 2.59:1$ are shown in (Figure 6.8 and Figure 6.9).

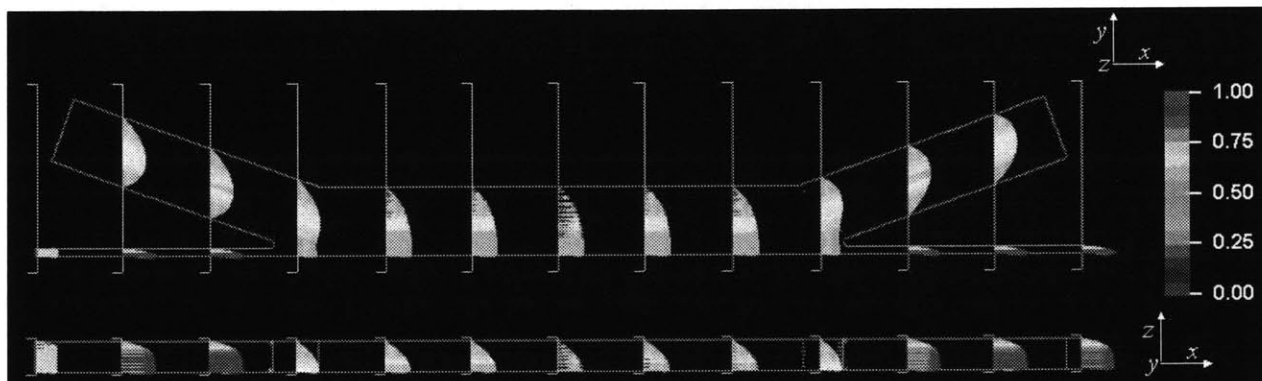


Figure 6.8. A vector plot of the velocity profile for channel widths 24-6-24 μm , $\mu_{\text{saline}}:\mu_{\text{peptide}} = 1:1$, and $Q_{\text{saline}}:Q_{\text{peptide}} = 2.59:1$

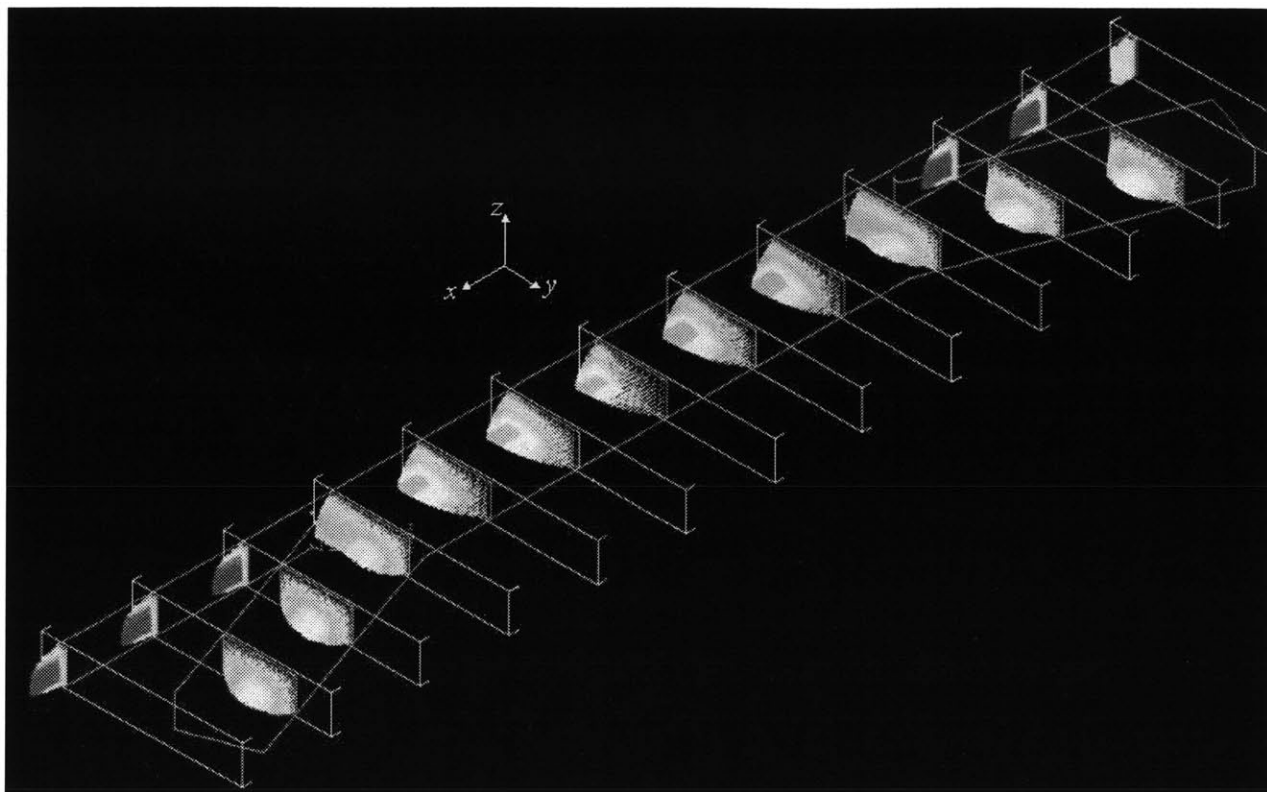


Figure 6.9. An isometric vector plot of the velocity profile for channel widths 24-6-24 μm , $\mu_{\text{saline}}:\mu_{\text{peptide}} = 1:1$, and $Q_{\text{saline}}:Q_{\text{peptide}} = 2.59:1$

The narrower peptide stream width greatly decreases the length of the low-salt region in the converged peptide stream (Figure 6.10).

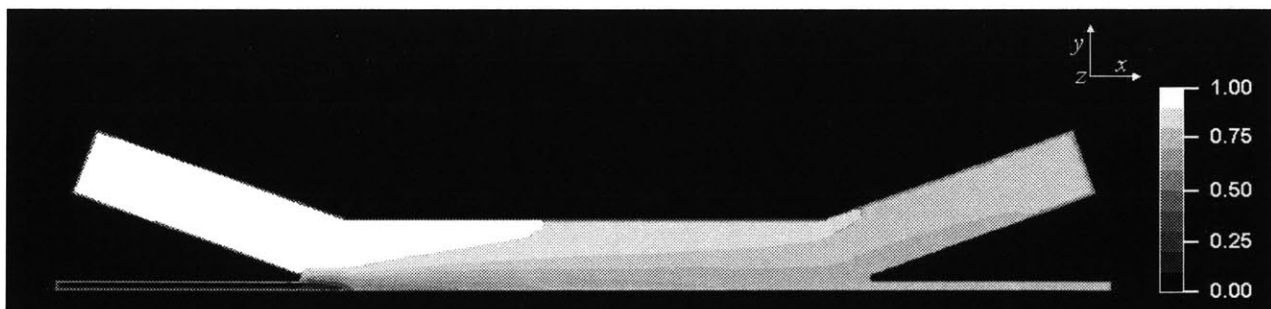


Figure 6.10. A band plot of the concentration profile of saline for a device with channel widths 24-6-24 μm

Modeling these different geometries is useful for designing future channel geometries. In the fabricated device (24-24-24 μm wide channels), factors in addition to distance may be hindering full salt diffusion and gel formation. Even without addressing these problems,

narrowing the peptide solution stream will certainly reduce the time required for full gelling, and will also produce a membrane closer in width to the physiologic gap between liver and capillary cells (the Space of Disse, see Figure 1.2).

6.3 Investigating the Nature of Gel Formation

Simply narrowing the center peptide stream to produce a completely gelled membrane avoids addressing the reasons why the center of the peptide stream did not gel in the micron-scale experiments, or why there appears to have been a peptide gel gradient in the macro-scale experiment. Further experimentation to understand the nature of peptide gel formation is needed to elucidate the causes of this behavior.

6.4 Testing the Gel

Once a micron-scale gel membrane has been successfully fabricated between the two channels, a chemical or pressure gradient can be imposed across the membrane to investigate its conductivity and mechanical properties. Conductivity of the gel can be measured by flowing a fluorescent dye of known diffusivity and molecular size in solution through one channel, and water on the other side. Flow is stopped in both channels, then the change in concentration density as the dye diffuses through the peptide gel and into the water-filled channel is observed by measuring the intensity of fluorescence over time (Figure 6.11).

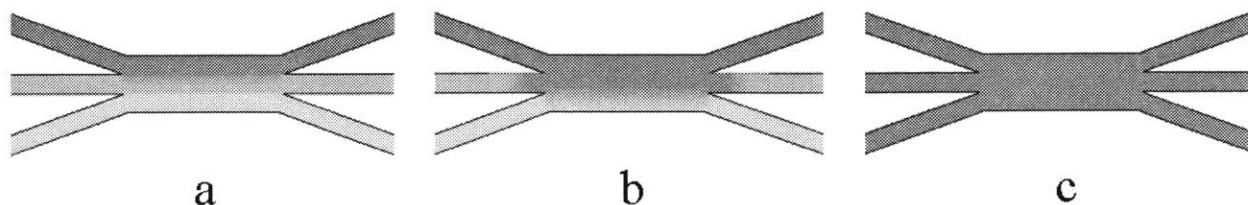


Figure 6.11. (a) Dye of known diffusivity and molecular size is flowed into one channel, water in the other. Flow is stopped in both channels, and the change in concentration density as (b) the dye diffuses through the peptide gel and (c) into the water-filled channel is observed by measuring the intensity of fluorescence over time.

Alternatively, a pressure gradient across the membrane can be used to measure the conductivity of the membrane. A pressure gradient can be set up using fluid reservoirs containing different heights of water. The water level in these reservoirs can be measured over time to monitor the flow rate through the membrane versus pressure across the channels (Figure 6.12).

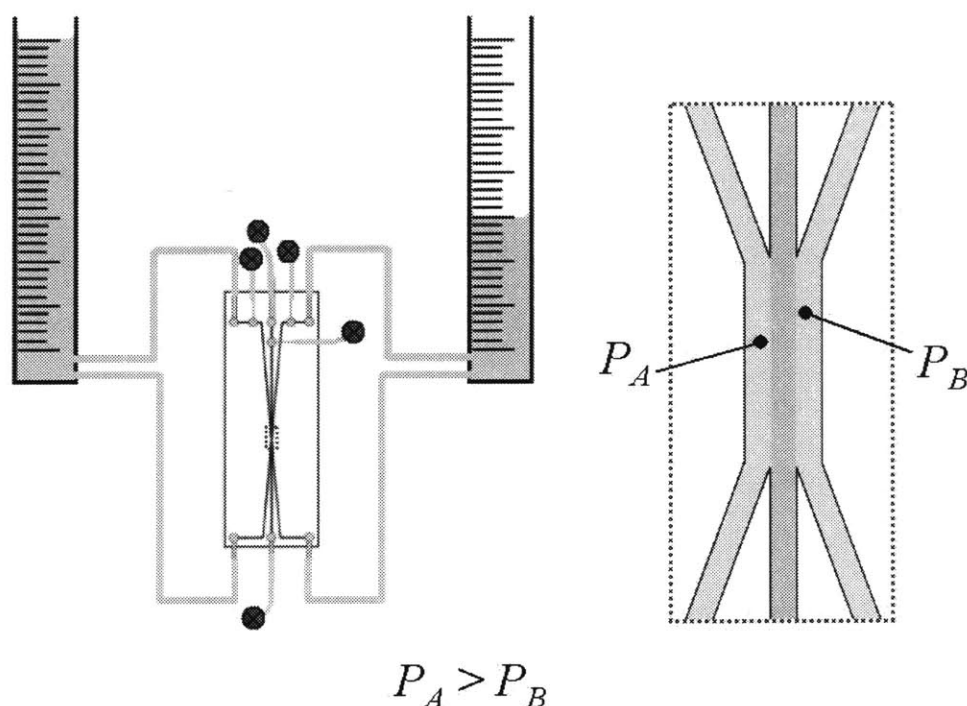


Figure 6.12. A pressure gradient is set up across the membrane. The red box is a detail view of the converged-channel area.

This setup can also be used to measure the fracture strength of the gel by increasing the pressure gradient across the membrane until rupture (or a sudden increase in conductivity) is observed.

6.5 Cell Culture

6.5.1 Surface Chemistry Modification

The device geometry requires that cells be dynamically seeded. It will be necessary to control where the cells will adhere and grow. If hepatocytes adhere to areas outside of the converged-channel region, they will essentially be in homotypic cell-culture. Their viability will be impeded; as they undergo apoptosis, they may release toxins into the cell culture medium that will negatively affect cells in the co-culture region. Areas that either promote or resist cell-adhesion can be created through modification of surface chemistry. Techniques for surface modification in specific areas on silicon and glass have been developed extensively in the literature [3,10,20]. These techniques can be employed to promote cell attachment in the converged-channel device area, while making the inlet and outlet channel surfaces resistant to cell adhesion (Figure 6.13).

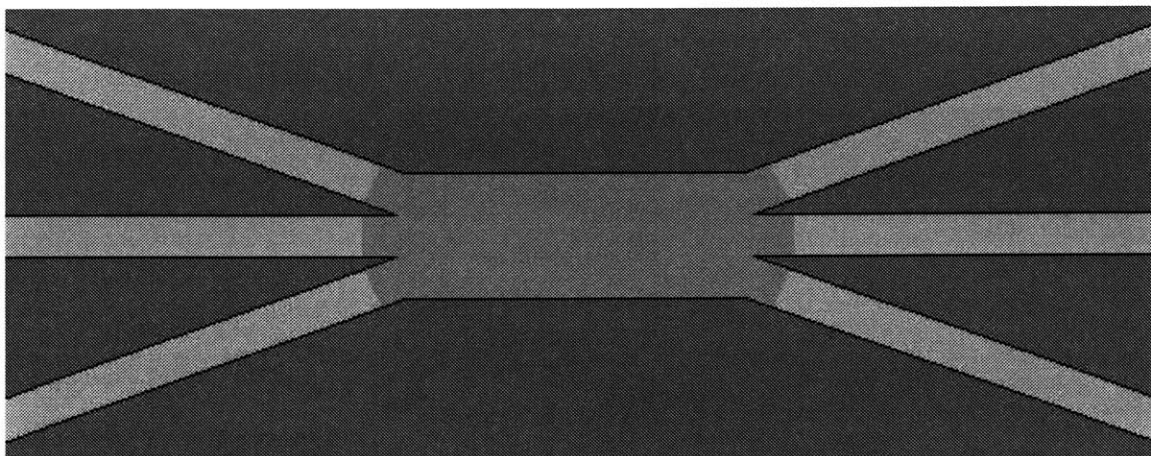


Figure 6.13. Top view of the converged-channel area. The co-culture area (green) can be treated to be “sticky” to cells. The light gray areas can be treated to resist cell adhesion.

6.5.2 Geometry Modification

In the process of dynamic seeding, the use of surface chemistry to keep cells from settling in the inlet and outlet channels may not be entirely reliable. A more complicated flow-channel

network can implemented to introduce cells into the co-culture area, then flush them from the inlet and outlet channels (Figure 6.14).

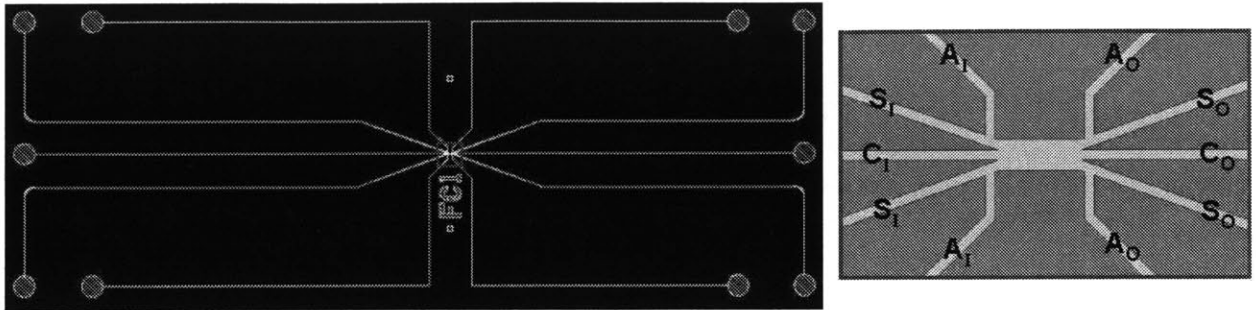


Figure 6.14. Revised FC1 showing new fluidic paths (*left*). Detail of converged-channel area (*right*), fluid paths are labeled: the current-design center and side inlets, C_1 and S_1 's; the current-design center and side outlets, C_0 and S_0 's; the new auxiliary inlets and outlets, A_1 's and A_0 's.

The new channels (auxiliary channels A_1 's and A_0 's) are filled with water. If water is assumed to be an incompressible fluid, these channels, if filled and plugged, will not affect the gel formation process. Once the gel is formed, cells will be flowed through the device in suspension, then allowed to settle and adhere to the channels (in through the S_1 's and out through the S_0 's) (Figure 6.15).

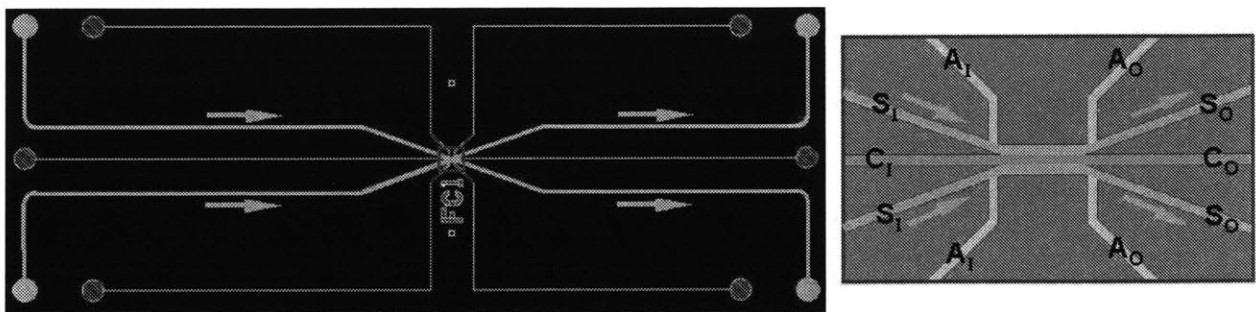


Figure 6.15. Cells are flowed into the device in suspension; they are flowed in through the S_1 's and out through S_0 's.

Culture medium is then flowed through the A_1 's and out the S_1 's to flush cells from the inlet channels. The process is repeated, flowing culture medium through the A_0 's and out the S_0 's, to flush cells from the outlet channels as well (Figure 6.16). This procedure should be performed

carefully to leave the gel membrane intact and the channel surfaces in the converged-channel device area coated with cell–adhesion molecules.

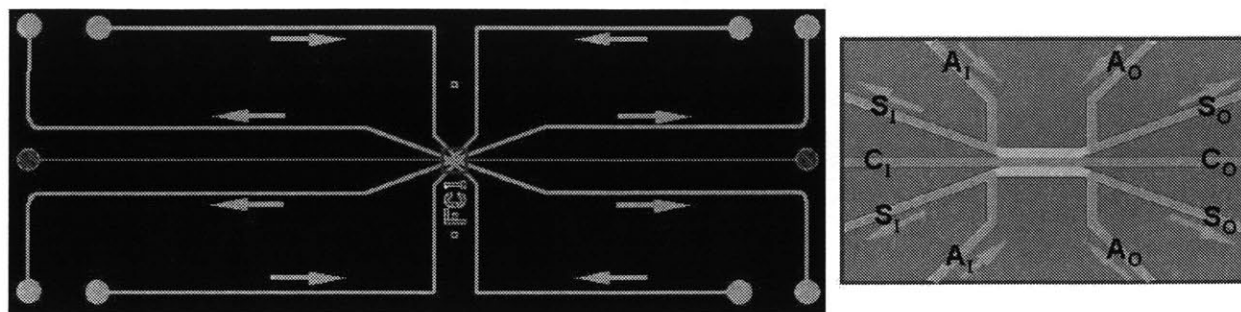


Figure 6.16. Cells are flushed from the inlet and outlet channels; fluid is flowed in through the A_1 's and A_0 's, and out through the S_1 's and S_0 's.

6.6 Summary

In this study, techniques for gel membrane formation in the device have been developed. Efforts to form a gel membrane can be assisted by improvements to the device geometry. At the cost of resolution, different mask and device materials can allow design and fabrication revisions of the device design at much lower costs and more quickly than with high-resolution silicon photolithography. Specific revisions can be made to the device geometry to reduce the high pressures incurred by long, narrow channels. Design of the membrane-forming experiments can be aided by general investigation into the nature of peptide gelation. Once a membrane is successfully formed in the device, properties of the gel can be probed with the use of chemical and pressure gradients. To utilize the device as a bioreactor for co-culture of parenchymal and mesenchymal cells, the geometry will require further modification, and a protocol must be developed to seed and culture the cells.

This page intentionally let blank.

Chapter 7

Summary and Conclusions

7.1 Summary of the Work

A novel bioreactor was designed to co-culture endothelial and hepatic parenchymal cells in an environment that mimics the *in vivo* characteristics of a single capillary and the adjacent hepatocytes in the liver. The device incorporates a membrane made of a self-assembling oligopeptide that forms a hydrogel matrix when exposed to specific chemical conditions. Analytic and numerical modeling techniques were used to investigate the fluid flow and mass transfer characteristics and aid in design of the bioreactor. The experimental setup incorporated precision flow control instrumentation, reflectance and fluorescence microscopy, and digital image acquisition hardware. Membrane-forming experiments produced promising precursors to a gel membrane, and guided refinement and improvement of the device and experiment design.

7.2 Results

In the course of this study, computational models were developed to predict flow and optimize membrane formation in the device. These models required investigation of unknown physical properties of the peptide in solution. Proof of concept was successfully demonstrated in a large-scale device (channel widths on the order of millimeters instead of micrometers). Results from experimentation with the micrometer-scale devices contributed to the development of the membrane-forming protocols.

Analytic and numerical models were developed to study fluid flow and mass transfer during the fabrication of the membrane. The mass transfer model enabled prediction of the initial gelation pattern. The solution to the Navier-Stokes equation for fully-developed uniaxial flow and the three-dimensional finite element models of fluid flow revealed the velocity field that results from flows consisting of two fluids with different viscosities.

The properties of the peptide were investigated to optimize the flow parameters. The diffusivity of the peptide was approximated using structural data and the molecular volume of an average peptide filament. The viscosity of the peptide was determined through rheometry and flow experiments; techniques were developed to quickly measure fluid viscosities using very small sample volumes.

Large-scale experiments proved the feasibility of the membrane-forming concept by formation of a millimeter-scale oligopeptide gel membrane. At the micron-scale, a stable, fully gelled membrane was not successfully fabricated. However, promising precursors were demonstrated, and a protocol was proposed but not executed, due to device cost and non-optimal geometry.

7.3 Recommendations for Further Work

Recommendations for further work were proposed to address the factors that prevented success in the membrane-forming experiments. Further improvements to the device materials and geometry were outlined to eliminate these factors. A number of issues arose in the membrane-formation experiments, most notably the non-uniform gelling behavior exhibited by the peptide. Future investigation into the nature of peptide gelation will elucidate these results, and will help in designing experiments for successful membrane formation. Once membrane

formation is achieved and refined, the device can be utilized to measure the conductivity and mechanical properties of the gel. To co-culture cells in the device, the surface chemistry and geometry will require further modification. Finally, it is our hope that studies of co-cultured cells in the completed device will contribute to the field of tissue engineering. Similar methods can be adapted to tissues other than the liver, or scaled-up to grow vascularized tissue *in vitro*, to aid in the eventual development of engineered replacement organs.

This page intentionally left blank.

References

- [1] I.M. Arias, H. Popper, D. Schachter, D.A. Shafritz, The Liver: Biology and Pathobiology, Raven Press, New York, 1982, p.xxiv, xxix.
- [2] S. Bhatia, Microfabrication in Tissue Engineering and Bioartificial organs, Kluwer Academic Publishers, Boston, MA, 1999, pp.13-15.
- [3] S. Bhatia, Microfabrication in Tissue Engineering and Bioartificial organs, Kluwer Academic Publishers, Boston, MA, 1999.
- [4] S.N. Bhatia, U.J. Balis, M.L. Yarmush, and M. Toner, "Microfabrication of hepatocyte/fibroblast co-cultures: role of homotypic cell interactions," *Biotechnology Progress*, Vol. 14, 1998, pp. 378-387.
- [5] J.T. Borenstein, K.R. King, H. Terai, and J.P. Vacanti, "Capillary formation in microfabricated polymer scaffolds," *Materials Research Society Symposia Proceedings*, Vol. 711, GG1.3, 2002.
- [6] J.L. Campra and T.B. Reynolds, "The Hepatic Circulation," The Liver: Biology and Pathobiology, Raven Press, New York, 1982, pp.627-645.
- [7] M.R. Caplan, P.N. Moore, S. Zhang, R.D. Kamm, and D.A. Lauffenburger, "Self-Assembly of a β -Sheet Protein Governed by Relief of Electrostatic Repulsion Relative to van der Waals Attraction," *Biomacromolecules*, Vol.1, No.4, 2000, pp.627-631.
- [8] Y. Cohen, Chapter 9: Interfacial Mass Transfer, Environmental Multimedia Transport Phenomena, Multimedia Envirosoft Corporation, LA, CA, [online], URL: http://polysep.ecla.edu/envmm/chapt9_10.pdf
- [9] W.M. Deen, Analysis of Transport Phenomena, Oxford University Press, New York, 1998.
- [10] L.E. Dike, C.S. Chen, M. Mrksich, J. Tien, G.M. Whitesides, and D.E. Ingber, "Geometric control of switching between growth, apoptosis, and differentiation during angiogenesis using micropatterned surfaces," *In vitro cellular & developmental biology – Animal*, Vol. 35, Sept. 1999, pp.441-448.
- [11] S. Erlinger, "Bile Flow," The Liver: Biology and Pathobiology, Raven Press, New York, 1982, pp.407-427.
- [12] L.G. Griffith and Gail Naughton, "Tissue Engineering – Current Challenges and Expanding Opportunities," *Science*, Vol. 295, 2002, pp.1009-1016.

- [13] L.G. Griffith, B. Wu, M.J. Cima, M.J. Powers, B. Chaignaud, and J.P. Vacanti, "In Vitro Organogenesis of Liver Tissue," *Annals of the New York Academy of Sciences*, Vol. 831, Dec. 1999, pp.382-397.
- [14] A.C. Guyton, Textbook of Medical Physiology, 3rd edition, W.B. Saunders Co., Philadelphia, 1968, p.325.
- [15] A.C. Guyton, J.E. Hall, Textbook of Medical Physiology, 10th ed., W.B. Saunders Co., Philadelphia, 2000, p.145.
- [16] A.C. Guyton, Textbook of Medical Physiology, 10th edition, W.B. Saunders Co., Philadelphia, 2000, p.798.
- [17] Harvard Apparatus website, URL: <http://www.harvardbioscience.com>
- [18] T. Holmes, S. de Lacalle, X. Su, G. Liu, A. Rich, and S. Zhang, "Extensive neurite outgrowth and active synapse formation on self-assembling peptide scaffolds," *Proceedings of the National Academy of Sciences of the United States of America*, Vol. 97, June 2000, pp. 6728-6733.
- [19] S. Kaihara, J. Borenstein, R. Koka, S. Lalan, E.R. Ochoa, M. Ravens, H. Pien, B. Cunningham, and J.P. Vacanti, "Silicon Micromachining to Tissue Engineer Branched Vascular Channels for Liver Fabrication," *Tissue Engineering*, Vol. 6, No. 2, 2000, pp. 105-117.
- [20] R.S. Kane, S. Takayama, E. Ostuni, D.E. Ingber, G.M. Whitesides, "Patterning proteins and cells using soft lithography," *Biomaterials*, Vol. 20, 1999, pp.2363-2376.
- [21] E.B. Keefe, "Selection of patients for liver transplantation," Transplantation of the Liver, Appleton and Lange, Norwalk, CT, 1995.
- [22] K.R. King, C.C. Wang, J.T. Borenstein, M. Shin, and J.P. Vacanti, "Biodegradable Polymer Microfluidics for Tissue Engineering Microvasculature," *Materials Research Society Symposia Proceedings*, Vol. 730, U1.4, 2002.
- [23] J. Kisiday, M. Jim, H. Hung, B. Kurz, S. Zhang, A.J. Grodzinsky, "Self-assembling Peptide Scaffold for Cartilage Tissue Engineering," Vol. 26, *San Francisco, California: Transactions of the Orthopedic Research Society*, 2001.
- [24] E.J. Leon, N. Verma, S. Zhang, D.A. Lauffenburger, and R.D. Kamm, "Mechanical properties of a self-assembling oligopeptide matrix," *Journal of Biomaterials Science – Polymer Edition*, Vol. 9, No. 3, 1998, pp. 297-312.
- [25] D.M. Marini, W. Hwang, D.A. Lauffenburger, S. Zhang, R.D. Kamm, "Left-Handed Helical Ribbon Intermediates in the Self-Assembly of a β -Sheet Peptide," *Nano Letters*, Vol. 2, No. 4, 2002, pp. 295-299.

- [26] The Organ Procurement and Transplantation Network, online database, URL: <http://www.optn.org> [cited May 17, 2002]
- [27] T.P. Richardson, M.C. Peters, A.B. Ennett, and D.J. Mooney, "Polymeric System for Dual Growth Factor Delivery," *Nature Biotechnology*, Vol. 19, 2001, p.1029.
- [28] I. Sample, "Organs to order," *New Scientist*, No. 2340, 27 April 2002, pp.4-5.
- [29] J.D. Seader and E.J. Henley, Separation Process Principles, John Wiley & Sons, New York, 1998.
- [30] S.C. Strom, J.R. Chowdhury, and I.B. Fox, "Hepatocyte Transplantation for the Treatment of Clinical Liver Disease," *Seminars in Liver Disease*, Vol. 19, 1999, pp.39-47.
- [31] J. Wanson, R. Mosselmans, A. Brouwer, and D.L. Knook, "Interaction of Adult Rat Hepatocytes and Sinusoidal Cells in Coculture," *Biologie Cellulaire*, Vol. 36, 1979, pp.7-16.
- [32] R.C. Weast, editor-in-chief, CRC Handbook of Chemistry and Physics, 64th ed, CRC Press, Boca Raton, FL, 1983.
- [33] S. Zhang, T.C. Holmes, C.M. DiPersio, R.O. Hynes, X. Su, and A. Rich, "Self-complementary oligopeptide matrices support mammalian cell attachment," *Biomaterials*, Vol. 16, 1995, pp. 1385-1393.
- [34] S. Zhang, T.C. Holmes, C. Lockshin, and A. Rich, "Spontaneous assembly of self-complementary oligopeptide to form a stable macroscopic membrane," *Proceedings of the National Academy of Sciences of the United States of America*, Vol. 90, April 1993, pp. 3334-3338.

This page intentionally left blank.

Appendix

A2.1 Shear Stress on the Membrane

The Navier-Stokes equation was solved for laminar, viscous fluid flow in a rectangular channel.

The Navier-Stokes equation is

$$\rho \frac{DV}{Dt} = \rho g - \nabla P + \mu \nabla^2 V \quad (\text{A2.1})$$

where V is the fluid velocity vector. For rectangular coordinates, the x -component of the Navier-Stokes equation is

$$\frac{\partial u}{\partial t} + u \frac{\partial u}{\partial x} + v \frac{\partial u}{\partial y} + w \frac{\partial u}{\partial z} = -\frac{1}{\rho} \frac{\partial p}{\partial x} + \frac{\mu}{\rho} \left(\frac{\partial^2 u}{\partial x^2} + \frac{\partial^2 u}{\partial y^2} + \frac{\partial^2 u}{\partial z^2} \right) \quad (\text{A2.2})$$

where u is flow in the x -direction, v is flow in the y -direction, and w is flow in the z -direction.

At steady state,

$$\frac{\partial u}{\partial t} = 0 \quad (\text{A2.3})$$

and since the flow is solely in the x -direction

$$v = 0 \quad (\text{A2.4})$$

$$w = 0 \quad (\text{A2.5})$$

Ignoring the short entrance and exit regions, the flow is fully-developed, so that:

$$\frac{\partial u}{\partial x} = 0 \quad (\text{A2.6})$$

$$\frac{\partial^2 u}{\partial x^2} = 0 \quad (\text{A2.7})$$

u is a function of y and z , $u = u(y, z)$.

Assuming dp/dx is constant over the channel, the Navier-Stokes equation then simplifies to:

$$\frac{\partial p}{\partial x} = \mu \left(\frac{\partial^2 u}{\partial y^2} + \frac{\partial^2 u}{\partial z^2} \right) \quad (\text{A2.8})$$

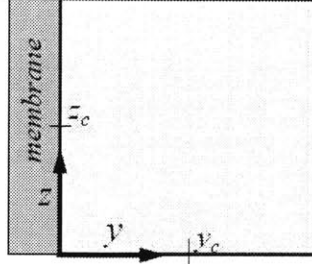


Figure A2.1. Cross-section of the channel, showing the side of the channel adjacent to the membrane

The boundary conditions are (see Figure A2.1):

No flow at the walls

$$u(0, z) = 0 \quad (\text{A2.9})$$

$$u(y, 0) = 0 \quad (\text{A2.10})$$

The velocity gradient is zero at the centerlines

$$\frac{\partial u}{\partial z}(y, z_c) = 0 \quad (\text{A2.11})$$

$$\frac{\partial u}{\partial y}(y_c, z) = 0 \quad (\text{A2.12})$$

The series solution to this problem is found using the Finite Fourier Transform method [9]:

$$u(y, z) = \sum_{n=1}^{\infty} u_n(y) \Phi_n(z) \quad (\text{A2.13})$$

where

$$\Phi_n(z) = \sqrt{\frac{2}{z_c}} \sin\left(n + \frac{1}{2}\right) \frac{\pi z}{z_c}, \quad n = 0, 1, 2, \dots \quad (\text{A2.14})$$

$$u_n(y) = [k_1 \sinh \lambda y + k_2 \cosh \lambda y + C_n] \quad (\text{A2.15})$$

$$u(y, z) = \sum_{n=1}^{\infty} u_n(y) \Phi_n(z) \quad (\text{A2.16})$$

$$\Phi_n(z) = \sqrt{\frac{2}{z_c}} \sin\left(n + \frac{1}{2}\right) \frac{\pi z}{z_c}, \quad n = 0, 1, 2, \dots \quad (\text{A2.17})$$

$$u_{sn}(y) = [k_1 \sinh \lambda y + k_2 \cosh \lambda y + C_n] \quad (\text{A2.18})$$

$$\lambda = \frac{\pi}{z_c} \left(n + \frac{1}{2}\right) \quad (\text{A2.19})$$

$$C_n = -\frac{1}{\mu} \frac{dp}{dx} \frac{z_c^{2.5} \sqrt{2}}{\left(n + \frac{1}{2}\right)^3 \pi^3} \quad (\text{A2.20})$$

$$k_2 = -C_n = \frac{1}{\mu} \frac{dp}{dx} \frac{z_c^{2.5} \sqrt{2}}{\left(n + \frac{1}{2}\right)^3 \pi^3} \quad (\text{A2.21})$$

$$k_1 = -k_2 \frac{\sinh(\lambda y_c)}{\cosh(\lambda y_c)} \quad (\text{A2.22})$$

Shear stress is given by $\tau = \mu \nabla u(y, z)$; the shear stress on the membrane is

$$\tau_{\text{membrane}} = \mu \frac{du}{dy}(0, z). \quad (\text{A2.23})$$

The partial derivative with respect to y is

$$\frac{du}{dy}(y, z) = \sum_{n=1}^{\infty} \frac{du_n}{dy}(y) \Phi_n(z) = \sum_{n=1}^{\infty} [\lambda k_1 \cosh \lambda y + \lambda k_2 \sinh \lambda y] \Phi_n(z) \quad (\text{A2.24})$$

The force on one surface of the membrane is the shear stress integrated over the area of the membrane.

$$F_{\text{one side}} = L 2 \mu \int_0^{z_c} \frac{du}{dy} dz = L 2 \mu \sum_{n=1}^{\infty} \sqrt{\frac{2}{z_c}} \left(\frac{z_c}{\pi \left(n + \frac{1}{2}\right)} (-k_1) \right) \quad (\text{A2.25})$$

Equal flow is assumed on both sides of the membrane, so this result simply multiplied by 2 gives an estimate of the total force on the membrane (F_{tot}) from the fluid shear stress on both sides of the membrane.

$$F_{tot} = 2F_{one\ side} = 4L \int_0^{\kappa_c} \mu \frac{du}{dy} dz \quad (A2.26)$$

A2.2 Stresses Due to Pressure Differences Across the Membrane: Bending

For the beam bending problem, the curvature of the deformed membrane is

$$\kappa = \frac{d\theta}{ds} = \frac{d^2 u_y}{dz^2} \quad (A2.27)$$

where u_y is displacement of the membrane in the y -direction. The bending moment per unit depth of the membrane is

$$M_{membrane} = -K_B \frac{d^2 u_y}{dz^2} \quad (A2.28)$$

where $M_{membrane}$ is the moment per unit “depth”; in this case, the x -dimension, L .

The membrane bending modulus is

$$K_B = \frac{Et^3}{12(1-\nu^2)}. \quad (A2.29)$$

Stress in the z -direction is

$$\sigma_z = -\frac{My}{I_x}; M = M_{membrane} \cdot L. \quad (A2.30)$$

The moment of inertia is

$$I_x = \frac{Lt^3}{12}. \quad (A2.31)$$

Substituting M and I_x into the stress equation yields

$$\sigma_z = \frac{Ey}{(1-\nu^2)} \frac{d^2 u_y}{dz^2}. \quad (\text{A2.32})$$

Bending due to the pressure difference across a membrane is given by

$$\Delta P = K_B \frac{d^4 u_y}{dz^4}. \quad (\text{A2.33})$$

We can integrate to determine $u_y(z)$, using boundary conditions

$$u_y(0) = u_y(h) = 0 \quad (\text{A2.34})$$

(the ends of the membrane are ‘clamped,’ that is, adhesion is assumed over the entire surface of the membrane that contacts the wall);

and

$$\frac{du_y}{dz}\left(\frac{h}{2}\right) = \frac{du_y}{dz}(0) = \frac{du_y}{dz}(h) = 0. \quad (\text{A2.35})$$

The slope at the center of the membrane is zero due to symmetry, and the ends are clamped.

We integrate to find $\frac{d^2 u_y}{dz^2}$:

$$\frac{d^2 u_y}{dz^2} = \frac{\Delta P}{K_B} \left[\frac{z^2}{2} - \frac{hz}{2} + \frac{h^2}{12} \right] \quad (\text{A2.36})$$

and substitute into equation A2.32 to get

$$\sigma_z = \frac{Ey}{(1-\nu^2)} \frac{\Delta P}{K_B} \left[\frac{z^2}{2} - \frac{hz}{2} + \frac{h^2}{12} \right]. \quad (\text{A2.37})$$

Finally, we solve for ΔP

$$\Delta P = \frac{K_B \sigma_z}{Ey} \frac{(1-\nu^2)}{\left[\frac{z^2}{2} - \frac{hz}{2} + \frac{h^2}{12} \right]}. \quad (\text{A2.38})$$

The maximum $\frac{d^2 u_y}{dz^2}$ values occur at $z = 0, h$.

The maximum σ_z values occur at $y = \pm \frac{1}{2}$.

For $h=0$, $y = \frac{1}{2}$, and $\sigma_z = \sigma_{max}$ (the material fracture strength), one can calculate the critical pressure ΔP_{crit} at which the membrane will break.

A2.3 Stresses Due to Pressure Differences Across the Membrane: Surface Tension

The Laplace equation for surface tension is

$$\Delta P = N \left(\frac{1}{R_1} + \frac{1}{R_2} \right), \text{ where} \quad (\text{A2.39})$$

$$N = (\text{stress}) \cdot (\text{membrane thickness}). \quad (\text{A2.40})$$

Figure 2.13 shows R_1 in the z -direction, and R_2 in the x -direction. In these devices, R_1 is at least four times smaller than R_2 , therefore stresses induced along the R_2 direction can be ignored.

At failure,

$$N = \sigma_{max} \cdot t \quad (\text{A2.41})$$

Figure 2.14 shows a cross-sectional view along R_1 at the center of the membrane.

At failure,

$$\frac{S - h}{h} = \epsilon_{max} \quad (\text{A2.42})$$

From Figure A2.2,

$$R \cdot \sin \frac{\theta}{2} = \frac{h}{2}. \quad (\text{A2.43})$$

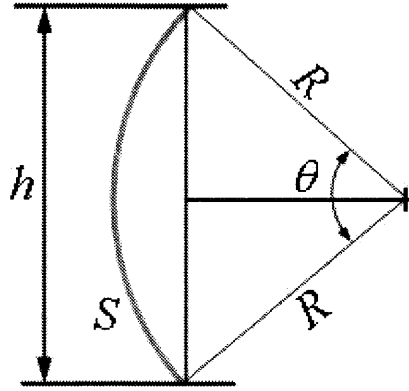


Figure A2.2. The stretched geometry of the membrane

Solving for R gives

$$R = \frac{h}{2 \sin \frac{\theta}{2}} \quad (\text{A2.44})$$

Also,

$$2\pi R \cdot \frac{\theta}{2\pi} = S. \quad (\text{A2.45})$$

Using

$$S = \theta R \quad (\text{A2.46})$$

gives

$$R = \frac{S}{\theta}. \quad (\text{A2.47})$$

To calculate ΔP_{crit} , both expressions for R as functions of θ (equations A2.44 and A2.47) are plotted, and the value of R at the intersection of the curves is used. The ΔP_{crit} that is calculated with this R value is the critical pressure that will generate surface tension strain and stress that will break the gel.

$$\Delta P_{crit} = \frac{\sigma_{max} t}{R} \quad (\text{A2.48})$$

A3.1 Mask Layouts

The layout images are screen-captures from the CADENCE CAD software.

The silicon mask layout (Figure A3.1):

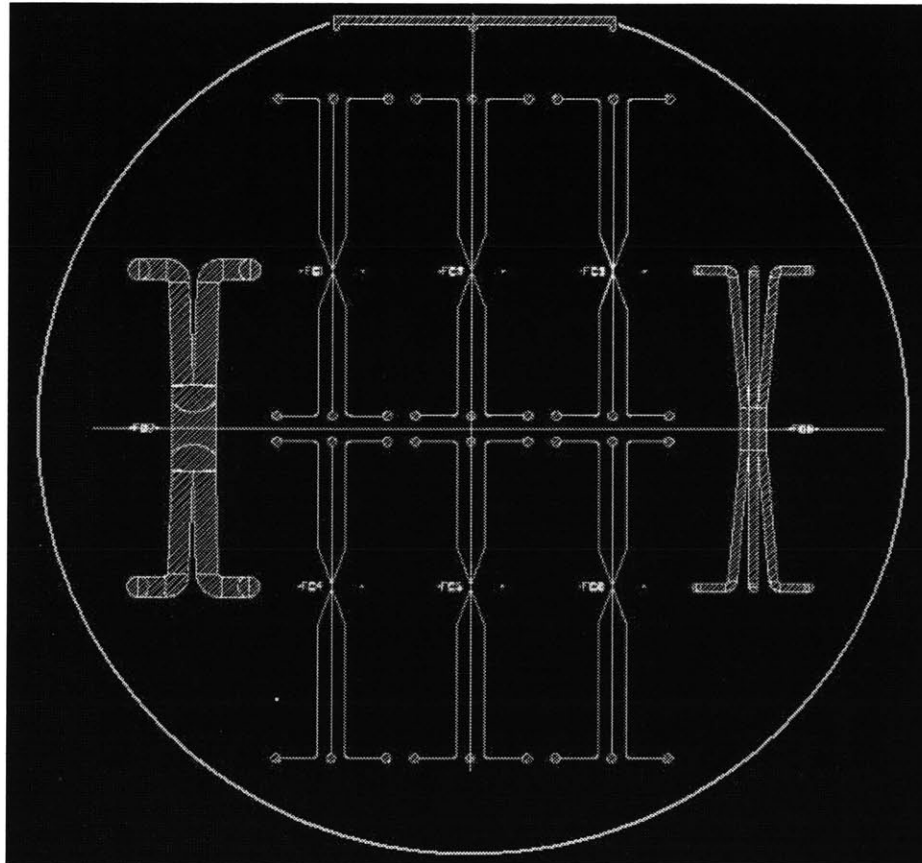


Figure A3.1. Layout for silicon wafer pattern. Horizontal and vertical axes are not part of the pattern.
Diameter of the wafer is 10.0 cm.

A detail view of the layout for device Fc1 (Figure A3.2):

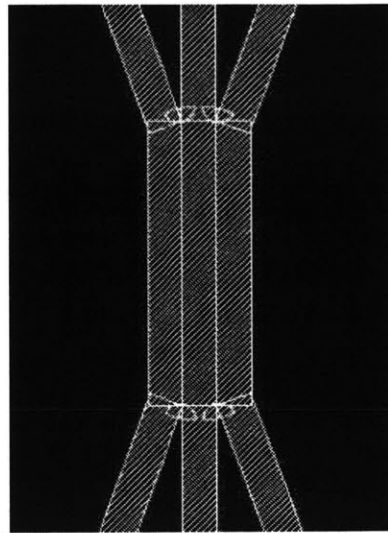


Figure A3.2. Detail view of the layout for device Fc1

The glass mask layout (Figure A3.3):

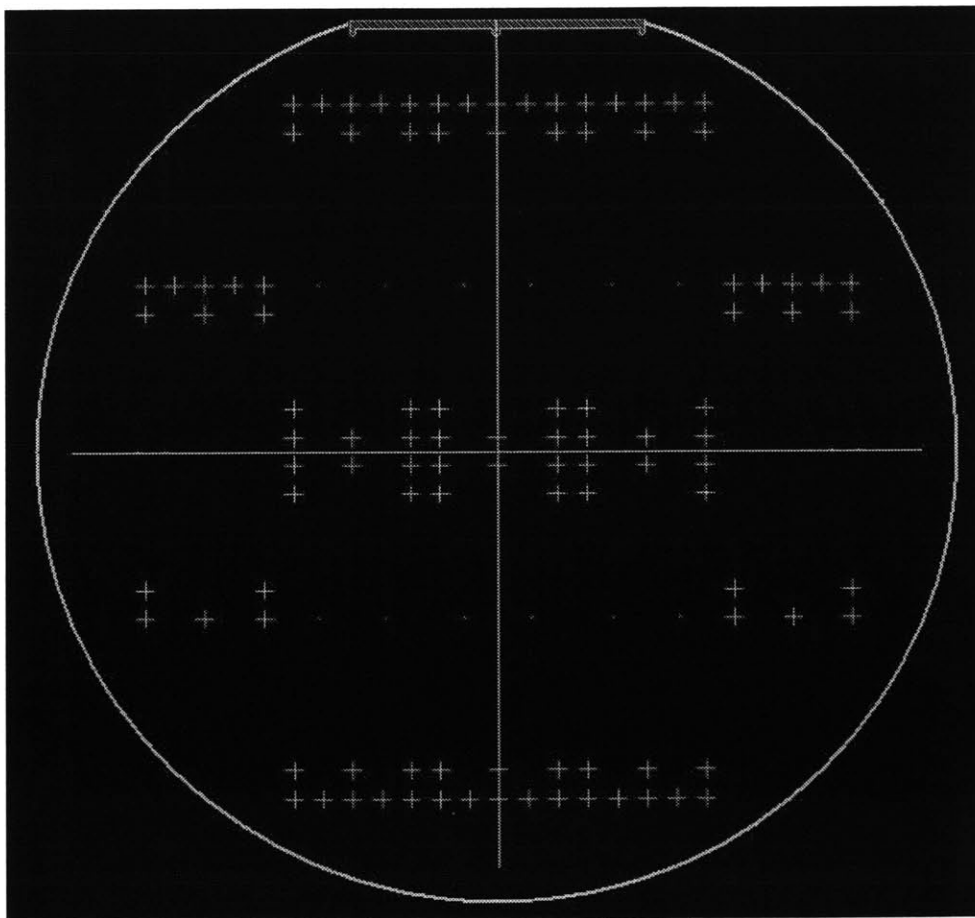


Figure A3.3. Layout for glass wafer pattern. Horizontal and vertical axes are not part of the pattern.
Diameter of the wafer is 10.0 cm.

A3.2 Fluidic Fittings: Fabrication and Assembly

A3.2.1 Large-Bore Fittings

The large-bore metal fluidic fittings were machined from stainless steel tube and rod (Figure A3.4), and were assembled using MSD 505-3 epoxy (Figure A3.5). The tubes were slip-fit onto the bases, and the epoxy was applied around the interface with a micro-spatula. The assembly was left at room temperature for 12 hours to let the epoxy harden, then the epoxy was cured for 24 hours in a 60°C oven.

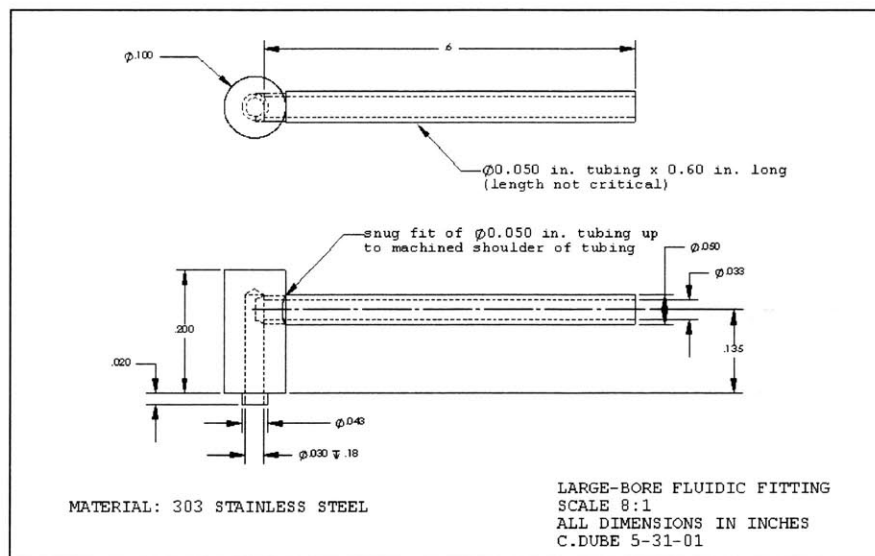


Figure A3.4. Machine drawing for large-bore fluidic fitting

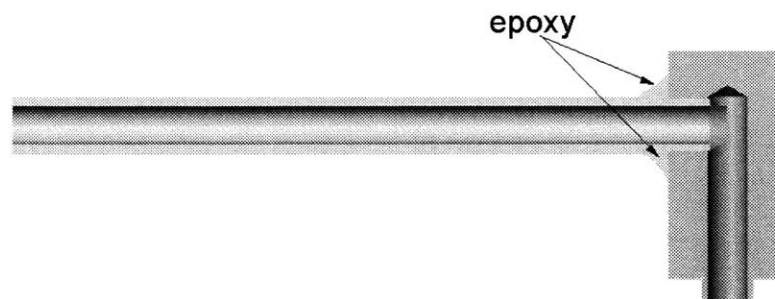


Figure A3.5. Cross-section of the large-bore fluidic fitting, showing locations of epoxy

A3.2.2 Small-Bore Fittings

The small-bore metal fluidic fittings were machined from stainless steel rod and small-gauge hypodermic tube stock (Figure A3.6, Figure A3.7). The Small-Bore Tube is slip-fit into the Small-Bore Base, and MSD 505-3 epoxy was applied to the interface with a micro-spatula (Figure A3.8). The assembly was left at room temperature for 12 hours to let the epoxy harden. The epoxy was then cured for 24 hours in a 60°C oven.

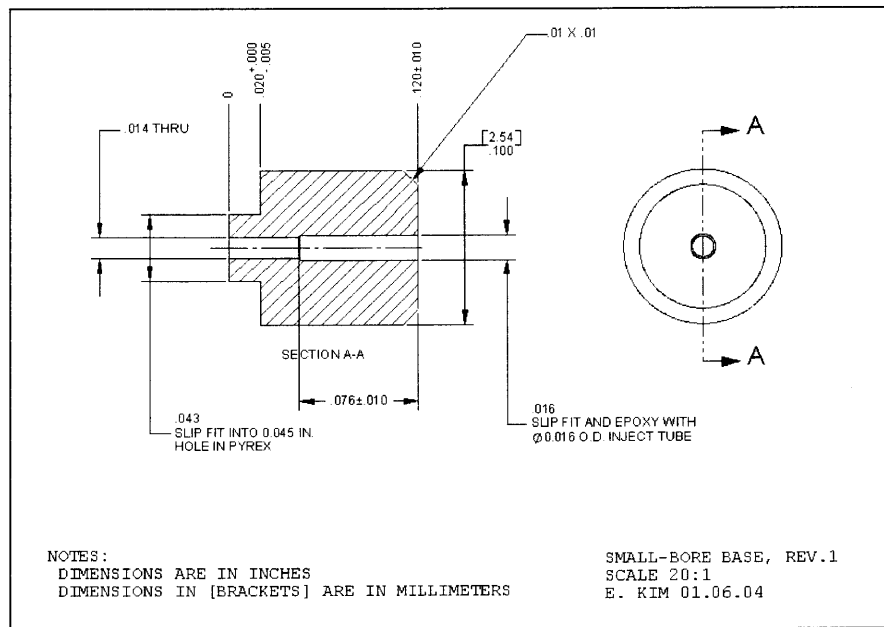


Figure A3.6. Machine drawing for small-bore fluidic fitting, base

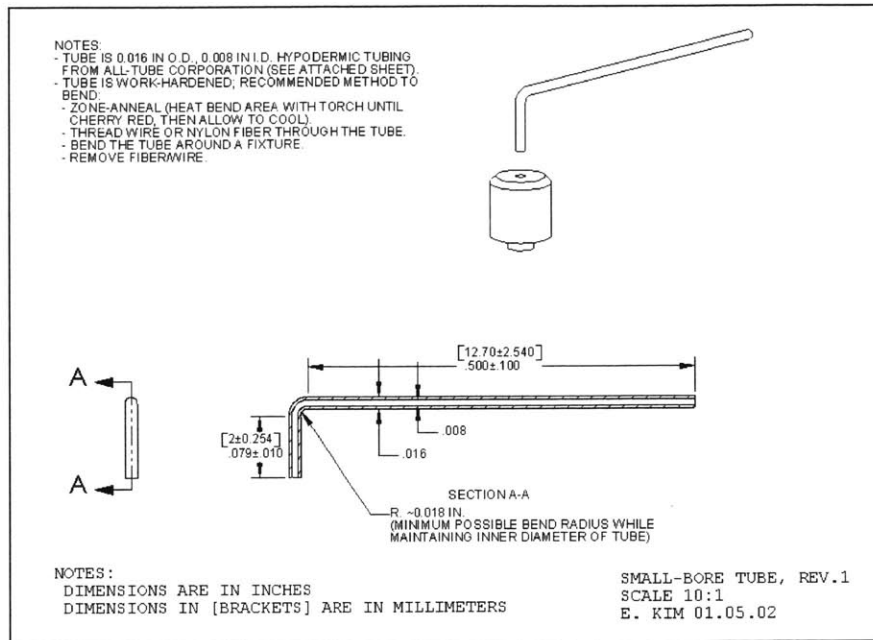


Figure A3.7. Machine drawing for small-bore fluidic fitting, tube

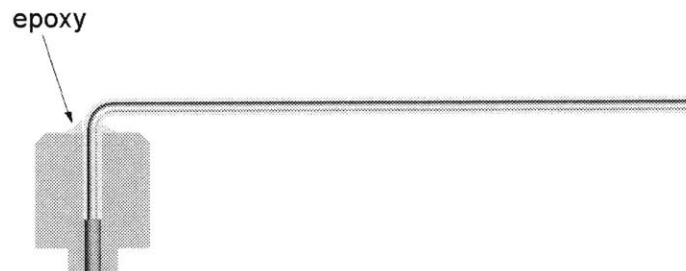


Figure A3.8. Cross-section of the small-bore fluidic fitting, showing location of epoxy

A3.3 Adhesive Gasket

The adhesive gasket was fabricated from 3M Core Series 2-0300 adhesive film (3M Worldwide, St. Paul, MN). The film was ~0.0004 inches thick, and was packaged in a roll with a layer of backing paper to prevent the adhesive from contacting itself. The final dimensions of the ring were I.D. Ø0.045, O.D. Ø0.100 (Figure A3.9).

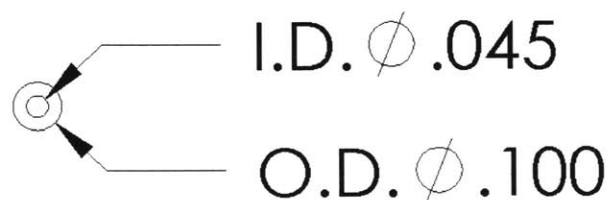


Figure A3.9. Drawing of the adhesive gasket

A strip of adhesive was cut off of the roll. Extra backing paper was placed on the exposed adhesive surface to make a sandwich (Figure A3.10). A Ø0.045 inch hole was punched through the sandwich. The top paper was pulled off and a fluidic fitting was pushed through the hole so that the adhesive film stuck to the base of the fitting.

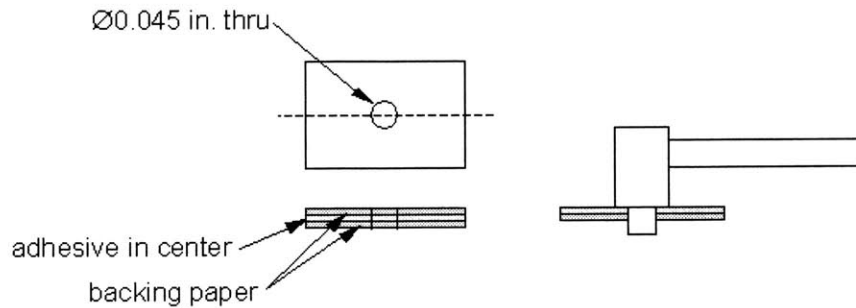


Figure A3.10. Assembly of the adhesive gasket, part 1

With a razor blade, scalpel, or very small pair of scissors, the adhesive-paper stack was trimmed to the outer diameter of the fluidic fitting. The remaining backing paper was removed, and the fluidic fitting was pressed gently and firmly into a hole on the device (Figure A3.11, Figure A3.12). Epoxy was then applied around the base of the fluidic fitting at the glass-metal interface.

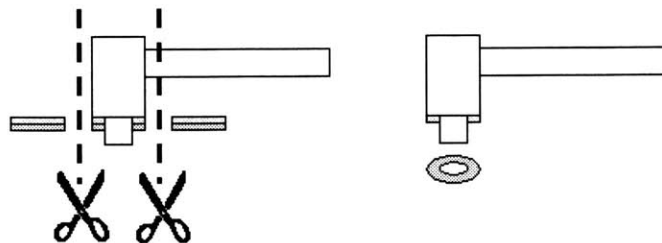


Figure A3.11. Assembly of the adhesive gasket, part 2

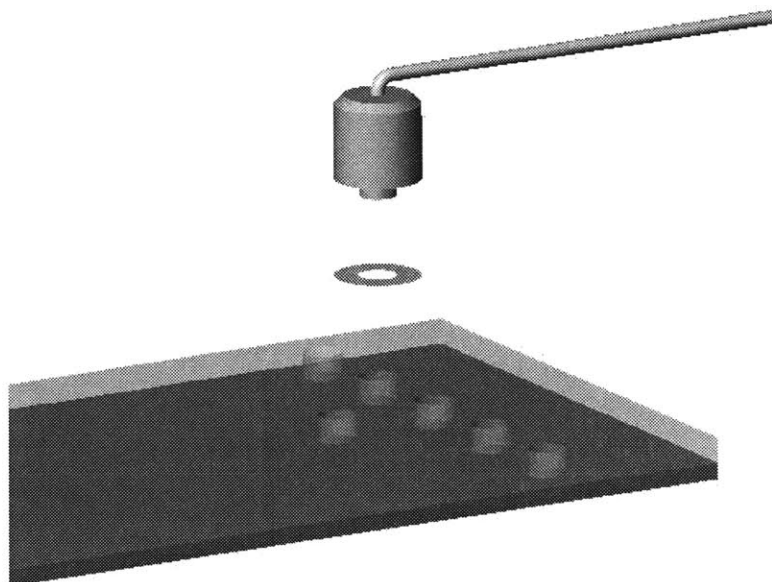


Figure A3.12. Exploded view, showing the location of the adhesive gasket between the glass-silicon device and the fluidic fitting

A3.4 Modifications to the Harvard Apparatus PHD 2000 Push/Pull syringe pump

With the proper accessories, a standard Harvard PHD 2000 syringe pump can “push” or “pull” up to 10 syringes (*i.e.*, all syringes are either simultaneously injecting or withdrawing fluid) (Figure A3.13). The PHD 2000 Pull/Pull Pump is equipped with syringe holders mounted in opposite directions to each other, with a single plunger/piston actuator so that, when similar syringes are mounted on opposite sides of the actuator, the pump can simultaneously infuse and withdraw fluid at the same flow rate (Figure A3.14).

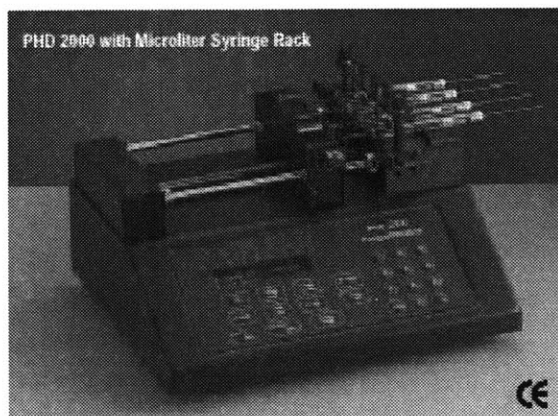


Figure A3.13. Standard PHD 2000 with 4 syringe rack [17]

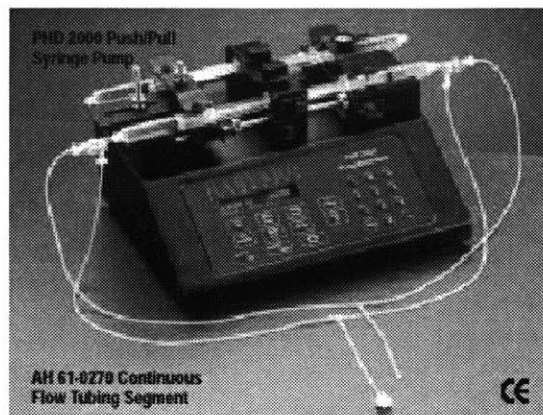


Figure A3.14. PHD 2000 Push/Pull Syringe Pump [17]

Our initial protocol required three syringes to be infused while three syringes were withdrawn at identical flow rates. This would require at least two standard syringe pumps. A more economic alternative was to modify the pump to push four and pull four syringes simultaneously. While Harvard Apparatus makes and sells multi-syringe racks for attachment to the “Push” side of the actuator, they do not make a similar attachment for the “Pull” side. Modifications and new parts were designed to allow a standard 4-syringe rack to be mounted on the “Pull” side of the pump (see Figure 3.7 for a photograph of the modified PHD2000 Push/Pull syringe pump). The modifications were designed to have no negative effects on the functionality of the pump or the 4-syringe rack.

The modifications and part drawings are shown below.

- Harvard Apparatus PHD2000 Push-Pull Pump modification, exploded assembly view (Figure A3.15)

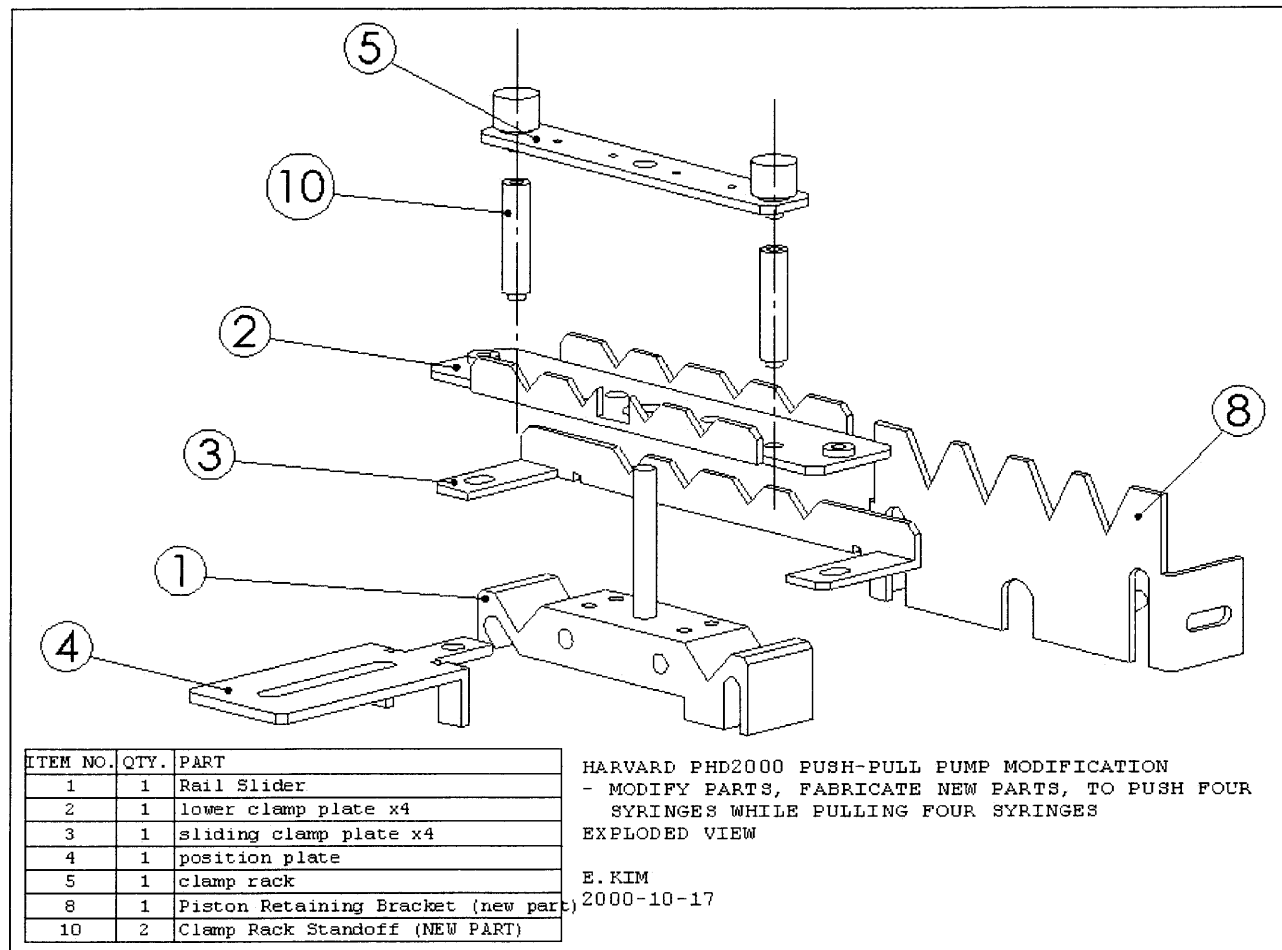


Figure A3.15. Exploded-assembly drawing of the Harvard PHD2000 Push-Pull Pump Modifications

This drawing shows and lists the parts to be modified or fabricated. There are a total of 7 different parts; 5 are modifications of existing parts, and 2 are new parts.

- Rail Slider – This is a modification of an existing part (Figure A3.16).

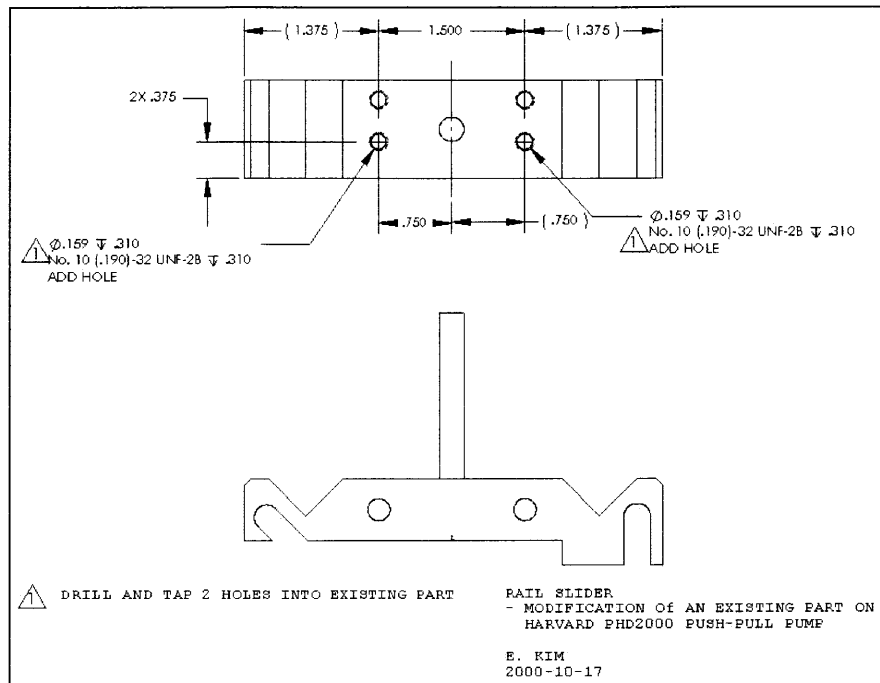


Figure A3.16. Rail Slider, modification of an existing part

- Lower Clamp Plate - This is a modification of an existing part (Figure A3.17).

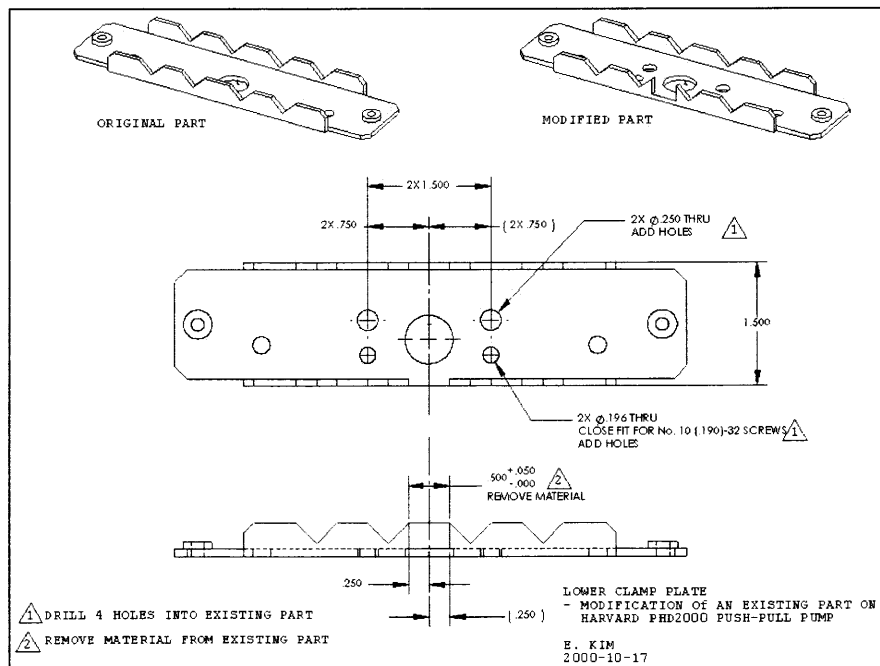


Figure A3.17. Lower Clamp Plate, modification of an existing part

- Sliding Clamp Plate – This is a modification of an existing part (Figure A3.18).

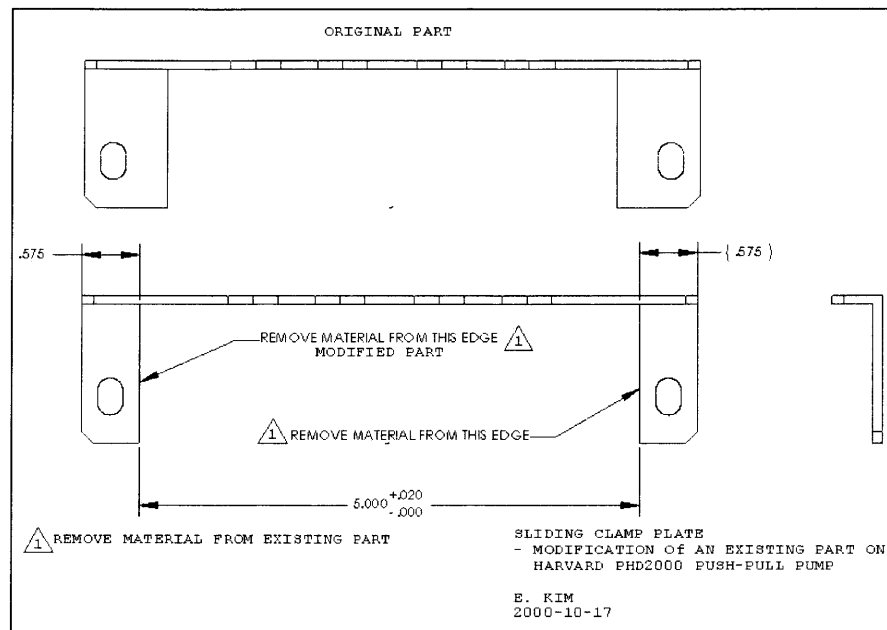


Figure A3.18. Sliding Clamp Plate, modification of an existing part

- Position Plate – This is a modification of an existing part (Figure A3.19).

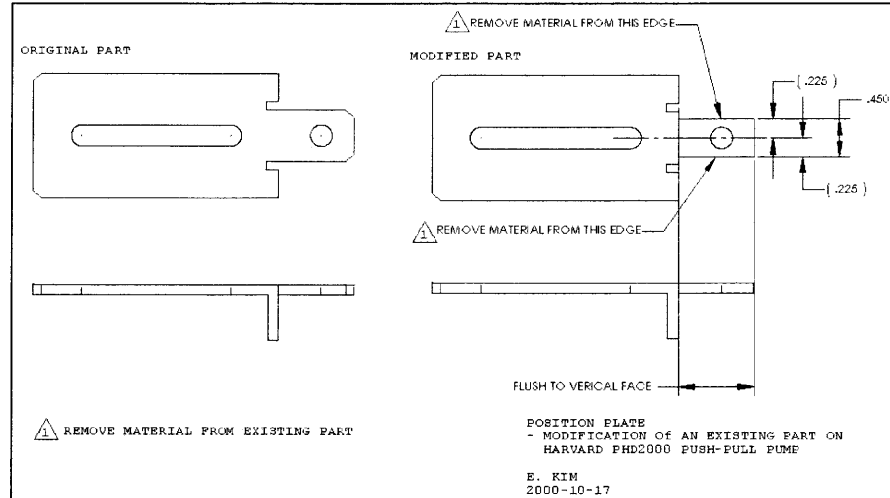


Figure A3.19. Position Plate, modification of an existing part

- Clamp Rack – This is a modification of an existing part (Figure A3.20).

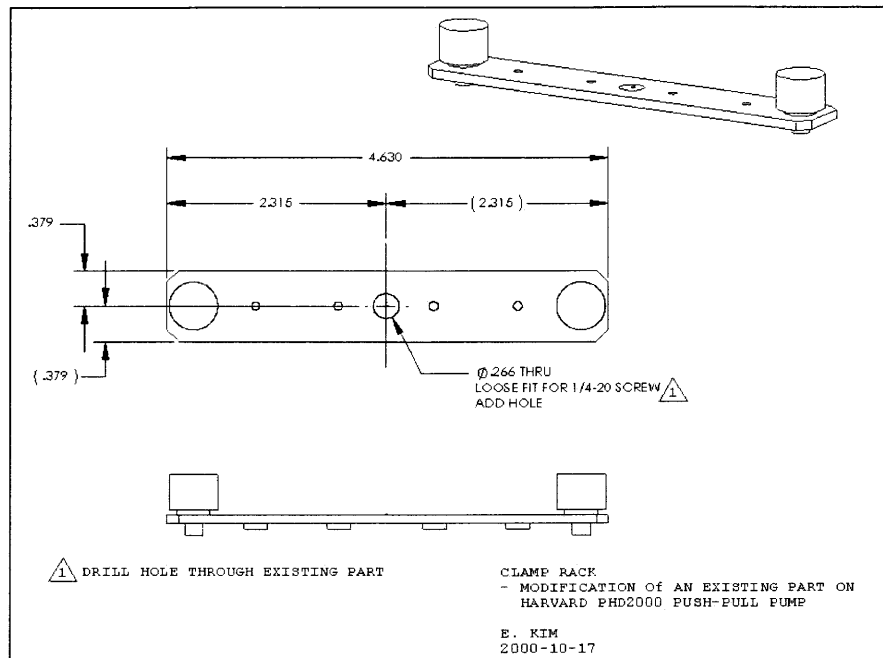


Figure A3.20. Clamp Rack, modification of an existing part

- Piston Retaining Bracket – This is a new part (Figure A3.21, Figure A3.22).

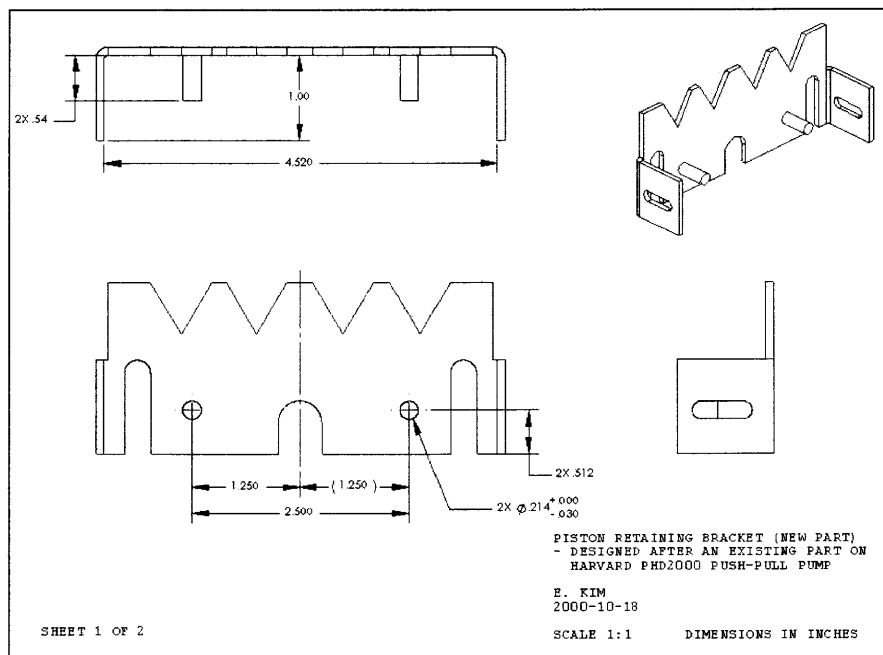


Figure A3.21. Piston Retaining Bracket, new part, sheet 1 of 2

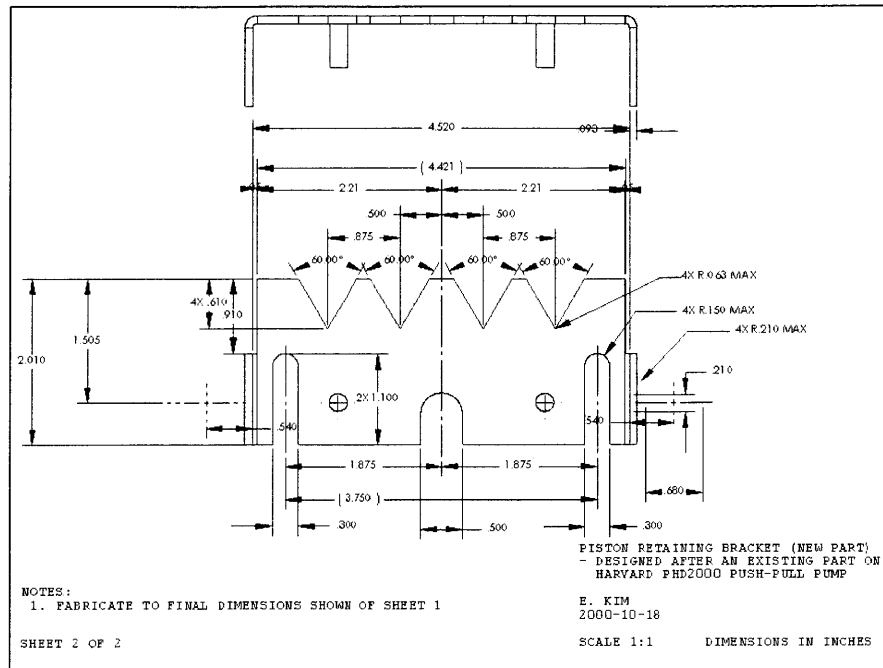


Figure A3.22. Piston Retaining Bracket, sheet 2 of 2

- Clamp Rack Standoff – This is a new part (Figure A3.23).

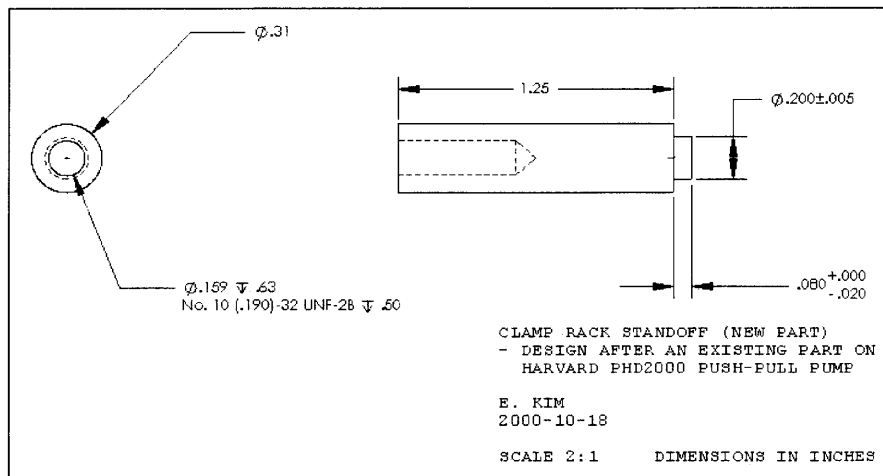


Figure A3.23. Clamp Rack Standoff, new part

A4.1 Peptide Solution Density Measurements

The density of the peptide in solution was measured using a 1.0 weight percent KFE8 solution. A volume of solution was measured on an Ohaus Analytical Plus balance (Ohaus Corporation, Pine Brook, NJ) using a 100 μl Eppendorf Reference[®] pipetor (Eppendorf, Hamburg, Germany) (Table A4.1).

Table A4.1. Density data for the 1.0 wt percent KFE8 solution

Density of 1 wt% KFE8 solution		
Vol [μl]	Mass [mg]	Density, ρ [kg/m^3]
20	20.40	1020
30	30.80	1026.667
24.95	24.98	1001.202
19.95	20.90	1047.619

Mass was plotted versus volume, and the trendline was required to pass through the origin (zero volume = zero mass), resulting in the calculated density of the peptide solution (Figure A4.1),

$$\rho_{1 \text{ wt. \% KFE8}} = 1.0223 \text{ g/ml.}$$

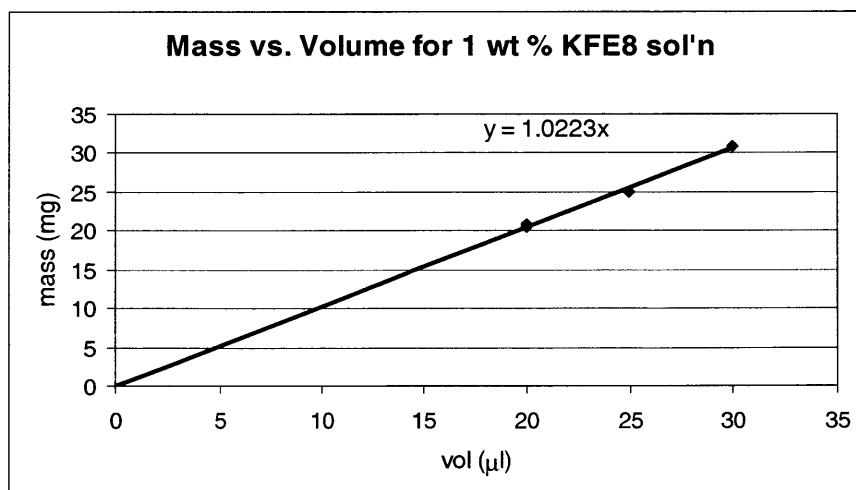


Figure A4.1. Mass vs. volume for 1.0 weight percent KFE8 solution

A4.2 Peptide Solution Viscosity Measurements

The viscosity of the peptide solution was measured on an AR 1000N rheometer (TA Instruments, New Castle, DE). The peptide in solution was tested and was shown to exhibit shear-thinning behavior; the solution was more viscous at lower shear rates, and less viscous at higher shear rates (Figure A4.2).

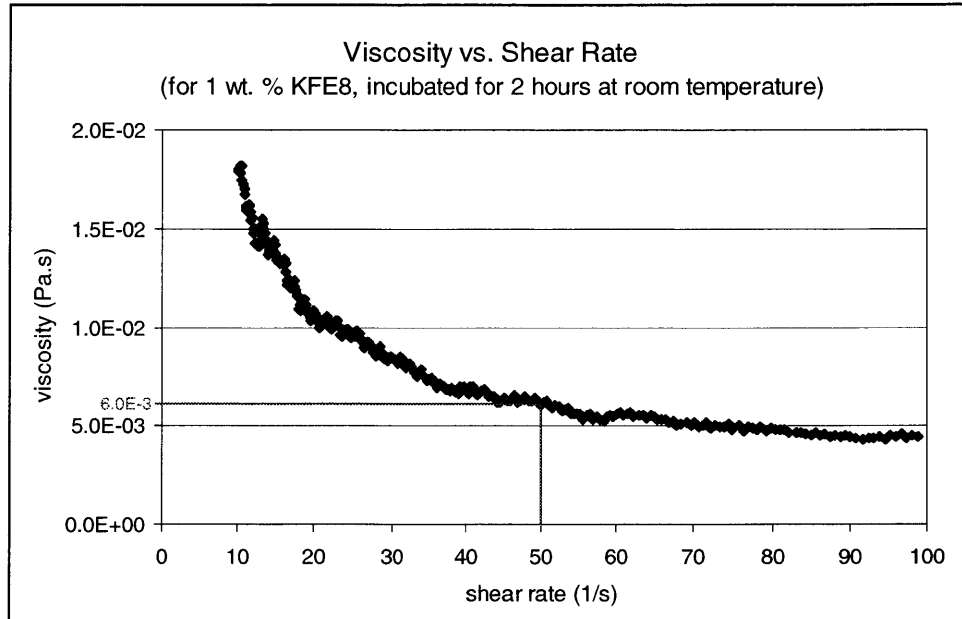


Figure A4.2. Viscosity vs. shear rate for 1 weight % KFE8 solution; note the shear thinning behavior of the fluid. Using the average fluid velocity and the typical channel dimensions of our devices, an approximation for shear rate can be calculated, and the corresponding viscosity can be determined. For an average velocity in the device $V_{average} \approx 3.0 \times 10^{-3}$ m/s (see Section 4.2.1), the approximate maximum velocity will be $V_{max} \approx 6.0 \times 10^{-3}$ m/s. The width of an Fc1 channel is $L = 2.4 \times 10^{-5}$ m, so the approximate shear rate is

$$\frac{V_{max}}{\frac{1}{2} \cdot L} = 50 \text{ 1/s} \quad (\text{A4.1})$$

A shear rate of 50 1/s gives us an approximate viscosity value of

$$\mu_{KFE8} \approx 0.006 \text{ Pa}\cdot\text{s}$$

A4.3 Derivation of the Analytic Solution

At steady state,

$$\frac{\partial u}{\partial t} = 0 \quad (\text{A4.2})$$

and flow is solely in the x-direction: $v = 0$ and $w = 0$

Ignoring the short entrance and exit regions, the flow is fully-developed so that:

$$\frac{\partial u}{\partial x} = 0, \quad (\text{A4.3})$$

$$\frac{\partial^2 u}{\partial x^2} = 0, \quad (\text{A4.4})$$

$$\text{and } u = u(y, z). \quad (\text{A4.5})$$

Assuming dp/dx is constant over the device, the Navier-Stokes equation then simplifies to

$$\frac{\partial p}{\partial x} = \mu \left(\frac{\partial^2 u}{\partial y^2} + \frac{\partial^2 u}{\partial z^2} \right). \quad (\text{A4.6})$$

The boundary conditions are:

$$\text{No flow at the walls } u_s(0, z) = 0 \quad \text{saline region} \quad (\text{A4.7})$$

$$u_s(y, 0) = 0 \quad \text{saline region, } y = 0 \text{ to } y_m \quad (\text{A4.8})$$

$$u_p(y, 0) = 0 \quad \text{peptide region, } y = y_m \text{ to } y_c \quad (\text{A4.9})$$

The velocity gradient is zero at the centerlines:

$$\frac{\partial u_s}{\partial z}(y, z_c) = 0 \quad \text{saline region, } y = 0 \text{ to } y_m \quad (\text{A4.10})$$

$$\frac{\partial u_p}{\partial z}(y, z_c) = 0 \quad \text{peptide region} \quad (\text{A4.11})$$

$$\frac{\partial u_p}{\partial y}(y_c, z) = 0 \quad \text{peptide region} \quad (\text{A4.12})$$

Velocity and shear stress are continuous across the two fluids

$$u_s(y_m, z) = u_p(y_m, z) \quad (\text{A4.13})$$

$$\mu_s \frac{\partial u_s}{\partial y}(y_m, z) = \mu_p \frac{\partial u_p}{\partial y}(y_m, z) \quad (\text{A4.14})$$

Using the Finite Fourier Transform method [9], the form of the solution is

$$u_s(y, z) = \sum_{n=1}^{\infty} u_{sn}(y) \Phi_n(z) \quad u_{sn} = \text{series coefficients for the saline region solution} \quad (\text{A4.15})$$

$$u_p(y, z) = \sum_{n=1}^{\infty} u_{pn}(y) \Phi_n(z) \quad u_{pn} = \text{series coefficients for the peptide region solution} \quad (\text{A4.16})$$

For the boundary conditions in the z -dimension, $\Phi_n(z)$ fits Deen's Case III [9]:

$$\Phi_n(z=0) = 0; \Phi'_n(z=z_c) = 0 \quad (\text{A4.17, A4.18})$$

$$\Phi_n(z) = \sqrt{\frac{2}{z_c}} \sin\left(n + \frac{1}{2}\right) \frac{\pi z}{z_c}, \quad n = 0, 1, 2, \dots \quad (\text{A4.19})$$

For the saline region

$$\frac{\partial p}{\partial x} = \mu_s \left(\frac{\partial^2 u_s}{\partial y^2} + \frac{\partial^2 u_s}{\partial z^2} \right) \quad (\text{A4.6})$$

$$u_s(0, z) = 0 \quad (\text{A4.7})$$

$$u_s(y, 0) = 0 \quad (\text{A4.8})$$

$$\frac{\partial u_s}{\partial z}(y, z_c) = 0 \quad (\text{A4.10})$$

The finite Fourier Transform is defined as

$$u_{sn}(y) = \int_0^{z_c} \Phi_n(z) u_s(y, z) dz \quad (\text{A4.20})$$

Transform (4.6)

first term:

$$\int_0^{z_c} \Phi_n \frac{\partial p}{\partial x} dz = \int_0^{z_c} \sqrt{\frac{2}{z_c}} \sin\left(\left(n + \frac{1}{2}\right) \frac{\pi z}{z_c}\right) \frac{\partial p}{\partial x} dz = \left[-\sqrt{\frac{2}{z_c}} \frac{\partial p}{\partial x} \frac{z_c}{\left(n + \frac{1}{2}\right) \pi} \cos\left(\left(n + \frac{1}{2}\right) \frac{\pi z}{z_c}\right) \right]_0^{z_c},$$

(A4.21)

$$n=0,1,2,\dots$$

$$\int_0^{z_c} \Phi_n \frac{\partial p}{\partial x} dz = \sqrt{\frac{2}{z_c}} \frac{\partial p}{\partial x} \frac{z_c}{\left(n + \frac{1}{2}\right) \pi} \quad \text{First term}$$

(A4.22)

second term:

$$\int_0^{z_c} \Phi_n \mu \frac{\partial^2 u_s}{\partial y^2} dz = \mu \frac{\partial^2}{\partial y^2} \int_0^{z_c} \Phi_n u_s dz = \mu \frac{\partial^2 u_{sn}}{\partial y^2} \quad \text{Second term}$$

(A4.23)

third term:

$$\begin{aligned} \int_0^{z_c} \Phi_n \mu \frac{\partial^2 u_s}{\partial z^2} dz &= \mu \Phi_n \frac{\partial u_s}{\partial z} \Big|_{z=0}^{z=z_c} - \mu \int_0^{z_c} \frac{\partial u_s}{\partial z} \frac{\partial \Phi_n}{\partial z} dz \\ &= \mu \Phi_n \frac{\partial u_s}{\partial z} \Big|_{z=0}^{z=z_c} - \mu u_s \frac{\partial \Phi_n}{\partial z} \Big|_{z=0}^{z=z_c} + \mu \int_0^{z_c} u_s \frac{\partial^2 \Phi_n}{\partial z^2} dz \end{aligned}$$

(A4.24)

$$\mu \Phi_n \frac{\partial u_s}{\partial z} \Big|_{z=0}^{z=z_c} = \mu \Phi_n(z_c) \frac{\partial u_s}{\partial z}(z_c) - \mu \Phi_n(0) \frac{\partial u_s}{\partial z}(0) = 0 - 0 = 0$$

(A4.25)

$$\begin{aligned} \mu u_s \frac{\partial \Phi_n}{\partial z} \Big|_{z=0}^{z=z_c} &= \\ &= \mu u_s(y, z_c) \left(-\sqrt{\frac{2}{z_c}} \frac{z_c}{\left(n + \frac{1}{2}\right) \pi} \cos\left(\left(n + \frac{1}{2}\right) \pi\right) \right) - \mu u_s(y, 0) \left(-\sqrt{\frac{2}{z_c}} \frac{z_c}{\left(n + \frac{1}{2}\right) \pi} \cos(0) \right) = 0 - 0 \end{aligned}$$

(A4.26)

$$\mu \int_0^{z_c} u_s \frac{\partial^2 \Phi_n}{\partial z^2} dz = \int_0^{z_c} -\mu u_s \left(\left(n + \frac{1}{2}\right) \frac{\pi}{z_c} \right)^2 \sqrt{\frac{2}{z_c}} \sin\left(n + \frac{1}{2}\right) \frac{\pi z}{z_c} dz$$

(A4.27)

$$\mu \int_0^{\epsilon_c} u_s \frac{\partial^2 \Phi_n}{\partial z^2} dz = \int_0^{\epsilon_c} -\mu u_s \left(\left(n + \frac{1}{2} \right) \frac{\pi}{z_c} \right)^2 \Phi_n dz = -\mu \left(\left(n + \frac{1}{2} \right) \frac{\pi}{z_c} \right)^2 \int_0^{\epsilon_c} u_s \Phi_n dz \quad (\text{A4.28})$$

$$\boxed{\int_0^{\epsilon_c} \Phi_n \mu \frac{\partial^2 u_s}{\partial z^2} dz = -\mu \left(\left(n + \frac{1}{2} \right) \frac{\pi}{z_c} \right)^2 u_{sn} \quad \text{Third term}} \quad (\text{A4.29})$$

$$\boxed{\frac{\partial p}{\partial x} \frac{\sqrt{2z_c}}{\left(n + \frac{1}{2} \right) \pi \mu} = \frac{\partial^2 u_{sn}}{\partial y^2} - \left(\left(n + \frac{1}{2} \right) \frac{\pi}{z_c} \right)^2 u_{sn}} \quad (\text{A4.30})$$

Transform the boundary conditions:

$$u_s(0, z) = 0 \quad (\text{A4.7})$$

$$u_{sn}(0) = \int_0^{\epsilon_c} \Phi_n(z) u_s(0, z) dz = 0$$

$$u_{sn}(0) = 0 \quad (\text{A4.31})$$

$$u_s(y, 0) = 0 \quad \text{satisfied by the basis function} \quad (\text{A4.8})$$

$$\frac{\partial u_s}{\partial z}(y, z_c) = 0 \quad \text{satisfied by the basis function} \quad (\text{A4.10})$$

A similar analysis for the peptide region yields the FFT Navier-Stokes equation for the peptide region and boundary conditions. The shared boundary conditions are also transformed:

$\frac{\partial^2 u_{sn}}{\partial y^2} - \left(\frac{\pi}{z_c} \right)^2 \left(n + \frac{1}{2} \right)^2 u_{sn} = \frac{\partial p}{\partial x} \frac{\sqrt{2z_c}}{\left(n + \frac{1}{2} \right) \pi \mu_s}$	(A4.30)
$u_{sn}(0) = 0$	(A4.31)
$\frac{\partial^2 u_{pn}}{\partial y^2} - \left(\frac{\pi}{z_c} \right)^2 \left(n + \frac{1}{2} \right)^2 u_{pn} = \frac{\partial p}{\partial x} \frac{\sqrt{2z_c}}{\left(n + \frac{1}{2} \right) \pi \mu_p}$	(A4.32)

$\frac{\partial u_{p_n}(y_c)}{\partial y} = 0$	(A4.33)
$u_{s_n}(y_m) = u_{p_n}(y_m)$	(A4.34)
$\mu_s \frac{\partial u_{s_n}(y_m)}{\partial y} = \mu_p \frac{\partial u_{p_n}(y_m)}{\partial y}$	(A4.35)

Rewrite A4.30 as

$$u''_{s_n} + \sigma u_{s_n} = A_{s_n} \quad (\text{A4.36})$$

$$\sigma = -\left(\frac{\pi}{z_c}\right)^2 \left(n + \frac{1}{2}\right)^2 \quad (\text{A4.37})$$

$$\lambda = \frac{\pi}{z_c} \left(n + \frac{1}{2}\right) \quad (\text{A4.38})$$

$$A_{s_n} = \frac{\partial p}{\partial x} \frac{\sqrt{2z_c}}{\left(n + \frac{1}{2}\right) \pi \mu_{s_n}} \quad (\text{A4.39})$$

$\sigma < 0$, so the general solution is

$$u_{s_n}(y) = k_1 \sinh \lambda y + k_2 \cosh \lambda y + C_{s_n} \quad (\text{A4.40})$$

Solve for C_{s_n}

$$C_{s_n} = -\frac{1}{\mu_s} \frac{\partial p}{\partial x} \frac{z_c^{2.5} \sqrt{2}}{\left(n + \frac{1}{2}\right)^3 \pi^3} \quad (\text{A4.41})$$

$$\text{at } u_{s_n}(0) = 0 \quad (\text{A4.31})$$

$$u_{s_n}(0) = k_1 \sinh(0) + k_2 \cosh(0) + C_{s_n} = 0 \quad (\text{A4.42})$$

$$u_{s_n}(0) = 0 + k_2 + C_{s_n} = 0 \quad (\text{A4.43})$$

$$k_2 = -C_{sn} = \frac{1}{\mu_s} \frac{\partial p}{\partial x} \frac{z_c^{2.5} \sqrt{2}}{\left(n + \frac{1}{2}\right)^3 \pi^3} \quad (\text{A4.44})$$

$$u_{sn}(y) = \left[k_1 \sinh \lambda y + \frac{1}{\mu_s} \frac{\partial p}{\partial x} \frac{z_c^{2.5} \sqrt{2}}{\left(n + \frac{1}{2}\right)^3 \pi^3} \cosh \lambda y - \frac{1}{\mu_s} \frac{\partial p}{\partial x} \frac{z_c^{2.5} \sqrt{2}}{\left(n + \frac{1}{2}\right)^3 \pi^3} \right] \quad (\text{A4.45})$$

use
$$c_n = \frac{\partial p}{\partial x} \frac{z_c^{2.5} \sqrt{2}}{\left(n + \frac{1}{2}\right)^3 \pi^3} \quad (\text{A4.46})$$

$$u_{sn}(y) = \left[k_1 \sinh \lambda y + \frac{1}{\mu_s} c_n \cosh \lambda y - \frac{1}{\mu_s} c_n \right] \quad (\text{A4.47})$$

A similar analysis for the peptide region yields

$$u_{pn}(y) = k_3 \sinh \lambda y + k_4 \cosh \lambda y - \frac{1}{\mu_p} c_n \quad (\text{A4.48})$$

$$\frac{\partial u_{pn}(y_c)}{\partial y} = 0 \quad (\text{A4.33})$$

$$\frac{\partial u_{pn}(y_c)}{\partial y} = k_3 \lambda \cosh \lambda y_c + k_4 \lambda \sinh \lambda y_c = 0 \quad (\text{A4.49})$$

$$k_3 \cosh \lambda y_c = -k_4 \sinh \lambda y_c \quad (\text{A4.50})$$

$$k_3 = -k_4 \frac{\sinh \lambda y_c}{\cosh \lambda y_c} \quad (\text{A4.51})$$

$$u_{pn}(y) = \left[-k_4 \frac{\sinh \lambda y_c}{\cosh \lambda y_c} \sinh \lambda y + k_4 \cosh \lambda y - \frac{1}{\mu_p} c_n \right] \quad (\text{A4.52})$$

k_1 and k_4 are solved using the shared boundary conditions.

$$u_{sn}(y_m) = u_{pn}(y_m) \quad (\text{A4.34})$$

$$\left[k_1 \sinh \lambda y_m + \frac{1}{\mu_s} c_n \cosh \lambda y_m - \frac{1}{\mu_s} c_n \right] = \left[-k_4 \frac{\sinh \lambda y_c}{\cosh \lambda y_c} \sinh \lambda y_m + k_4 \cosh \lambda y_m - \frac{1}{\mu_p} c_n \right] \quad (\text{A4.53})$$

Solve for k_1

$$k_1 = -k_4 \frac{\sinh \lambda y_c}{\cosh \lambda y_c} \frac{\sinh \lambda y_m}{\sinh \lambda y_m} + k_4 \frac{\cosh \lambda y_m}{\sinh \lambda y_m} - \frac{1}{\mu_s} c_n \frac{\cosh \lambda y_m}{\sinh \lambda y_m} - \frac{1}{\mu_p} \frac{c_n}{\sinh \lambda y_m} + \frac{1}{\mu_s} \frac{c_n}{\sinh \lambda y_m} \quad (\text{A4.54})$$

Simplify

$$k_1 = -k_4 \tanh \lambda y_c + k_4 \coth \lambda y_m - \frac{1}{\mu_s} c_n \coth \lambda y_m - \frac{1}{\mu_p} c_n \operatorname{csch} \lambda y_m + \frac{1}{\mu_s} c_n \operatorname{csch} \lambda y_m \quad (\text{A4.55})$$

$$\mu_s \frac{\partial u_{s_n}(y_m)}{\partial y} = \mu_p \frac{\partial u_{p_n}(y_m)}{\partial y} \quad (\text{A4.35})$$

$$\frac{\partial u_{s_n}(y_m)}{\partial y} = k_1 \lambda \cosh \lambda y_m + \frac{1}{\mu_s} c_n \lambda \sinh \lambda y_m \quad (\text{A4.56})$$

$$\frac{\partial \Theta_{p_n}(y_m)}{\partial y} = -k_4 \frac{\sinh \lambda y_c}{\cosh \lambda y_c} \lambda \cosh \lambda y_m + k_4 \lambda \sinh \lambda y_m \quad (\text{A4.57})$$

$$\mu_s k_1 \lambda \cosh \lambda y_m + c_n \lambda \sinh \lambda y_m = -\mu_p k_4 \frac{\sinh \lambda y_c}{\cosh \lambda y_c} \lambda \cosh \lambda y_m + \mu_p k_4 \lambda \sinh \lambda y_m \quad (\text{A4.58})$$

Solve for k_1

$$k_1 = -\frac{\mu_p}{\mu_s} k_4 \frac{\sinh \lambda y_c}{\cosh \lambda y_c} \frac{\lambda \cosh \lambda y_m}{\lambda \cosh \lambda y_m} + \frac{\mu_p}{\mu_s} k_4 \frac{\lambda \sinh \lambda y_m}{\lambda \cosh \lambda y_m} - \frac{1}{\mu_s} c_n \frac{\lambda \sinh \lambda y_m}{\lambda \cosh \lambda y_m} \quad (\text{A4.59})$$

Simplify

$$k_1 = -\frac{\mu_p}{\mu_s} k_4 \tanh \lambda y_c + \frac{\mu_p}{\mu_s} k_4 \tanh \lambda y_m - \frac{1}{\mu_s} c_n \tanh \lambda y_m \quad (\text{A4.60})$$

Solve for k_4

$$k_1 = -k_4 \tanh \lambda y_c + k_4 \coth \lambda y_m - \frac{1}{\mu_s} c_n \coth \lambda y_m - \frac{1}{\mu_p} c_n \operatorname{csch} \lambda y_m + \frac{1}{\mu_s} c_n \operatorname{csch} \lambda y_m \quad (\text{A4.61})$$

$$k_4 \left(\left(\frac{\mu_p}{\mu_s} - 1 \right) \tanh \lambda y_c + \coth \lambda y_m - \frac{\mu_p}{\mu_s} \tanh \lambda y_m \right) = \quad (\text{A4.52})$$

$$- \frac{1}{\mu_s} c_n \tanh \lambda y_m + \frac{1}{\mu_s} c_n \coth \lambda y_m + \left(\frac{1}{\mu_p} - \frac{1}{\mu_s} \right) c_n \operatorname{csch} \lambda y_m$$

$$k_4 = c_n \frac{\left(\frac{1}{\mu_P} - \frac{1}{\mu_S} \right) \text{csch } \lambda y_m - \frac{1}{\mu_S} \tanh \lambda y_m + \frac{1}{\mu_S} \coth \lambda y_m}{\left(\frac{\mu_P}{\mu_S} - 1 \right) \tanh \lambda y_c + \coth \lambda y_m - \frac{\mu_P}{\mu_S} \tanh \lambda y_m} \quad (\text{A4.63})$$

The solution to the Navier-Stokes equation for this problem is

$$u_{sn}(y) = \left[k_1 \sinh \lambda y + \frac{1}{\mu_S} c_n \cosh \lambda y - \frac{1}{\mu_S} c_n \right] \quad (\text{A4.64})$$

$$u_{pn}(y) = \left[-k_4 \frac{\sinh \lambda y_c}{\cosh \lambda y_c} \sinh \lambda y + k_4 \cosh \lambda y - \frac{1}{\mu_P} c_n \right] \quad (\text{A4.65})$$

$$k_4 = c_n \frac{\left(\frac{1}{\mu_P} - \frac{1}{\mu_S} \right) \text{csch } \lambda y_m - \frac{1}{\mu_S} \tanh \lambda y_m + \frac{1}{\mu_S} \coth \lambda y_m}{\left(\frac{\mu_P}{\mu_S} - 1 \right) \tanh \lambda y_c + \coth \lambda y_m - \frac{\mu_P}{\mu_S} \tanh \lambda y_m} \quad (\text{A4.63})$$

$$k_1 = -\frac{\mu_P}{\mu_S} k_4 \tanh \lambda y_c + \frac{\mu_P}{\mu_S} k_4 \tanh \lambda y_m - \frac{1}{\mu_S} c_n \tanh \lambda y_m \quad (\text{A4.60})$$

$$\lambda = \frac{\pi}{z_c} \left(n + \frac{1}{2} \right) \quad (\text{A4.38}) \quad c_n = \frac{\partial p}{\partial x} \frac{z_c^{2.5} \sqrt{2}}{\left(n + \frac{1}{2} \right)^3 \pi^3} \quad (\text{A4.46})$$

A4.4 Analytic Model Implemented in MATLAB

When the analytic model is coded into MATLAB, a number ε must be added to the denominator of k_4 to keep the computer from trying to divide by zero.

$$k_4 = c_n \frac{\left(\frac{1}{\mu_P} - \frac{1}{\mu_S} \right) \text{csch } \lambda y_m - \frac{1}{\mu_S} \tanh \lambda y_m + \frac{1}{\mu_S} \coth \lambda y_m}{\varepsilon + \left(\frac{\mu_P}{\mu_S} - 1 \right) \tanh \lambda y_c + \coth \lambda y_m - \frac{\mu_P}{\mu_S} \tanh \lambda y_m} \quad (\text{A4.66})$$

The smallest ε was determined to be $\varepsilon = 1 \times 10^{-15}$

The MATLAB model was tested to determine the optimal mesh size and n in the series expansion. The mesh size affects the integration of the flow rate values; the side flow rate (Q_S), the center flow rate (Q_C), and the ratio $Q_S:Q_C$ are examined. At a mesh size of $0.125 \mu\text{m}$, the maximum % error from twice the mesh size ($0.25 \mu\text{m}$) converges to $< 0.5 \%$. The % error for the flow rate values converges very quickly as n increases. Values above $n = 4$ give sufficient accuracy.

Table A4.2. Calculated error for the MATLAB model with varying mesh size
n=10 dp/dx = 1e6 [Pa/m]

mesh size	Qs [$\mu\text{l/min}$]	% error	Qc [$\mu\text{l/min}$]	% error	Qs:Qc	% error
2 μm	4.21E-01	-	2.12E-01	-	1.9886	-
1 μm	4.21E-01	0.123	2.03E-01	4.385	2.0732	4.083
0.5 μm	4.20E-01	0.327	1.98E-01	2.360	2.1152	1.986
0.25 μm	4.19E-01	0.228	1.96E-01	1.219	2.1361	0.980
0.125 μm	4.18E-01	0.130	1.95E-01	0.619	2.1466	0.486
0.0625 μm	4.18E-01	0.069	1.94E-01	0.312	2.1518	0.242

Table A4.3. Calculated error for the MATLAB model with varying n in the series expansion
mesh size = 0.125 μm

n	Qs [$\mu\text{l/min}$]	% error	Qc [$\mu\text{l/min}$]	% error	Qs:Qc	% error
2	4.17E-01	-	1.95E-01	-	2.1448	-
4	4.18E-01	0.1067	1.95E-01	0.0400	2.1462	0.0667
6	4.18E-01	0.0196	1.95E-01	0.0072	2.1465	0.0124
8	4.18E-01	0.0061	1.95E-01	0.0022	2.1465	0.0038
10	4.18E-01	0.0025	1.95E-01	0.0009	2.1466	0.0016
12	4.18E-01	0.0012	1.95E-01	0.0005	2.1466	0.0007
14	4.18E-01	0.0006	1.95E-01	0.0002	2.1466	0.0004
16	4.18E-01	0.0004	1.95E-01	0.0002	2.1466	0.0002

A4.4.1 MATLAB Code

```
% usolve.m
% began: August 15, 2001
% last modification: September 11, 2001
% 3D analysis of my flow channel, taking into account the 2 different
% viscosities of the two fluids
% flow is in the x-direction (u_x)
% y is the wide dimension, y=0 is the edge, y=yc is the center
% z is the depth, z=0 is the edge, z=zc is the center
% derivation of equations see ExpNotes.01.08.xx.doc and prior documents
clear;

% set some variables stuff to zero
ThetaS = 0;
ThetaP = 0;

% define constants
mu_s = 0.00711; % viscosity of saline
mu_p = 0.0060; % viscosity of peptide
yc = 36e-6; % m
zc = 12e-6; % m
z_step = 1e-6
y_step = 1e-6
% define ym and dp/dx
ym = 24e-6; % m
dpdx = -1.0E+05; % Pa

yc_index = abs(1 + (yc/y_step))
zc_index = abs(1 + (zc/z_step))

Us = zeros(zc_index, yc_index);
Up=Us;
yvector=Us;
zvector=Us;

% saline
for z=0:z_step:zc
    for y=0:y_step:ym
        ThetaS = 0;
        for n=0:1:10
            lambda = (pi/zc)*(n + 1/2);
            cn = dpdx*(zc^2.5)*(2^0.5)/(((n + 1/2)*pi)^3); % calculate cn
            % calculate k4 and k1
            k4_numerator = cn*( ((1/mu_p) - (1/mu_s))*csch(lambda*ym) -
(1/mu_s)*tanh(lambda*ym)
+ (1/mu_s)*coth(lambda*ym) );
            % orig: addition of 1e-15 to prevent division by zero
            k4_denominator = 1e-15 + ((mu_p/mu_s)-1)*tanh(lambda*yc) + coth(lambda*ym)
- (mu_p/mu_s)*tanh(lambda*ym);
            k4 = k4_numerator/k4_denominator;
            k1 = -(mu_p/mu_s)*k4*tanh(lambda*yc) + (mu_p/mu_s)*k4*tanh(lambda*ym)
- (1/mu_s)*cn*tanh(lambda*ym);
            % Calculate ThetaSn
            ThetaSn = k1*sinh(lambda*y) + (1/mu_s)*cn*cosh(lambda*y) - (1/mu_s)*cn;
            % Calculate ThetaS
            ThetaS = ThetaSn*((2/zc)^0.5)*sin((n + 1/2)*pi*z/zc) + ThetaS;
        end
        Us(single(1 + (z/z_step)), single(1 + (y/y_step))) = ThetaS;
        % creating position matrices
        yvector(single(1 + (z/z_step)), single(1 + (y/y_step))) = y;
        zvector(single(1 + (z/z_step)), single(1 + (y/y_step))) = z;
    end
end

% peptide
for z=0:z_step:zc
    for y=ym:y_step:yc
        ThetaP = 0;
```

```

for n=0:1:10
    lambda = (pi/zc)*(n + 1/2);
    % calculate cn
    cn = dpdx*(zc^2.5)*(2^0.5)/(((n + 1/2)*pi)^3);
    % calculate k4
    k4_numerator = cn*((1/mu_p) - (1/mu_s))*csch(lambda*ym) -
        (1/mu_s)*tanh(lambda*ym) + (1/mu_s)*coth(lambda*ym);
    k4_denominator = 1e-15 + ((mu_p/mu_s)-1)*tanh(lambda*yc) + coth(lambda*ym)
        - (mu_p/mu_s)*tanh(lambda*ym);
    k4 = k4_numerator/k4_denominator;
    k1 = -(mu_p/mu_s)*k4*tanh(lambda*yc) + (mu_p/mu_s)*k4*tanh(lambda*ym)
        - (1/mu_s)*cn*tanh(lambda*ym);
    % Calculate ThetaPn
    ThetaPn = -k4*tanh(lambda*yc)*sinh(lambda*y) + k4*cosh(lambda*y) - (1/mu_p)*cn;
    % Calculate ThetaP
    ThetaP = ThetaPn*((2/zc)^0.5)*sin((n + 1/2)*pi*z/zc) + ThetaP;
end
    Up(single(1 + (z/z_step)), single(1 + (y/y_step))) = ThetaP;
    yvector(single(1 + (z/z_step)), single(1 + (y/y_step))) = y;
    zvector(single(1 + (z/z_step)), single(1 + (y/y_step))) = z;
end
end

sf = abs(1 + ym/y_step) %sf = shark fin = where Us and Up share a y coordinate

Us_truncated = Us(:,1:sf);
yvector_s_truncated = yvector(:,1:sf);
zvector_s_truncated = zvector(:,1:sf);

Up_truncated = Up(:,sf:yc_index);
yvector_p_truncated = yvector(:,sf:yc_index);
zvector_p_truncated = zvector(:,sf:yc_index);

U_combined = Us + Up;
% smoothes the overlap in the functions
U_combined(:,sf) = U_combined(:,sf)/2;

%plot full flow field, U_full
%
%          q1          q2
% (U_combined)
% -----
%          q4          q3
%
%
%
q2 = fliplr(U_combined);
q3 = flipud(q2);
q4 = flipud(U_combined);
% there are extra rows and columns: an extra yc in q2 and q3, and extra zc in q3 and q4
q2 = q2(:,2:yc_index); % removes column 1
q3 = q3(:,2:yc_index); % removes column 1
q3 = q3(2:zc_index,:); % removes row 1
q4 = q4(2:zc_index,:); % removes row 1

U_full=[U_combined q2; q4 q3];

%full_yvector =
yq2 = ones(zc_index, yc_index-1);
yq2 = yvector(1,yc_index)*yq2 + yvector(:,2:yc_index);
yq3 = ones(zc_index-1, yc_index-1);
yq3 = yvector(1,yc_index)*yq3 + yvector(2:zc_index,2:yc_index);
yq4 = yvector(2:zc_index,:);
full_yvector = [yvector yq2;yq4 yq3];

% full_zvector =
zq2 = zvector(1:zc_index,2:yc_index);
zq3 = ones(zc_index-1, yc_index-1);
zq3 = zvector(zc_index,1)*zq3 + zvector(2:zc_index,2:yc_index);
zq4 = ones(zc_index-1, yc_index);
zq4 = zvector(zc_index,1)*zq4 + zvector(2:zc_index,1:yc_index);
full_zvector = [zvector zq2;zq4 zq3];

```

```

% Integration
Qs = 0;
Qp = 0;
for z=1:1:(zc_index-1)
    for y=1:1:(yc_index-1)
        Qs=Qs + (y_step*z_step)*( (Us(z,y) + Us(z+1,y) + Us(z,y+1) + Us(z+1,y+1))/4 );
        Qp=Qp + (y_step*z_step)*2*( (Up(z,y) + Up(z+1,y) + Up(z,y+1) + Up(z+1,y+1))/4 );
    end
end

fprintf(1,'Qs = %d ul/min\n', Qs*6e10)
fprintf(1,'Qp = %d ul/min\n', Qp*6e10)
Qs/Qp

figure(1)
surf(yvector_s_truncated, zvector_s_truncated, Us_truncated)
shading flat
axis([0 yc 0 yc 0 1])
axis 'auto z'

figure(2)
surf(yvector_p_truncated, zvector_p_truncated, Up_truncated)
shading flat
axis([0 yc 0 yc 0 1])
axis 'auto z'

figure(3)
surf(full_yvector, full_zvector, U_full)
shading flat

view([0 0]);
axis([0 2*yc 0 2*yc 0 1])
axis 'auto z'

figure(4)
surf(full_yvector, full_zvector, U_full)
shading flat
axis([0 2*yc 0 2*yc 0 1])
axis 'auto z'

```

A4.5 Diffusivity Calculation for the Peptide

There are several equations for calculating diffusivity in water based on molecular volume [8]. These relations were used to approximate the diffusivity of the peptide.

$$\text{Wilke and Chang (1955)} \quad D_{BW} = \frac{7.4 \times 10^{-8} (\phi_w M_w)^{1/2} T}{\eta_w V_B^{0.6}} \text{ cm}^2/\text{s} \quad (\text{A4.67})$$

and

$$\text{Hayduk and Laudie (1974)} \quad D_{BW} = \frac{13.26 \times 10^{-5}}{\eta_w^{1.14} V_B^{0.589}} \text{ cm}^2/\text{s} \quad (\text{A4.68})$$

where

M_w = molecular weight of water (g/mol)

T = temperature (K)

η = viscosity of water (cP)

V_B = molar volume of solute B at boiling temperature (cm^3/mol)

ϕ_w = solvent association factor for water = 2.6

The molecular volume of the peptide can be found by summing the volumes of the single atoms [29]. The total molecular volume for KFE8 is tabulated in Table A4.4.

Table A4.4. Tabulation of the total molecular volume of a KFE8 monomer

		C	N in primary amines	N in secondary amines	O -OH	H
amino acid sub-units	K	6	1	1	1	13
	F	9	1		1	9
	E	5	1		3	6
	Rink amide		1			2
	Acetylated	2			1	3
number of sub-units in each monomer	2*K	12	2	2	2	26
	4*F	36	4		4	36
	2*E	10	2		6	12
	Rink		1			2
	acetyl	2			1	3
total sub-units		60	9	2	13	79
volume per element		14.8	10.5	12	12	3.7
Total Vol. per element		888	94.5	24	156	292.3
Volume of a monomer		1454.8 m ³ /kmol				

$$\text{Volume of a monomer} = 1454.8 \times 10^{-3} \text{ m}^3/\text{kmol}$$

$$V_B = 1454.8 \text{ ml/mol}$$

The diffusivity of the filaments, not single monomers, is desired. Data on the structural properties of the peptide, inferred through AFM experiments and molecular modeling studies, can provide the means to estimate the number of monomers in a filament. The filaments are made of several helical ribbons, which are composed of the monomers. The total molecular volume can be estimated by counting the number of monomers in a filament, then multiplying this value times the volume of a single monomer (see Tables 4.5 and 4.6).

Table A4.5. Tabulation of the total molecular volume of a KFE8 intermediate [25]

average length	~100 nm
monomers/turn	60
length/turn	20 nm
total monomers	~300

Table A4.6. Tabulation of the total molecular volume of a KFE8 filament [25]

average length	~1 μm
Intermediates/filament	~10
volume of 1 filament	~3000×1454.8 m ³ /kmol

Using this value for molecular volume, diffusivity of the peptide in solution was calculated using equations A4.67 and A4.68.

D (Wilkes and Chang)	D (Hayduk and Laudie)	
1.5375×10^{-8}	1.6242×10^{-8}	cm^2/s

The average of these two values is

$$D_{KFE8} = 1.58 \times 10^{-8} \text{ cm}^2/\text{s}$$

A4.6 Non-Dimensionalizing the Numerical Model

Non-dimensionalizing the numerical model often helps eliminate computational problems associated with very small and very large numbers. For the mass-transfer and fluid flow problems, the governing equations are the Convection-Diffusion equation and the Navier-Stokes equation.

The Convection-Diffusion equation for concentration is

$$\frac{\partial C}{\partial t} + V \cdot \nabla C = D \nabla^2 C . \quad (\text{A4.69})$$

$$\text{At steady-state, } \frac{\partial C}{\partial t} = 0. \quad (\text{A4.70})$$

$$C^* = \frac{C}{C_0} \quad (\text{A4.71})$$

is the normalized concentration where, C_0 = concentration of the species at the inlet.

$$V^* = \frac{V}{V_0} \quad (\text{A4.72})$$

is the normalized velocity where V_0 = average fluid velocity in the center region of the device.

$$\nabla = \frac{\nabla^*}{L} \quad \text{is the normalized gradient operator.} \quad (\text{A4.73})$$

$$\frac{\partial}{\partial x} = \frac{\nabla^*}{L} \quad \text{is the normalized partial derivative operator with respect to length. (A4.74)}$$

These substitutions give

$$V^* \nabla^* C^* = \frac{D}{LV_0} \nabla^{*2} C^*, \quad \text{the normalized Convection-Diffusion equation. (A4.75)}$$

$$\frac{D}{LV_0} = \frac{1}{Pe} \quad (A4.76)$$

For the Navier-Stokes equation

$$\rho \left[\frac{\partial v_x}{\partial t} + V \cdot \nabla V \right] = -\frac{\partial P}{\partial x} + \mu [\nabla^2 V] \quad (A4.77)$$

$$\text{At steady-state, } \frac{\partial v_x}{\partial t} = 0. \quad (A4.78)$$

$$\rho^* = \frac{\rho}{\rho_0} \quad \text{is the normalized fluid density. (A4.79)}$$

The above substitutions give

$$\rho^* V^* \cdot \nabla^* V^* = -\frac{\partial^* P}{\rho_0 V_0^2} + \frac{\mu}{\rho_0 V_0 L} \nabla^{*2} V^*, \quad \text{the normalized Navier-Stokes equation (A4.80)}$$

$$\frac{\mu}{\rho_0 V_0 L} = \frac{1}{Re} \quad (A4.81)$$

To normalized the numerical models,

$$\text{model geometry} = \frac{\text{device geometry}}{L} \quad (A4.82)$$

$$\text{model velocity} = \frac{\text{velocity}}{V_0} \quad (A4.83)$$

$$\text{model density} = \frac{\rho}{\rho_0} = 1 \quad (A4.84)$$

$$\text{model diffusivity} = \frac{1}{Pe} = \frac{D}{LV_0} \quad (\text{A4.85})$$

$$\text{model viscosity} = \frac{1}{Re} = \frac{\mu}{\rho_0 V_0 L} \quad (\text{A4.86})$$

For channels 24-24-24 μm by 24 μm deep, L = hydraulic diameter = $\frac{4 \cdot (\text{cross - sectional area})}{\text{wetted perimeter}} =$

0.0036 cm. From the initial Reynolds number calculation, $V_0 = 2.948 \times 10^{-3}$ m/s; this value is rounded to $V_0 = 3.0 \times 10^{-3}$ m/s. ρ for both the saline and the peptide is ~ 0.001 kg/cm³, so $\rho_0 = 0.001$ kg/cm³.

$$\text{The model diffusivity for saline} = \frac{D_{\text{saline}}}{LV_0} \quad (\text{A4.87})$$

$$= \frac{1.483 \times 10^{-5} \text{ cm}^2/\text{s}}{(3.6 \times 10^{-3} \text{ cm})(3.0 \times 10^{-1} \text{ cm/s})} = 0.013731481 \text{ (Pe} = 73\text{)}$$

$$\text{The model diffusivity for the peptide} = \frac{D_{\text{peptide}}}{LV_0} \quad (\text{A4.88})$$

$$= \frac{1.8 \times 10^{-8} \text{ cm}^2/\text{s}}{(3.6 \times 10^{-3} \text{ cm})(3.0 \times 10^{-1} \text{ cm/s})} = 1.6667 \times 10^{-5} \text{ (Pe} = 60,000\text{)}$$

$$\text{The model viscosity for saline} = \frac{\mu_{\text{saline}}}{\rho_0 V_0 L} \quad (\text{A4.89})$$

$$= \frac{7.11 \times 10^{-5} \text{ kg/cm.s}}{(0.001 \text{ kg/cm}^3)(3.0 \times 10^{-1} \text{ cm/s})(3.6 \times 10^{-3} \text{ cm})} = 65.8333 \text{ (Re} = 0.0151899\text{)}$$

$$\text{The model viscosity for peptide} = \frac{\mu_{\text{peptide}}}{\rho_0 V_0 L} \quad (\text{A4.90})$$

$$= \frac{6.01 \times 10^{-5} \text{ kg/cm.s}}{(0.001 \text{ kg/cm}^3)(3.0 \times 10^{-1} \text{ cm/s})(3.6 \times 10^{-3} \text{ cm})} = 55.6481 \text{ (Re} = 0.01797\text{)}$$

For the saline,

$$C_0 = C_{\text{in, saline}} = 0.1$$

For the peptide solution,

$$C_0 = C_{\text{in, peptide}} = 0.01$$

For the inlet concentrations of each of these species,

$$C^* = \frac{C_{\text{in}}}{C_0} = 1$$

The normalized parameters for the numerical models in this study are shown in table A4.7.

Table A4.7. Parameters for the normalized numerical models

channels 24-24-24									
	[V]	x	y		Q [μl/min]	Vo [cm/s]	0.3		
peptide	3.9097E-01	3.9097E-01	0.0000E+00	cm/s	1.3512E-01	L [cm]	0.0036		
saline	2.5452E-01	2.3917E-01	8.7050E-02	cm/s	8.7961E-02	D*saline	0.013731481	Pe	72.82535401
normalized									
peptide	1.3032E+00	1.3032E+00	0.0000E+00			μ*saline	65.83333333	Re	0.015189873
saline	8.4839E-01	7.9723E-01	2.9017E-01			D*peptide	1.46296E-05	Pe	68354.43038
						μ*peptide	55.55555556	Re	0.018
channels 24-6-24									
	[V]	x	y		Q [μl/min]	Vo [cm/s]	0.3		
peptide	4.3622E-01	4.3622E-01	0.0000E+00	cm/s	3.7690E-02	L [cm]	0.003323077		
saline	2.8297E-01	2.6591E-01	9.6782E-02	cm/s	9.7795E-02	D*saline	0.014875772	Pe	67.2234037
normalized									
peptide	1.4541E+00	1.4541E+00	0.0000E+00			μ*saline	60.28549383	Re	0.016587738
saline	9.4324E-01	8.8636E-01	3.2261E-01			D*peptide	1.58488E-05	Pe	63096.39727
						μ*peptide	60.18518519	Re	0.016615385
channels 24-12-24									
	[V]	x	y		Q [μl/min]	Vo [cm/s]	0.3		
peptide	3.9884E-01	3.9884E-01	0.0000E+00	cm/s	6.8920E-02	L [cm]	0.003428571		
saline	2.7529E-01	2.5869E-01	9.4154E-02	cm/s	9.5140E-02	D*saline	0.014418056	Pe	69.35748001
peptide	9.1335E-01	9.1335E-01	0.0000E+00	cm/s	1.5783E-01	μ*saline	58.43055556	Re	0.017114333 μ = 0.00601
saline	1.4666E-01	1.3782E-01	5.0162E-02	cm/s	5.0687E-02	μ*saline	1434.027778	Re	0.000697337 μ = 0.1475
normalized									
peptide	1.3295E+00	1.3295E+00	0.0000E+00			D*peptide	1.53611E-05	Pe	65099.4575
saline	9.1763E-01	8.6229E-01	3.1385E-01			μ*peptide	58.33333333	Re	0.017142857
peptide	3.0445E+00	3.0445E+00	0.0000E+00						
saline	4.8888E-01	4.5940E-01	1.6721E-01						

A5.1 Preparation of the Peptide Solution

1.0 weight percent KFE8 peptide solution was used in all of the experiments. Mechanical properties were available for a similar peptide sequence (EKF8) at this concentration (see Section 2.3.3). The peptide in powder form was measured into 1.5 ml Eppendorf centrifuge tubes (Eppendorf, Hamburg, Germany) in quantities of approximately 4 to 8 mg. Deionized filtered water was added to the tubes. The solution was mixed in a vortexer for 10 minutes, mixed in an ultrasonic cleaner for 20 minutes, then incubated at room temperature for approximately 2 hours.

A5.2 Micron-Scale Viscosity Experiment: Measurement Procedure and Validation

Measurements of the center fluorescent fluid stream were made from images taken by the CCD camera-microscope setup using Image Pro Plus video image acquisition and analysis software. The measurement tool was calibrated using the width of the channel, which was assumed to be the as-designed dimension of 72 microns. The dark regions surrounding the channels (Figure A5.2) result from the curved inner corners of the channel, formed in the etch process (Figure A5.1). The curved corners do not reflect light back towards the microscope objective, and therefore appear dark. The as-designed dimension was measured to the outside of the dark regions.

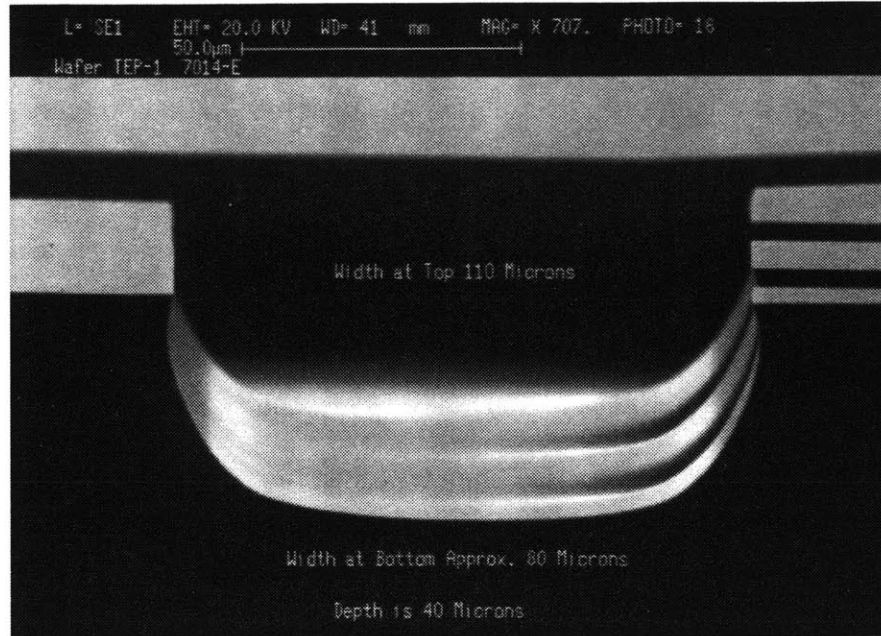


Figure A5.1. Scanning-electron microscope image of the cross-section of an etched silicon channel. The dimensions are different from those used in this study, but the curvature at the bottom of the channel will exist in our fabricated geometries. (Image courtesy of Joe Ricker, Charles Stark Draper Laboratory, Cambridge, MA)

Each fluorescent stream width measurement was made by taking two measurements (Figure A5.2). The width of the fluorescent stream was measured to the outer edges of the fluorescent stream. Despite convection dominance indicated by high Peclet numbers, the edge was less distinct at slower fluid velocities, making these measurements less reliable. The second measurement was the re-measuring of the channel outer dimension. This measurement was made parallel (by eye) to the first. The value for the width of the fluid stream used in the calculations, the adjusted stream width, was determined by the following operation:

$$\text{adjusted width} = 72 \cdot \frac{\text{measure stream width}}{\text{measure channel width}} \quad (\text{A5.1})$$

This adjustment effectively rendered the initial calibration unnecessary. If the device were to shift under the microscope or if the zoom knob was jarred, this constant re-calibration ensured consistent measurements.

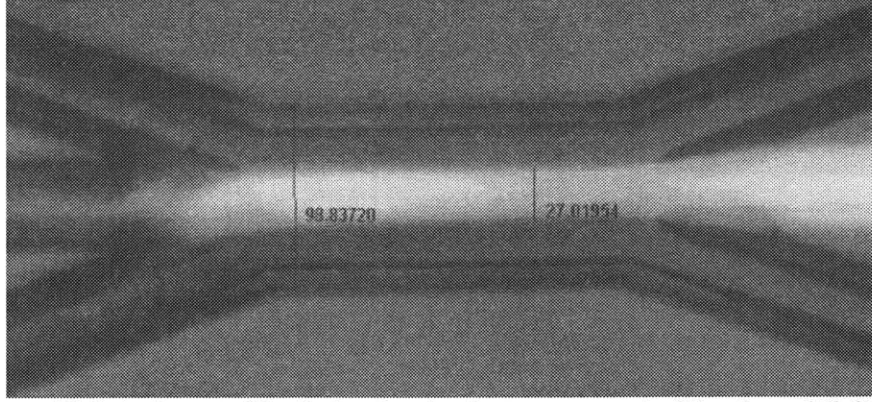


Figure A5.2. An image of the device showing the measurement of the channel (*left*) and the center stream (*right*). The fluid is flowing from right to left in this image.

A5.3 Calculation of μ_{center}

The values for center flow width, the viscosity of the side flows (water), and the flow rate ratio $Q_{\text{side}}:Q_{\text{center}}$ enabled calculation of the viscosity of the center flow (μ_{center}). To calculate this value, the center flow width was first converted to a value for y_m , the distance from the edge of the channel to the edge of the center flow stream. This value was rounded to the nearest mesh size of the analytic MATLAB model, 0.125 microns. The viscosity of the side flows (water) was assumed to be 1.00×10^{-3} Pa·s at room temperature. An initial value for μ_{center} was guessed and the MATLAB model was run. This value was revised and iterated until the experimental value for $Q_{\text{side}}:Q_{\text{center}}$ was obtained. The computed $Q_{\text{side}}:Q_{\text{center}}$ value was matched to the experimental value to within ± 0.0001 in five or fewer iterations of this procedure. Incidentally, when dealing with the analytic solution (which assumes laminar flow and no diffusion) only the ratio of $Q_{\text{side}}:Q_{\text{center}}$ needs to be considered because the magnitudes of Q_{side} and Q_{center} vary linearly with

$\frac{dp}{dx}$, but the ratio $Q_{\text{side}}:Q_{\text{center}}$ stays constant.

A potential source of error was that the cross-sectional geometry of the etched channel was not perfectly rectangular as it was assumed in the analytic solution, but was curved along the bottom edges (Figure A5.3).

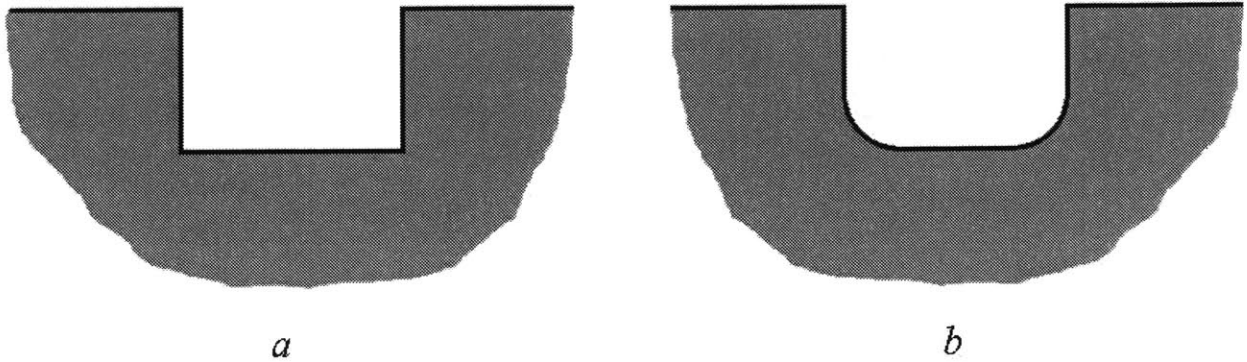


Figure A5.3. Drawings of (a) the assumed-geometry, used in the analytic solution, and (b) the actual geometry formed in the etch process

This curved geometry might significantly reduce the actual side-stream volume compared to the assumed volume. To approximate this effect, the measured channel dimension was reduced by a small percent, then μ_{center} was re-calculated. This procedure was repeated for several factors (0.9, 0.95, 0.97) and the calculated viscosity values were compared to those calculated with the as-measured channel dimension (factor of 1). The standard deviation of the calculated μ_{center} values were plotted against the adjustment factor, for both the full collected data series ($n = 6$) and the data series with the outlier removed ($n = 5$) (Figure A5.4).

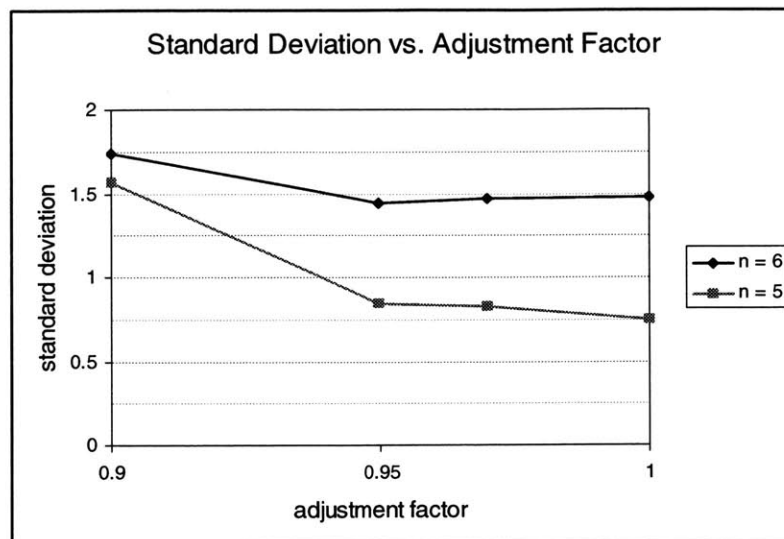


Figure A5.4. The standard deviation for data sets n=6 and n=5, for a range of adjustment factors

The data set for which the standard deviation value is the lowest is adjustment factor = 1, n = 5 (no adjustment to the measured channel width, and the outlier has been eliminated). The adjustment factor appears to worsen the result for μ_{center} . The experimental approach and execution were assumed to be sound, thus the adjustment factor 1 was chosen because it gave the most consistent results for μ_{center} .

A5.4 Design of the Simultaneous Pressure Release Fixtures

The fixtures for simultaneous pressure release were designed to be mounted on a 4-way stopcock set to the all-open position. When activated, they opened the fluid path to atmospheric pressure at the stopcock. Two different pressure release fixtures were designed and fabricated. The peptide pressure release fixture was constructed from a medium-sized binder clip, machined to fit snugly on the Luer-fitting of a stopcock and clamp a small piece of glass over the fluid port (Figure A5.5).

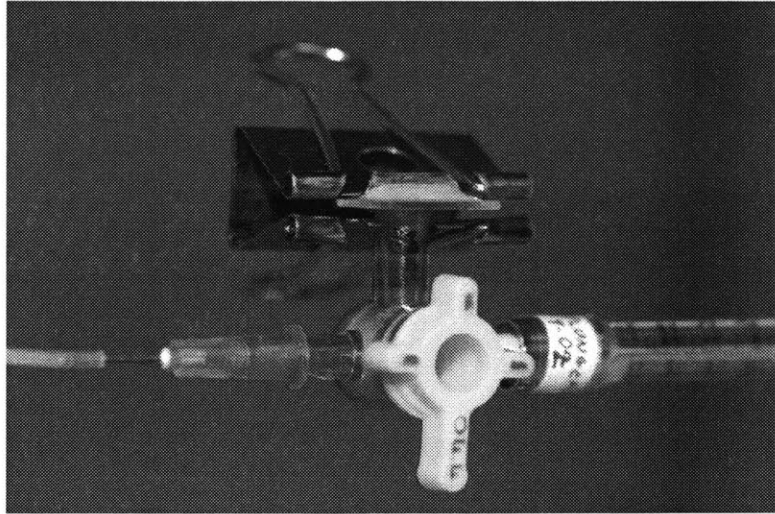


Figure A5.5. The single-syringe pressure release fixture

Opening the inlets to atmospheric pressure required pressure release fixtures on three fluid paths. For a single, two-handed operator to accomplish this feat, the saline pressure release fixture was designed to open both saline fluid paths to atmospheric pressure by pressing and locking a single lever (Figure A5.6).

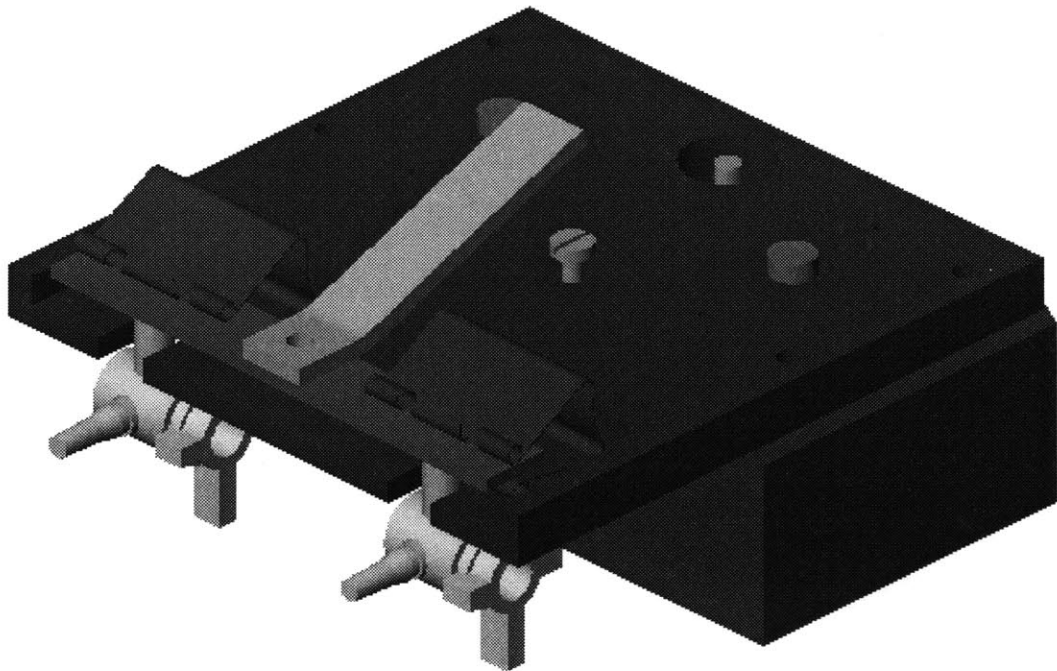


Figure A5.6. The saline pressure release fixture. The black base represents the syringe mounting block of the syringe pump.

Machined binder clips were used to clamp small pieces of glass to the stopcock openings. A small sheet of Parafilm[®] (American Can Company, Greenwich, CT) was placed between the stopcock and the glass to form an airtight seal (Figure A5.7, Figure A5.8).

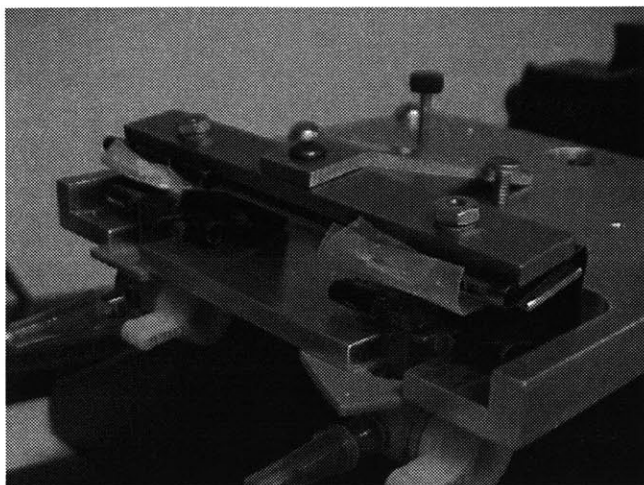


Figure A5.7. The saline pressure release fixture, shown in the open position

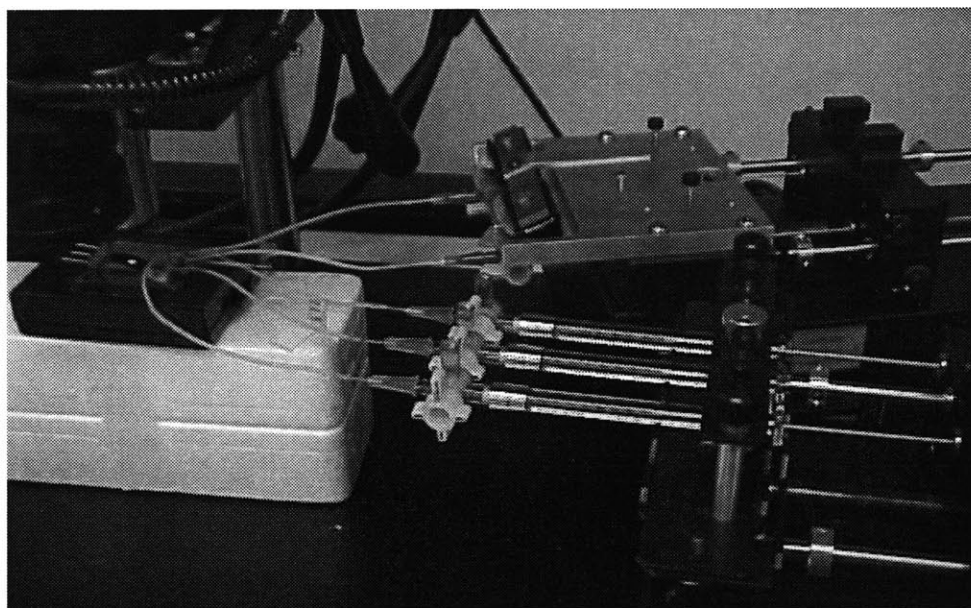


Figure A5.8. The saline pressure release fixture in the closed position (*right rear*)

182

$\phi .63$ THRU
 0
 2X .200
 4X .950
 2.20
 2.557
 3.450
 4.200
 4.40
 5X $\phi .089$ THRU
 No. 4-40 UNC-2B THRU
 4X $\phi .201$ THRU
 $\phi .107$ THRU
 No. 5-32 UNC-2B THRU
 2X R.25 MAX
 4X R.19 MAX
 1.31 $^{+.04}_{-.00}$
 2X .56 $^{+.02}_{-.00}$
 .38 $^{+.04}_{-.00}$
 .219 $\pm .010$
 SECTION A-A
 E. KIM
 x2359, x1986, ekim@mit.edu
 02.JAN.16
 2X CLAMP PLATE
 4.5x4x3/8 ALUMINUM PLATE
 .XX = $\pm .020$
 .XXX = $\pm .005$

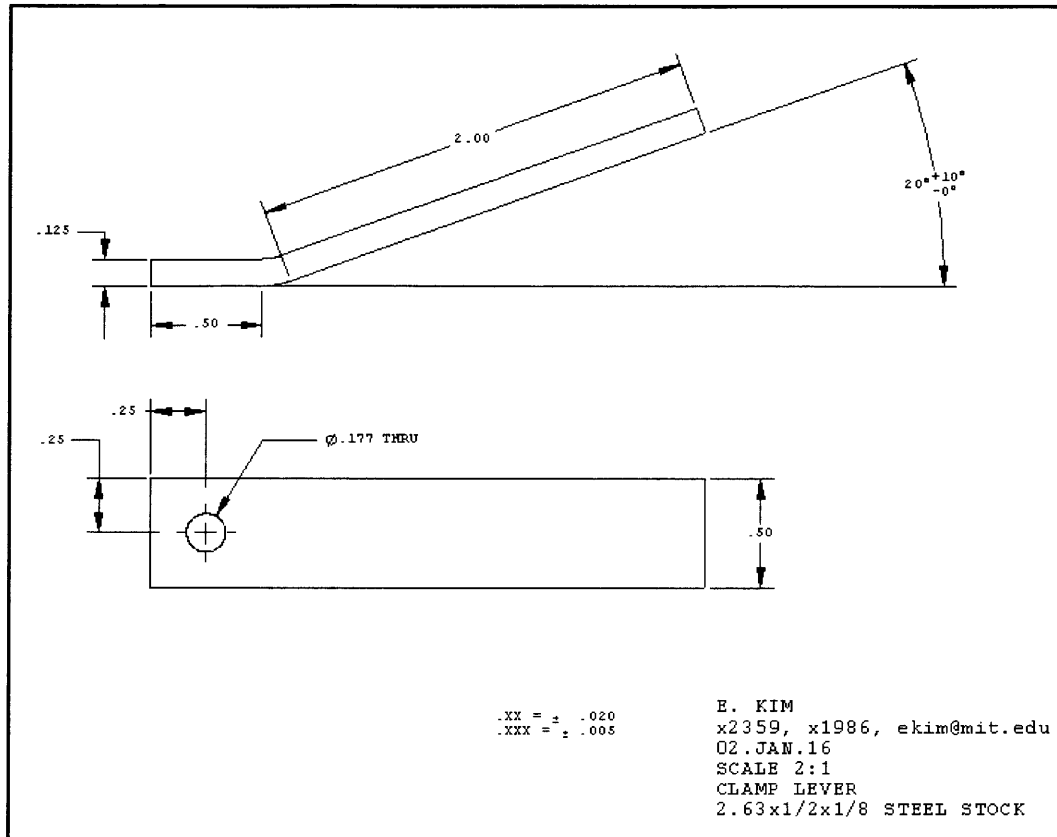


Figure 5.10. Clamp Lever

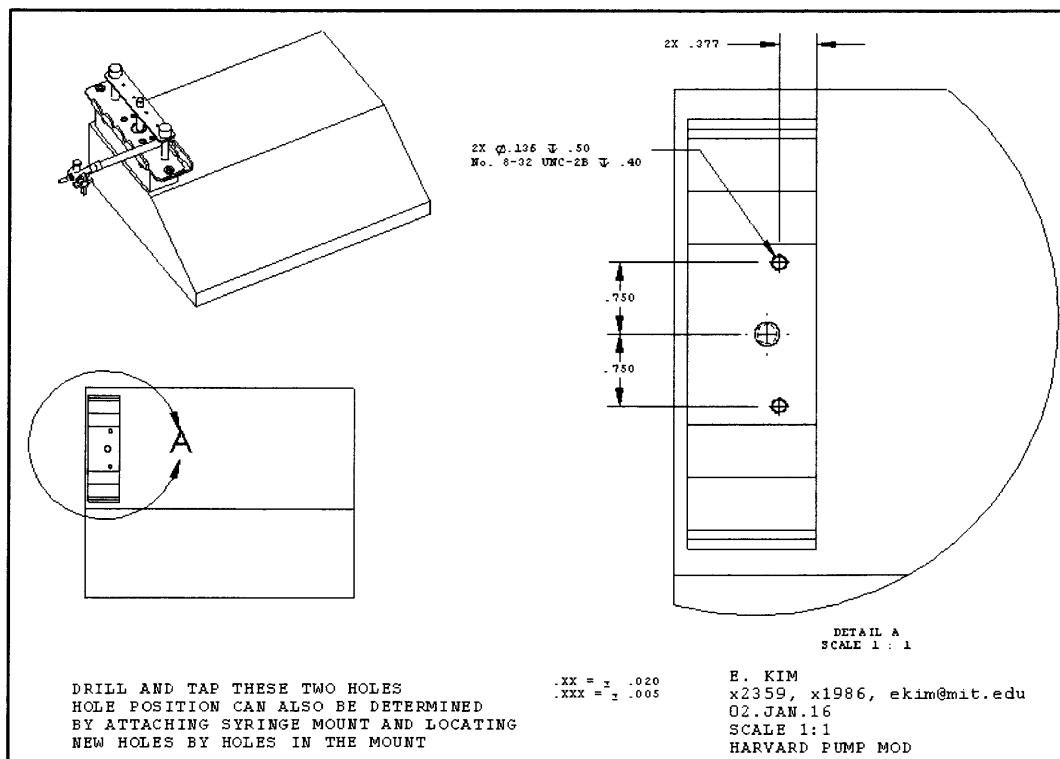


Figure 5.11. Harvard Pump Modification

This page intentionally left blank!